

Fall 12-15-2016

SCATTEROMETRY OF 50 NM HALF PITCH FEATURES

ruichao zhu
university of new mexico

Follow this and additional works at: https://digitalrepository.unm.edu/ose_etds

 Part of the [Electromagnetics and Photonics Commons](#), [Optics Commons](#), and the [Other Engineering Commons](#)

Recommended Citation

zhu, ruichao. "SCATTEROMETRY OF 50 NM HALF PITCH FEATURES." (2016). https://digitalrepository.unm.edu/ose_etds/55

This Dissertation is brought to you for free and open access by the Engineering ETDs at UNM Digital Repository. It has been accepted for inclusion in Optical Science and Engineering ETDs by an authorized administrator of UNM Digital Repository. For more information, please contact disc@unm.edu.

Ruichao Zhu

Candidate

Physics and Astronomy

Department

This dissertation is approved, and it is acceptable in quality and form for publication:

Approved by the Dissertation Committee:

Steven R. J. Brueck , Chairperson

Mansoor Sheik-Bahae

P. Randall Schunk

Francesca Cavallo

SCATTEROMETRY OF 50 NM HALF PITCH FEATURES

by

RUICHAO ZHU

B.S., Optical Science and Engineering, Fudan University
Shanghai, China, 2010

M.S., Optical Science and Engineering, University of New
Mexico
Albuquerque, USA, 2013

DISSERTATION

Submitted in Partial Fulfillment of the
Requirements for the Degree of

Doctor of Philosophy
Optical Science and Engineering

The University of New Mexico
Albuquerque, New Mexico

December, 2016

Acknowledgements

I would like to thank my advisor, Dr. Steven R.J. Brueck, for his support and guidance with his streaming knowledge and passion to me through all these years of my study. I cannot imagine I could finish my PhD work without his help and advice. He is a great mentor for my graduate study.

I would like to thank my committee members, Dr. Cavallo, Dr. Schunk and Dr. Sheik-Bahae, for their advices, guidance and supports.

I would like to thank S. Singhal and S.V. Sreenivasan at NASCENT center in University of Texas at Austin for preparing nanoimprint samples. Without their samples and advice, I cannot accomplish my work.

I would like to thank Dr. M. Babar Kaleem to provide the computer simulation code. All my simulation work and my custom code are based on his previous work.

I would like to thank Dr. Xiang He, Dr. Alex Neumann, Dr. Alex Raub and other students in my group, all other faculty, staff and student in Center for Hight Technology Materials (CHTM) for their help and friendship.

Finally, I would like to thank my wife, Fang Ding, my son, Haiyu, and other family members for your support these years.

Scatterometry of 50 nm Half Pitch Features

by

Ruichao Zhu

B.S., Optical Science and Engineering, Fudan University

Shanghai, China, 2010

M.S., Optical Science and Engineering, University of New Mexico

Albuquerque, NM, USA, 2013

Ph.D., Optical Science and Engineering, University of New Mexico

Albuquerque, NM, USA, 2016

Abstract

Metrology technologies are an essential adjunct to Integrated Circuit (I.C.) Semiconductor manufacturing. Scatterometry, an optical metrology, was chosen to measure 50 nm half pitch feature structures. A bread-board scatterometry system has been assembled to provide a non-contact, non-destructive, accurate and flexible measurement. A real-time, on-line scatterometry system has also been demonstrated and proven to provide a high throughput measurement.

Three different types of samples have been measured using the scatterometry setup. The wire-grid polarizer (WGP) sample has been made by Jet and Flash Nanoimprint Lithography with ~100 nm pitch and ~50 nm wide ~200 nm tall Al gratings on fused silica substrates. One of the resist grating samples has been made by Roll-to-Roll Nanoimprint Lithography with ~130 nm pitch and ~65 nm wide ~100 nm tall resist gratings on

polycarbonate substrate. The other resist grating samples have been made by Immersion Interference Lithography with ~80 nm pitch and ~70 nm tall resist gratings on silicon substrate.

For the WGP, four wavelengths (244 nm, 405 nm, 633 nm and 982 nm) were used to study the dependence of the parametric scatterometry on a function of the wavelength to sample pitch ratio (λ/p : from 2.4 to 9.8). Results show that even for a laser wavelength ten times larger than the sample pitch, scatterometry can still provide the characteristic structure information. The definition of the grating structure in the simulation has improved from a simple trapezoidal structure to a more complicated model with top rounding structure and an Al_2O_3 “skin”. With a better model and definition of the structure, simulation results have been closer to measurement results for all four wavelengths and the parameter sets present a very close results from scatterometry measurements. For the resist grating samples, scatterometry has less sensitivity because of lower index contrast than WGP, but a 405 nm laser source can still provide effective measurement on ~100 nm pitch resist samples. The scatterometry results are also sensitive to inhomogeneity of the resist sample and show a capability for classifying different types of macroscopic defects.

A model-based limitation study for both WGP and resist grating shows the fundamental limits of scatterometry for different materials and structures based on current noise levels. We have simulated a reducing linewidth and height of gratings with fixed pitch and the conditions with scaling the entire grating structure and have demonstrated that the potential capability of scatterometry can approach down to 10 nm feature size with a 405 nm laser.

Contents

List of Figures	ix
List of Tables	xiii
1. Introduction	1
1.1. Introduction to metrology	1
1.2 Metrology in Manufacturing	1
1.3 Metrology Technologies	5
1.3.1 Atomic Force Microscope	6
1.3.2 Scanning Electron Microscopy	8
1.3 Scatterometry	10
1.3.1 Wavelength-dependent scatterometry.....	12
1.3.2 Angular-dependent scatterometry	13
1.4 Methods to Utilize Scatterometry	14
1.5 Outline of the Dissertation	16
2 Sample Preparation.....	18
2.1 Wire Grid Polarizer (WGP)	18
2.1.1 Characterization of WGP	18
2.1.2 Fabrication process.....	20

2.2 Resist Grating	23
2.2.1 Resist grating made by J-FIL.....	23
2.2.2 Resist Grating made by Immersion Interference Lithography	24
3 Process of Scatterometry	32
3.1 Scatterometry Simulations	32
3.1.1 Introduction of RCWA.....	32
3.1.2 Definition of the Vertical Direction in RCWA.....	33
3.1.3 Definition of the horizontal direction in RCWA	37
3.1.4 RCWA Code for Additional Layer in the Horizontal Direction .	38
3.1.5 Selecting the Correct Number of Modes	40
3.2 Scatterometry Measurements.....	43
3.2.1 Measurement setup	43
3.2.2 Reliability of measurement setup	44
3.3 Fitting Process	48
3.3.1 Automatic fitting process.....	49
3.3.2 Library search	50
4. Experiments and Results	52
4.1 Wire Grid Polarizer	52
4.1.1 Measurements at Multiple Wavelengths	54
4.1.2 Effective Medium Comparison.....	56

4.1.3 Simple Grating Definition	60
4.1.4 Structure Definition Improvement.....	63
4.2 Resist Grating	79
4.2.1 Resist Grating Made by J-FIL	80
4.2.2 Resist Grating Made by IIL	86
4.3 In-line Scatterometry Attempts	90
5 Limits of Scatterometry.....	94
5.1 Noise Level	94
5.2 Limitation for WGP structure.....	95
5.2.1 Pitch at 100 nm.....	96
5.2.2 Pitch Variation from 100 nm to 5 nm.....	98
5.3 Resist Grating	100
5.3.1 Pitch at 130 nm	101
5.3.2 Pitch Variation from 130 nm to 10 nm.....	103
6. Conclusion and Future Work.....	106
6.1 Conclusion	106
6.2 Future Work	108
Reference.....	111

List of Figures

Figure 1.1 Etching conditions with different shape of mask.....	4
Figure 1.2 Deposition results	5
Figure 1.3 image of AFM working zone	8
Figure 1.4 image of SEM	9
Figure 1.5 image of wavelength dependent scatterometry	13
Figure 2.1 Fabrication process for an etched WGP.....	19
Figure 2.2 Jet and Flash Imprint Process.....	21
Figure 2.3 The imprinted film stack.	22
Figure 2.4 SEM image of WGP sample.....	22
Figure 2.5 Imprinting scheme selected for high-throughput flexible film imprinting	24
Figure 2.6 Interference Lithography setup	27
Figure 2.7 Immersion Interference Lithography setup	28
Figure 2.8 Snell's Law at prism interfaces	29
Figure 2.9 Function of bottom ARC.....	30
Figure 2.10 SEM of resist grating	31
Figure 3.1 1D grating structure	34
Figure 3.2 Fabry-Perot interference effect.....	35
Figure 3.3 Definition for a trapezoid grating structure	36
Figure 3.4 Definition of c_1 and c_2 for grating structure.....	37
Figure 3.5 Additional layer for grating structure.....	39
Figure 3.6 Number of modes in Fourier expansion	40
Figure 3.7 Simulation result for different modes with same structure at 45°	41
Figure 3.8 Simulation result for varying the number of modes in the RCWA simulation	42
Figure 3.9 Simulation result for different modes with same structure at angle range	

.....	43
Figure 3.10 Schematic top view of scatterometry experimental system.....	45
Figure 3.11 Test measurement on glass slide with TE polarization at 244 nm	46
Figure 3.12 Structure definition in CST	47
Figure 3.13 Comparison with Scatterometry measurement and simulation results.	48
Figure 4.1 the red line is grating direction and the blue line is polarization direction	53
Figure 4.2 Simulations at 244 nm	54
Figure 4.3 Measurement results at 244 nm.....	56
Figure 4.4 Measurement results at 405 nm.....	54
Figure 4.5 Measurement results at 632 nm.....	56
Figure 4.6 Measurement results at 982 nm.....	56
Figure 4.7 Measurement and effective medium approaches at 244 nm	58
Figure 4.8 Measurement and effective medium approaches at 405 nm	59
Figure 4.9 Measurement and effective medium approaches at 633 nm	59
Figure 4.10 Measurement and effective medium approaches at 982 nm	59
Figure 4.11 SEM image for WGP	61
Figure 4.12 Grating structure without top rounding	62
Figure 4.13 Definition of grating structure with top rounding structure.	63
Figure 4.14 Fitting results for 244 nm measurements.....	64
Figure 4.15 Fitting results for 405 nm measurements.....	64
Figure 4.16 Fitting results for 633 nm measurements.....	65
Figure 4.17 Comparison of the simulation results with and without the Al ₂ O ₃ layer.	69
Figure 4.18 Fitting results for 244 nm measurements.....	70
Figure 4.19 Fitting results for 405 nm measurements.....	70
Figure 4.20 Fitting results for 633 nm measurements.....	71

Figure 4.21 Fitting results for 982 nm measurements.....	71
Figure 4.22 Major parameters variation at 244 nm.....	74
Figure 4.23 Major parameters variation at 405 nm.....	75
Figure 4.24 Major parameters variation at 633 nm.....	76
Figure 4.25 Major parameters variation at 982 nm.....	77
Figure 4.26 Parallel conditions between gratings and polarizations	79
Figure 4.27 Definition of grating structure for J-FIL resist grating	80
Figure 4.28 Major parameters variation at 405 nm.....	81
Figure 4.29 Fitting results of resist grating for 405 nm measurements.....	83
Figure 4.30 Different types of defects and reflection pattern	85
Figure 4.31 Scatterometry measurement at different area with different type of defects.....	85
Figure 4.32 Definition of grating structure for IIL grating	86
Figure 4.33 Major parameters variation at 405 nm.....	87
Figure 4.34 Fitting results of resist grating for 405 nm measurements.....	89
Figure 4.35 SEM of resist grating	89
Figure 4.36 Real-time scatterometry design in Zemax	91
Figure 5.1 Varying Al thickness at fixed 100 nm pitch for WGP.....	96
Figure 5.2 Al thickness at 10 nm.....	96
Figure 5.3 Varying line width at fixed 100 nm pitch for WGP	97
Figure 5.4 Bottom width at 10 nm.....	96
Figure 5.5 Varying Pitch from 100 nm to 10 nm for WGP.....	96
Figure 5.6 Pitch at 20 nm for WGP.....	96
Figure 5.7 Reflection at normal incidence for different pitch at TM polarization ...	100
Figure 5.8 Varying line width at fixed 130 nm pitch for resist grating	101
Figure 5.9 Bottom width at 10 nm.....	101
Figure 5.10 Varying resist thickness at fixed 130 nm pitch for resist grating	102

List of Figures

Figure 5.11 Resist thickness at 30 nm.....	102
Figure 5.12 Varying resist thickness at fixed pitch for resist grating.....	103
Figure 5.13 Pitch at 24 nm for resist grating at TE polarization.....	104
Figure 5.14 Comparison with grating structure simulation at pitch=14 nm and effective medium	105

List of Tables

Table 4.1 Scatterometry fitting results with top rounding.....	66
Table 4.2 Fitting results of two different 405 nm laser	67
Table 4.3 Scatterometry fitting results of WGP with Al ₂ O ₃	72
Table 4.4 Comparison of parameter variances at different wavelengths for the WGP with and without the Al ₂ O ₃ layer.....	73
Table 4.5 RMS between -5% and +5% conditions.....	78
Table 4.6 RMS between -5% and +5% conditions.....	82
Table 4.7 Scatterometry fitting results of resist grating.....	84
Table 4.8 RMS between -5% and +5% conditions.....	88
Table 4.9 Scatterometry fitting results of resist grating.....	89

1. Introduction

1.1. Introduction to metrology

For the past several decades, metrology has been an essential aspect of the semiconductor industry¹ because of the need to monitor procedures and provide quality control. As the scale of semiconductor products today are as small as 12nm and less², metrology technology faces a significant challenge and has become an issue for the industry. Recently, more and more nanoscale critical steps have been added to the manufacturing process to obtain denser electronics requiring complicated 3D structures (e.g. FINFETs^{3,4}). For example, pattern doubling or tripling⁵ are used to decrease the node to a smaller size, but the number of steps increases by comparison to the single lithography process. Because more parts and steps need to be monitored, metrology has become a very expensive and time-consuming aspect of manufacturing, and accordingly, the industry faces a serious problem when pursuing smaller size products. Therefore, there is an urgent need to develop and improve current metrology technologies to meet the industry's needs and keep pace with the development of other manufacturing technologies.

1.2 Metrology in Manufacturing

All steps in manufacturing require metrology to monitor product conditions, but because

1. Introduction

of time and cost, the metrology process is typically introduced only before several important steps to avoid possible critical problems. In the remainder of this section, two manufacturing processes are introduced that normally require metrology to evaluate product quality.

Etching is a very common and useful process in the semiconductor industry. Dry etching uses a plasma of gas ions (e.g., O⁻, F⁻, Cl⁻, etc.) to bombard the material to be removed; the most common procedure used in dry etching is Reactive-ion etching (RIE). The process takes place under high vacuum conditions, and the sample is placed at the center of the vacuum chamber with the material's surface facing up. A plasma is produced in the top of the chamber and bombards the sample surface from above. Dry etching is used typically to transfer a pattern into the substrate, or form a special pattern structure; therefore, a mask is necessary to protect the surface so that the plasma removes only the desired areas of the material. The mask can be metal or photoresist with a slower etching rate than target material.

Etching process is complicated and the final results are determined by many different aspects. For instance, the etch rate and time need to be carefully controlled to avoid etching away the mask; the gas component needs to be optimized to have a large ratio of etching rates between target material and mask material; in some cases the gas flow needs

1. Introduction

to be controlled to have either isotropic or anisotropic etching; minimize the etching rate in the horizontal direction to avoid etching target material underneath mask and etc.

Among them, a desired shape of mask is the essential requirement to have a right etching process. Figure 1.1(a) shows a trapezoid mask with a large top width. The mask has covered the whole surface of target material, thus gas ions in etching tool cannot reach target material causing an undesired etching result. It is necessary to use metrology tools to assess the condition and shape of the mask before etching. A perfect mask (usually a perfect rectangle) can guide the gas ions to etch the proper area to form a straight isotropic structure during the etching process. The structure after etching process also needs to be monitored because a good mask is a requirement but not a sufficient condition for a good etching result. Figure 1.1(b) shows even with a straight right-angle mask, there is still possible to have an undercut problem if the etching rate is not optimized. A poor etching result could cause significant uncertainty for the next steps in manufacturing which may be lead to an unstable performance and property of products. To avoid a defective sample, metrology is required at every single step in the etching process.

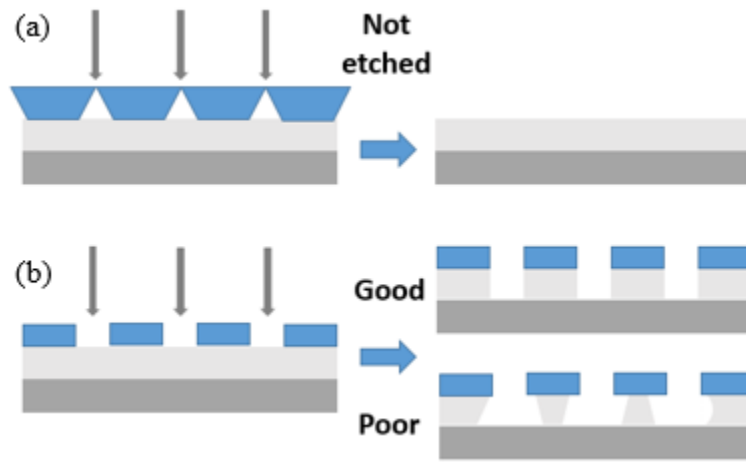


Figure 1.1 Etching conditions with different shape of mask (blue part is resist mask, white part is metal layer)

Deposition is another very common manufacturing process used in industry. There are many different tools available to deposit metal or other materials on a sample surface, including Chemical Vapor Deposition (CVD)⁶, Molecular Beam Epitaxy (MBE)⁷, and Atomic Layer Deposition (ALD)⁸. Deposition rate, deposition time and a straight rectangular mask are required for a reliable deposition process. Before deposition, the mask needs to be monitored to assure the mask with a flat surface on the top and a desired line and space ratio (see Figure 1.2(a)). Figure 1.2 (b) demonstrates that if the gaps in the mask are too narrow, depositing material cannot get into the gap between lines and can cover the whole surface. Metrology is also required after deposition process to check surface conditions. Figure 1.2(c) demonstrates that the depositing material could be too tall and contact with the top part after a deposition with a wrong speed and time.

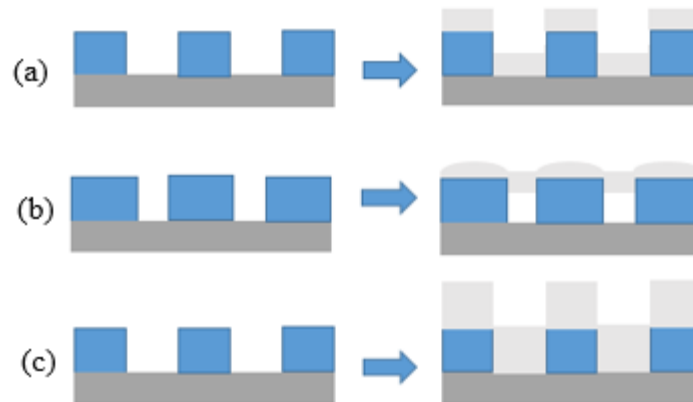


Figure 1.2 Deposition results (a) perfect condition (b) mask too fat (c) deposition time too long (blue part is resist mask, white part is metal layer)

Ideally, metrology is necessary and required at every step in the manufacturing process⁹, thus metrology is required to be: real-time, to facilitate high throughput; non-destructive, and preferably, non-contact, to prevent interference with processing; it also should have sufficient resolution to monitor drifts and changes in the manufacturing line, and should be flexible with respect to sampling and the number of areas on the samples. The next section introduces some commonly used metrology technologies.

1.3 Metrology Technologies

There are many different metrology technologies¹⁰. Three selected major optical metrology methods are introduced and explained below: Atomic Force Microscopy, Scanning Electron Microscopy, and Scatterometry.

1.3.1 Atomic Force Microscope

Atomic Force Microscope (AFM) is one of the most “popular” metrology tools¹¹⁻¹³. It uses a tiny probe that travels precisely across a μm -scale small area on the sample to measure the local properties. The tip is mounted on a cantilever. When the tip touches (contact mode) or approaches (non-contact mode) the sample surface through precise mechanical control of the cantilever, the force between the tip and the surface causes the cantilever to deflect away from the surface. A He-Ne laser is introduced at the center of the cantilever’s head to monitor this tilt. While the cantilever moves up and down, a position-sensitive photo diode is used to detect the accurate position of the laser’s reflection from the cantilever, which can detect the height information of the sample surface. The sample is fixed on a 3-dimensional mechanical stage. This allows the sample to be aligned close to the tip in the z-direction before measurement, and moves the sample in the x and y directions to allow the tip to scan the area of interest. The advantage of AFM is that it can provide an atomic scale resolution in the vertical direction for a low-aspect ratio sample, and forms a good image that can identify complex surface features. However, just as AFM has impressive abilities, it also has clear disadvantages. Because of the triangular shape of the tip, it is difficult to achieve good resolution in the horizontal direction, as the width of the tips causes a non-negligible error in the lateral measurement. Furthermore, with a high-aspect ratio sample, the tip cannot get into the gap between lines and cannot always touch bottom part of the sample

surface. Typically, there are several solutions to these problems. One is to calculate an effective tip width and conduct a careful calibration of the AFM results^{14,15}. However, this is a complicated and indirect process, and is not accurate when dealing with different surface and structure conditions. Another solution is to construct a narrow “rectangular” tip (like a GaN nanowire tip or carbon nanowire tip^{16,17}) rather than a triangular one, which produces better measurement results in the horizontal direction. Use of a carbon nanowire tip could sufficiently solve the measurement error of AFM at horizontal direction. However, carbon, not like a normal Si tip with Al coating, is a fragile material. It is very easy to be broken when measuring a hard material like Si or metal structure. A GaN tip may a better choice because of its rectangular shape and hardness of the material, but the large size of a GaN tip is still an issue and needs to be addressed in the future. An accurate AFM measurement needs to be taken in contact mode which means the tip needs to touch the sample surface during measurement. The tip may scratch the sample surface and cause an irreversible damage for the sample. There are some reports to make a soft polymer AFM tip¹⁸ to solve this problem, but the performance and resolution of the polymer tip are still very poor.

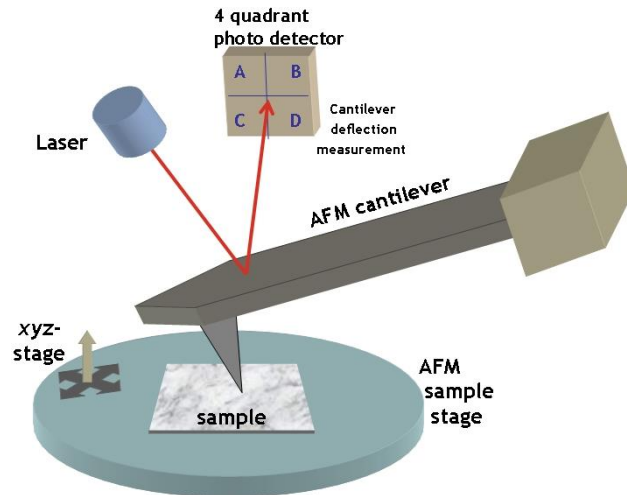


Figure 1.3 image of AFM working zone [Reference 19]

1.3.2 Scanning Electron Microscopy

Scanning Electron Microscopy (SEM) is another metrology tool used commonly in the semiconductor industry and laboratories^{20,21}. SEM can provide a direct image of the surface features from μm to nm scales. The SEM method obtains an image of the sample surface when an electron beam is incident to the sample, and a detector at the side collects the reflected or scattered electrons that represent information about the surface. The direct image of the surface is one of the most impressive advantages of SEM, as it can show an overall view over a range of areas, the blank layer under the structure (residual layer), and the cross-section conditions, which an AFM cannot measure. There are several different types of SEM, transmission SEM²², SEM with X-ray spectroscopy²³

1. Introduction

and etc. which can provide an accurate and comprehensive measurements. However, the cross-section and residual layer measurements require to cleave the sample which is not desired for industry manufacturing.

Today, only Critical-Dimension SEM (CD-SEM)²⁴ is used as a metrology technology in actual industrial processes. CD-SEM is a non-destructive technology which gives a top view of the sample surface and can get an ultra-high resolution image of the side wall roughness in current study²⁵. Although it can provide an accurate measurement of the pitch or line width of the grating, like AFM, it is unable to provide any information in the vertical direction in top view measurement, such as the thickness, or the bottom condition of structure. Another disadvantage of SEM measurement is that it is taken under high

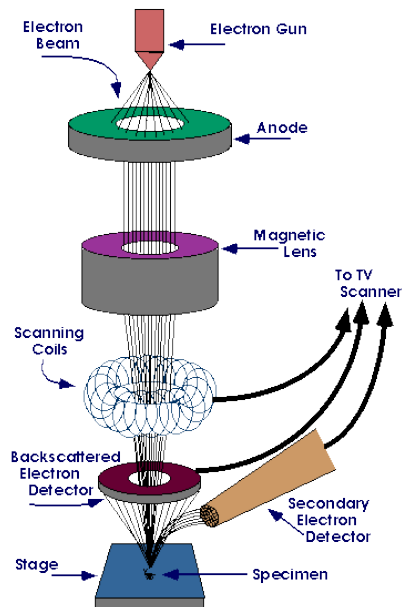


Figure 1.4 image of SEM [Reference 26]

vacuum conditions which is not desired for a manufacturing process.

1.3 Scatterometry

Scatterometry was first demonstrated by G A. Al-Jumaily, McNeil, et al in 1987 at the University of New Mexico²⁷, where a HeNe laser source was used to measure a 320 nm periodic structure. When this technology was first published, people doubted whether it could provide accurate information about the sample. However, after nearly 30 years of development, scatterometry has proven to be one of the most effective solutions for metrology at the 14 nm node in manufacturing today and possibly beyond²⁸⁻³⁵.

Scatterometry is an optical metrology based on diffraction from periodic structures, and it is well suited to the demands of nano-manufacturing of photonic and electronic components³⁶⁻³⁸. It satisfies the requirements for rapid, non-contact, on-line or at-line applications, and has demonstrated resolution commensurate with advanced semiconductor nodes³⁹. Scatterometry can measure a 1D periodic structure (e.g. gratings), a 2D Periodic structure (e.g. dots) and a 3D periodic structure (e.g. FinFETs and other structures that vary in all three dimensions). The scatterometry measurement process takes place in two steps: measurement (a forward process) and simulation (an inverse problem). Surface information and a fingerprint are measured first by scatterometry setup. The periodic structure is parameterized and thousands of computer-based simulations are calculated with different parameter sets within a certain range. The

solution for parameter sets of the surface structure appears when the simulation is closest to the measurement. The beam spot size typically ranges to as small as 10 μm and the size change does not impact diffractive efficiency. Thus, hundreds of thousands of periodic structures are measured at the same time (at 10 μm size, there are approximate 100 lines for 100 nm pitch grating structure). In the simulation, the periodic structure fulfills boundary condition and is assumed to be infinite in extent. It is reported that only twenty periods of resist grating samples in scatterometry are already sufficient to get a stable result and could be considered as an “infinity structure” in simulation³⁷. This indicates that a few periods can provide an accurate simulation result to demonstrate the average conditions of 1000 periods in measurement. The scatterometry results are not sensitive at local structure defects, but reflect an average conditions for a certain area of the sample. AFM and SEM can obtain a direct view of the sample surface, but only of a very small area, and the structure they measure may not represent the entire sample. This is one of the advantages of scatterometry, because all of the periodic structures within the area of the beam spot contribute to the reflection signal to represent the sample’s overall conditions. As mentioned above, AFM and CD-SEM can only provide an accurate measurement of the critical dimension (CD) from a top-down view so that current studies of in-line metrology focus on CD-AFM and CD-SEM, which cannot show other parameters of the grating structure, such as height and other features at the bottom of a structure. Another advantage of scatterometry is that its measurement system can be

adapted to a common ellipsometer tool and the diffraction measurement and inverse solving process are very similar between scatterometry and ellipsometry. We will introduce two different types of scatterometry⁴⁰ in the next section. One is wavelength-dependent scatterometry and the other is angular-dependent scatterometry.

1.3.1 Wavelength-dependent scatterometry

In wavelength-dependent scatterometry⁴¹, a wide range (usually from 230 nm to 800 nm) of wavelengths of white light is incident on the sample at a fixed angle (most often normal incidence). A rotatable polarizer is placed at the output of the white beam to switch the polarization of the beam between TM (electric field in the incidence plane) and TE (electric field perpendicular to the incidence plane). Under normal incidence conditions, a beam splitter placed above the sample reflected the beam into a detector. A reflection vs. wavelength graph (similar to an ellipsometer measurement) that contains information about the surface conditions is obtained after the measurement. Simulations with different parameter sets are calculated following the measurement to determine the

best-fitting parameters.

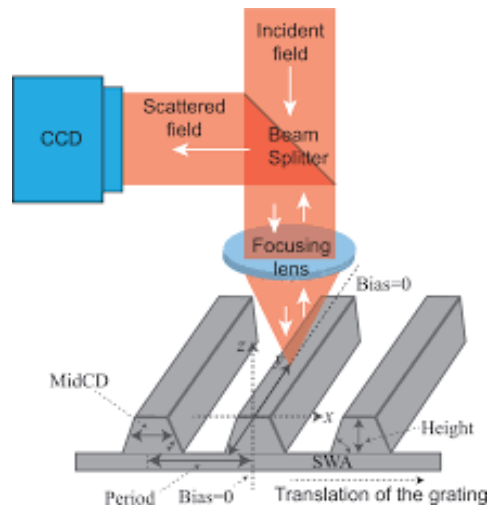


Figure 1.5 image of wavelength dependent scatterometry [Reference 42]

The advantage of wavelength-dependent scatterometry is that sample and optics do not need to be rotated or moved during measurement process which enhance the stability of the system. However, the simulation step requires a model of the dielectric properties of the various constituents of the film and nanostructure stack across the full range of wavelengths, often a difficult task for deposited films with varying compositions and stoichiometry. Furthermore, the brightness of white light is very low in the wavelength-dependent scatterometry system, thus the reflected signal is very small normally causing a low Signal / Noise ratio in measurement which results in a large uncertainty.

1.3.2 Angular-dependent scatterometry

Angular-dependent scatterometry only uses one wavelength beam source during a single

measurement process. A bread-board angular scatterometry setup is introduced in detail in Chapter 3. To obtain information about the grating parameters, the incident angle is varied over a certain range of angles to provide sufficient freedom and flexibility to solve the inverse problem of finding the parameter sets. The advantage of angular-dependent scatterometry is that the refractive index is fixed in the simulation because only one wavelength source is used, which makes the simulation more reliable. Another advantage is that, compared with wavelength-dependent scatterometry, angular-dependent scatterometry does not have high quality laser source. Even when using an inexpensive diode laser as source, the signals are typically larger than when using a spectrally filtered incoherent source and efficiently remove electronic noise from the measurement.

1.4 Methods to Utilize Scatterometry

As the current node and feature size of semiconductor products are reaching ~10 nm, the wavelength of the laser in metrology tools is always larger than the size of the structure that needs to be measured. In this project, a laser of several hundred nanometers wavelength was used to measure the 50 nm half-pitch features, in which the photons are at least two times larger than the sample pitch, and four times larger than the line width (CD) of the grating structure. With a single wavelength laser, as the scale of the sample becomes smaller and smaller, information about the structure in the reflection will be lost completely at some point and the only information the reflection provides is the effective

refractive index of the surface. The effective index can be obtained from the index of incidence medium (usually air), the index of the material of structures and the volume fraction of this material in the structure layer. This means that any structural information does not impact the scatterometry measurement and the structure is considered a plane homogenous layer with the effective refractive index. This is the ultimate limitation of scatterometry. To the author's knowledge, this limitation has not been studied well, and a better understanding of it could help achieve the full capability of scatterometry by determining approaches to its limitations.

At the current state, the smallest scale of the sample is limited by the fabrication technologies available to this project. On the other hand, there is no restriction on the size that can be simulated. Two different approaches of simulation-based limitation studies have been performed: one studies the smallest line width of the grating that can be measured at a fixed pitch. The other studies the smallest structure size that can be measured as the pitch becomes smaller and smaller at a 50% duty cycle. Although we cannot find a smaller sample to measure for these measurements, we can study the limitation with respect to wavelength / pitch (λ/p). While the pitch of the sample remained the same in the study, multiple wavelength lasers were used to measure the same sample structure to see whether the reflection still contains some information. After understanding the limits of wavelength / pitch, we can determine the smallest feature that

can be measured using a laser of a certain wavelength. In order to find a simulation result matching the measurement, an accurate structure model need to be defined in simulation.

The advantage of measuring at multiple wavelength lasers is that if the scatterometry results have significant variations at all of these wavelengths, it indicates that the structure model in simulation is not sufficient and some critical information and parameters are missing.

1.5 Outline of the Dissertation

The dissertation is presented in six chapters. Chapter 1 includes a general introduction to metrology technologies, and presents the details of three types of metrology technologies. Among these technologies, the advantages of scatterometry and the methods it uses to solve current barriers in the semiconductor industry are addressed.

Chapter 2 describes the characterization and fabrication of three different samples that are made by nanoimprint lithography and immersion interference lithography. The theories of these two lithographies are introduced, as well as the way in which an interference lithography is upgraded to an immersion interference lithography to obtain a smaller feature sample using a laser source of a fixed wavelength.

Chapter 3 presents the theory of scatterometry, which can be divided into two steps:

simulation and measurement. For simulation, the modeling code, Rigorous Coupled-Wave Analysis (RCWA), is introduced, and the methods to customize the code to fit the simulation requirements of the sample structure used in this dissertation are also discussed. In addition, the custom setup used to perform scatterometry is shown and its reliability is tested.

Chapter 4 presents the results of the scatterometry measurements and fitting for the three different types of samples used. The process to optimize the simulation code and structure definition, both of which can improve the fitting results, is described. An inline scatterometry effort combined with a library search is also discussed as a solution for real-time measurement.

Chapter 5 describes some of the limitations of scatterometry studies. A simulation study of scatterometry limitations with respect to the linewidth and grating thickness variation at a fixed feature size, and the smallest feature size measurable at a fixed wavelength for both a Wire Grid Polarizer and resist grating structure are presented.

Chapter 6 summarizes the project's research in scatterometry and proposes some future work.

2 Sample Preparation

The samples measured and analyzed were the Wire Grid Polarizer (WGP)³⁴ and resist grating. The samples were made by Nanoimprint Lithography (NIL)⁴³ and Immersion Interference Lithography (IIL). The WGP has an Al grating structure on a fused silica substrate and the resist grating consists of the resist material on a flexible polycarbonate substrate (NIL) and a silicon substrate (IIL). Using this measuring process for two completely different types of samples demonstrates the wide applicability of scatterometry for measurements of either a metallic or polymer materials and structures.

2.1 Wire Grid Polarizer (WGP)

2.1.1 Characterization of WGP

A Wire Grid Polarizer (WGP) is designed to allow one direction of the electric field to pass through it, thus the transmitted beam is linearly polarized. The WGP is widely used in various wavelength ranges, especially in the visible light range from 400 nm to 800 nm (e.g. for liquid crystal application). WGPs are also important optical components in lithography system, short wavelength laser, large displays, etc. because of its high polarization performance and temperature stability. Fused silica is used as the WGP substrate because the absorption coefficient of other glasses in the UV range is very high, such that they absorb nearly 90% of the energy of the UV light passing through it; thus,

2 Sample Preparation

normal glass optics do not work at the wavelength under 400 nm. In contrast, fused silica transmits nearly 90% energy at ~200 nm wavelength and is an ideal substrate material.

There are several different methods to fabricate a WGP. Our sample is an etched WGP. A blanket metal layer and oxide layer are deposited on the substrate first. Resist gratings on top of the structure functions as the etching mask for oxide layer and the etched oxide layer functions as the etching mask for metal layer. After removing the oxide hard mask layer, periodic metal gratings remains on the substrate. A detail introduction and discussion about the fabrication process is in the next section.

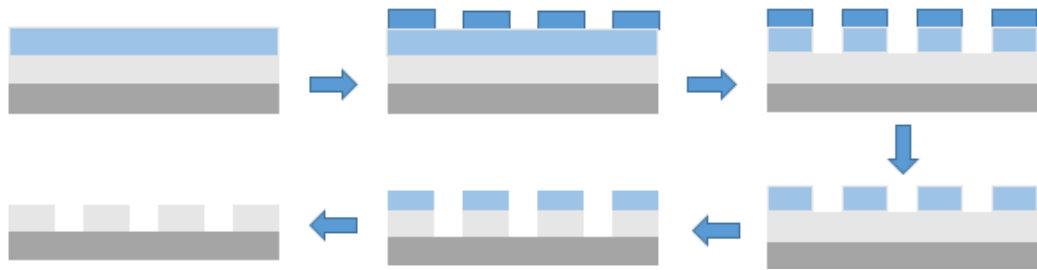


Figure 2.1 Fabrication process for an etched WGP, gray part is metal, light blue part is oxide hard mask and blue part is resist gratings.

The electric field of the laser can be divided into two orthogonal directions: parallel to the metal grating and perpendicular to the metal grating. For the electric field component parallel to the metal gratings, the electrons in the metal can move freely along the gratings in the surface plane to shout out the field which causes most energy in this direction to be reflected back by the WGP. For the electric field component perpendicular to the metal

gratings, the large gap between two gratings mean that the electrons cannot move in this direction. Most energy in this direction transmits through the metal grating structure. As a result, the beam passing through a WGP is linearly polarized with the polarization direction perpendicular to the metal grating.

2.1.2 Fabrication process

Nanoimprint lithography (NIL)⁴⁴⁻⁴⁷ is currently widely used in the semiconductor industry. NIL uses a hard mask with a metal structure on it as a stamp. During the lithography process, the hard mask is pushed to the sample surface with resist and a UV light is introduced on the top to cure the resist. The hard mask is removed from the sample surface after the process. NIL has a higher throughput than electron-beam and focused-ion-beam lithographies because its lithography process is done on a cm by cm large area simultaneously which is similar to interference lithography. NIL is less expensive than extreme ultraviolet lithography because it does not need an extremely large and complicated system. The resolution of NIL is not limited by optical diffraction and it has the ability to produce complex 2D and 3D structures because a high quality mask is used to form a pattern during lithography process. Besides these advantages, NIL also faces several challenges including mask wearing, resist dot alignment, surface tension when pushing mask on resist, adhesion when moving away the mask and etc. A lot of studies and efforts have been employed to find solutions to these challenges⁴⁸⁻⁵². As

a result, there are several different approaches to NIL. The technology used to produce our sample is the Jet and Flash Nanoimprint Lithography (J-FIL) and is discussed in this section.

The fabrication process of the WGP investigated here begins with a blanket electron-beam deposited an Al film at a target thickness of 200 nm on the fused silica substrate. Next a molecular Imprint Imprio-1100 tool (J-FIL) shown schematically below, was used to pattern the 100-nm pitch gratings. Finally, a Cl-based etch was used to transfer the nanoimprint pattern onto the Al layer.

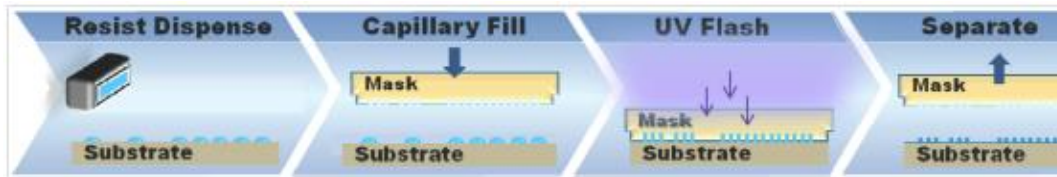


Figure 2.2 Jet and Flash Imprint Lithography Process. A low viscosity resist is deposited onto the substrate using an inkjet dispenser. Next, the patterned template is lowered onto the substrate so that the relief patterns are filled by capillary action. The resist is then crosslinked under UV radiation. Finally, the template is removed leaving a patterned resist on the substrate.

The film stack that was used to create the Al WGP is shown in Figure 2.3. The imprint processes produce a residual resist layer beneath the pattern. Thereafter, the etch processes began with a non-selective etch of the residual layer and adhesion films, which

2 Sample Preparation

have a total nominal thickness of 17 nm. Isotropic, oxygen-rich processes generally reduce, or “trim,” the critical dimension (CD) more than do low-oxygen processes. The addition of argon, combined with low pressure, leads to a process that, if timed correctly, causes very little CD loss. The de-scum process chosen was a low-pressure, low-power process with low oxygen flow and argon was used as a non-reactive, carrier gas. Once the de-scum process is completed, the oxide hard mask is etched using standard fluorine-based dry etch chemistry, and this hard mask is used to etch the Al film using chlorine-

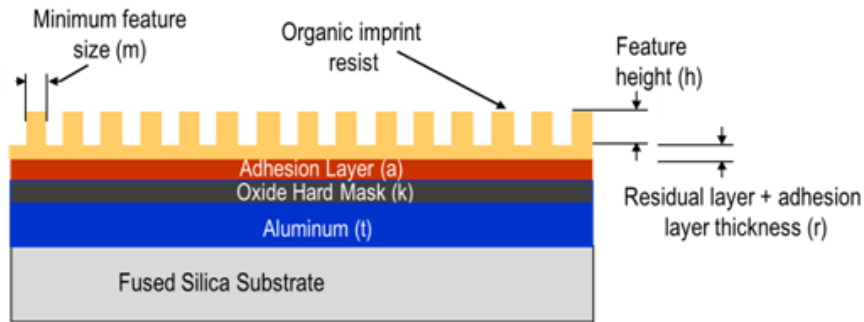


Figure 2.3 The imprinted film stack includes a grating resist pattern with nominal values of $m=50\text{nm}$, $h=125\text{nm}$, and $r=15\text{nm}$. The adhesion layer is an organic spin-on film with ‘a’ = 2nm. The oxide hard mask, $k = 25\text{nm}$, and Al thickness $t = 200\text{nm}$.

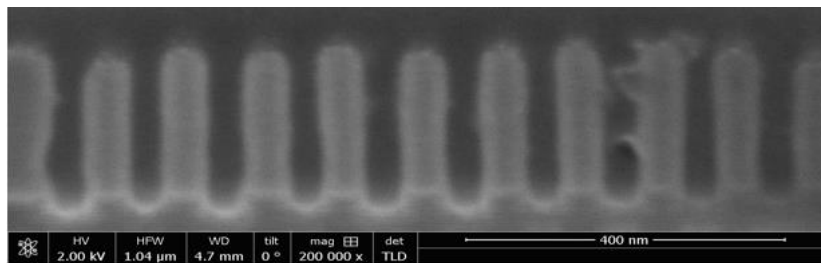


Figure 2.4 SEM image of WGP sample

based chemistry. Following the Al etch, the oxide mask is removed with an isotropic fluorine dry etch chemistry, which also leads to some undercut into exposed regions of the fused silica substrate.

2.2 Resist Grating

The second type of sample was a polymer resist grating. Resist grating usually is the first critical structure in the manufacturing process, which may be followed by etching, depositing metal, pattern transforming, and so on. It is very important to monitor and check the quality of the resist gratings and avoid possible defective samples that impact the final structure that thereby increasing cost and reducing yield⁵³⁻⁶². Two different lithography processes are used to produce resist grating: one is Roll-to-Roll Jet-and-Flash nanoimprint lithography (J-FIL) which is related to our project requirement and the other is immersion interference lithography (IIL). Both processes are widely used in semiconductor and integrated circuit (IC) industry. These two different lithographies and their fabrication procedures are discussed below.

2.2.1 Resist grating made by J-FIL

One of the resist samples was made using Roll-to-Roll J-FIL⁶³. As shown in Figure 2.5, this process uses a template, which is a fused silica wafer 150mm in diameter with a WGP pattern etched in it. First, the resist drops are dispensed on the flexible substrate so

that the drop distribution corresponds to the local pattern density of the template WGP. Then, the template is lowered into contact with the surface of the flexible substrate containing the drops, compressing the drops, which spread and merge into a continuous liquid film that fills in the features on the template. This is followed by broadband UV exposure to cure the imprint resist. Finally, the template is separated from the flexible substrate, which is then rolled forward to repeat the process on a new area of the substrate. The resist sample has ~130 nm pitch gratings ~100 nm in height. The flexible substrate material used is a commercially available polycarbonate.

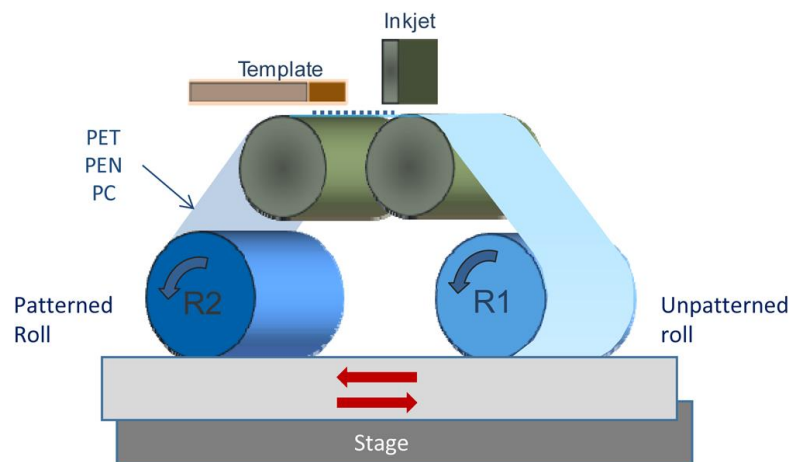


Figure 2.6 Imprinting scheme selected for high-throughput flexible film imprinting. [Reference 63]

2.2.2 Resist Grating made by Immersion Interference Lithography

2.2.2.1 Introduction to Immersion Interference Lithography

Interference Lithography (IL) is used widely to produce periodic gratings on the resist layer, and the pitch can be as small as $\lambda/2n$ (n is the refractive index of the medium above the photoresist layer). Neither a mask nor a lens system is needed in the IL process used to make small pitch grating structures; thus, IL is an inexpensive, large-area, time-saving method of lithography to fabricate nm-scale periodic features.

Because the grating pitch using IL is equal to $\lambda/2n$, there are two ways to improve the process to achieve a smaller feature size: normally using either a short wavelength to decrease λ , or conducting the exposure in a medium other than air to increase the n .

Recently, the most common laser used in industry which offers stable performance is 193 nm ArF pluses laser. Although there are shorter wavelength laser available, 193 nm laser is still the major light source used in industry because of the transmission limits of fused silica optics for the shorter wavelength laser. Therefore, trying to increase the index n is the only available solution. Immersion Interference Lithography (IIL) is a lithography technique in which the lithography process is completed in a high index fluid (water with $n=1.44$ at 193 nm was used in this dissertation) so that a smaller pitch compared to normal IL can be obtained during the lithography process with the same laser source.

In IL, two mutually coherent light beams are introduced to interfere with each other, and

the sample coated the photoresist is placed at the interference plane of the two beams.

The setup for IL is shown in Figure 2.6. The beam split is used to split the incident beam into two mutually coherent beams that can interfere with each other and a 3-Dimension vacuum stage can hold and move sample to the interference plane. Figure 2.6 (a) demonstrates a simplified IL setup which works with high transverse coherent source such as a single-mode light source. The laser source we used is a 193 nm ArF laser with multi-modes in output. The field at the right edge of a laser pulses is not coherent with the field at the left edge so that there is no coherence between the two beams at sample surfaces, shown in Figure 2.6(a). Figure 2.6 (b) demonstrates a solution that an additional Mirror A is placed in one of the light paths to flip a beam at one path so that the two beams are exactly the same and are coherent with themselves at the sample surface. At the interaction plane, the intensity of the interference has a standing wave with a cosine function that forms a grating structure in the resist layer on sample through the chemical reaction between the laser beam and resist. The best exposure contrast appears when the intensities of the two coherent beams are equal ($I_1=I_2=I_0$). The intensity function at the interaction plane can be simplified to

$$I(x) = 4I_0 \cos^2(k \sin(\theta)x) \quad (2.1)$$

where k is the photon wave vector $2\pi/\lambda$, θ is the incident angle and x is position on sample surface.

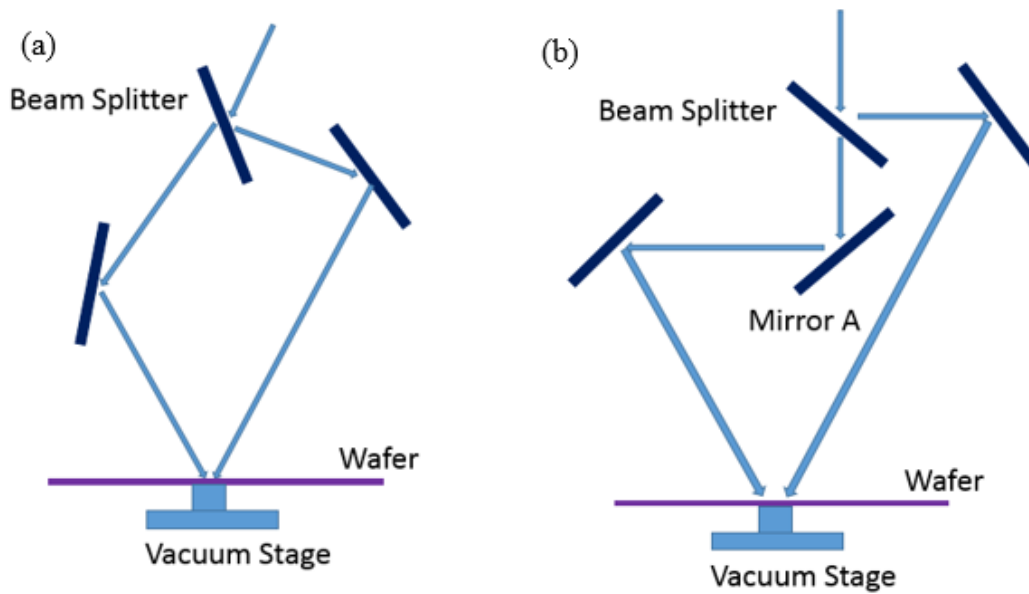


Figure 2.7 Interference Lithography setup (a) Beams not coherent without Mirror A (b) Beams coherent with Mirror A

The IIL setup is similar to that for IL, but there is a prism in front of the sample surface.

One of the functions of the prism in the system is that it can hold DI water with a uniform thickness because of the surface tension effect between prism and sample surface. At the interface between prism and DI water, the Snell's Law indicates that

$$NA = n_{prism} \sin\theta_1 = n_{water} \sin\theta_2 \quad (2.1)$$

2 Sample Preparation

where n_{prism} is refractive index of prism and is ~ 1.6 at 193 nm, n_{water} is refractive index of DI water and is ~ 1.44 at 193 nm and θ_1, θ_2 are the angle of incidence and transmission at the interface. The high index and the geometry of prism can provide a large NA to the lithography system which cannot be achieved at the interface between air and water. With a 60-degree prism system (see Figure 2.8), the largest NA at the interface between the prism and water appears when beam is introduced with normal incidence from air to prism ($\theta_{prism} = 90^\circ$ for an equilateral prism). The largest NA is equal to $n_{prism} \sin(\theta_{prism}) = 1.44$, yielding a smallest feature size of $p = \frac{\lambda}{2NA} = 67 \text{ nm}$ at $\lambda = 193 \text{ nm}$.

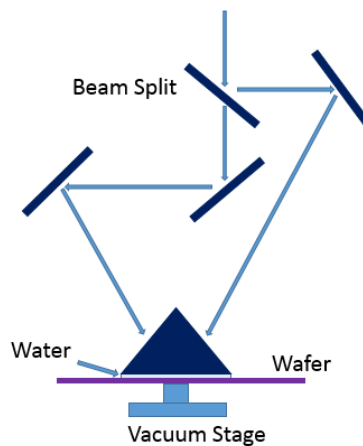


Figure 2.9 Immersion Interference Lithography setup

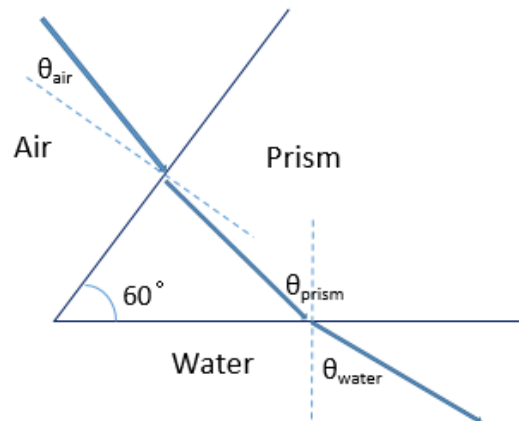


Figure 2.10 Snell's Law at prism interfaces

2.2.2.2 Fabrication process

A 6-inch silicon wafer was first cleaned with acetone and isopropyl alcohol (IPA) followed by a heating process at 205°C for one minute to remove any moisture on the wafer surface. A selected Anti-Reflection Coating (ARC) chemical material (ARC-145 from Brewer Science) was spin-coated directly on the Si substrate at 1500 RPM (rotations per minute) for 60s. The coating process is followed by a 60s hard bake at 205°C. The target thickness of the ARC layer is approximately 40 nm. An ARC layer is placed between the substrate and resist because, without the ARC, there is a very high reflection from the substrate (Si is a high reflectivity material) into photoresist which causes standing wave phenomena inside the resist pattern. This strong reflection, which disturbs the interference performance on the surface, is a major problem in IL. Figure 2.9 illustrates reflections from the photoresist-ARC interface and the ARC- substrate

interface. ARC refractive index and thickness are designed to make one-pass optical length of the beam in the ARC layer equal to $\lambda/4n$ ($n=1,2,3\dots$). Thus the total optical length beam traveling in the ARC is in terms of $\lambda/2$ which means that beam phase shifts by π in ARC layer. The two reflections from photoresist-ARC interface are canceled with each other because of this π phase shift. In our case, the ARC thickness is 40 nm and refractive index is ~ 1.2 . Thus the optical length is approximately 48 nm, which is exactly equal to $\lambda/4$ for 193 nm laser. ARC material is also designed with a high absorption coefficient which can absorb energy of beam to reduce the intensity of reflection from substrate. A desired ARC layer can limit the reflection into the photoresist less than 1%, which is an essential requirement for IL procedure.

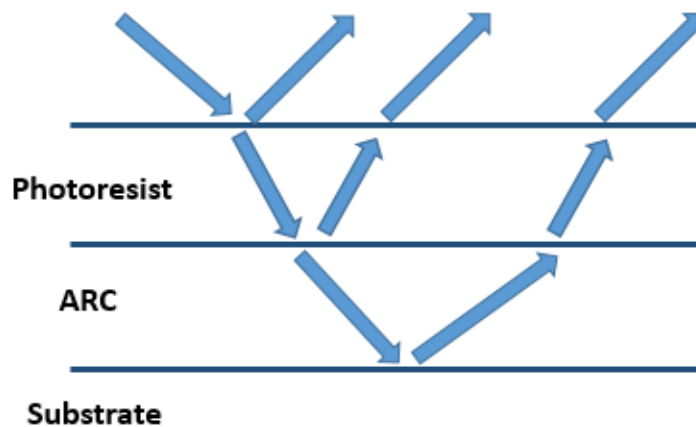


Figure 2.11 Function of bottom ARC

After the ARC is coated and baked at 205°C for 60 seconds, a resist layer is spin-coated on top of the ARC layer. A 60s, 2500 RPM coating process yields a 70 nm resist layer

2 Sample Preparation

(ARF AIM5518JN-7 from JSR Micro) adhering to the ARC layer. A 60 seconds hard baking at 120°C follows. Twenty pieces 1 inch by 1 inch samples can be obtained from the 6 inch wafer with proper cleaving. The next step is to place the 1 inch by 1 inch sample with the resist and ARC layer in the IIL setup as described above, and expose the sample to a certain dose using a 193 nm laser. After exposure, the sample must be heated to 115°C for 90 s to harden the structure, and then dipped in the developer for 60 s. There are many types of photoresist including positive resist and negative resist. We used positive resist, thus the resist area exposed with high laser intensity is dissolved in the developer and it is removed by a following DI water rinsing process. The resist area exposed with low laser intensity remained on the sample and formed a periodic grating pattern.

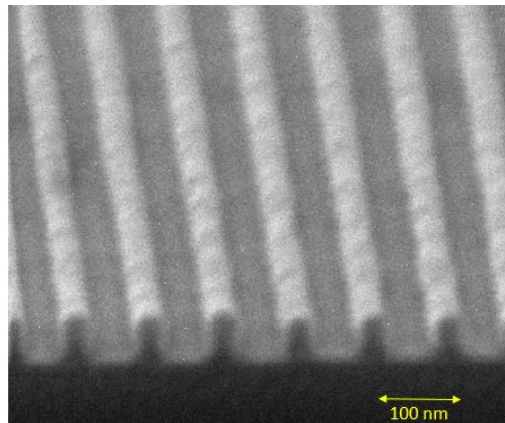


Figure 2.12 SEM of resist grating

3 Process of Scatterometry

Scatterometry is an optical metrology technology which is based on a two-step process: measurement (i.e. a forward problem) and simulation and fitting process (i.e. a reverse problem). The accuracy and efficiency of scatterometry depends on both steps and will be discussed in this chapter.

3.1 Scatterometry Simulations

3.1.1 Introduction of RCWA

The primary simulation method used here is Rigorous Coupled-Wave Analysis (RCWA), which was introduced first by Moharam and Gaylord in 1981⁶⁴. It provides a direct solution for Maxwell's equation for the reflection and diffraction of a grating structure. It has two fields with many different orders above and below a homogeneous layer or grating that can be described by a Floquet expansion. There is another field in the layer or grating to connect these two expansions. In 1D RCWA applications, grating structures or layers with different refractive indices are divided into several thin layers in the vertical direction so that the grating structure has vertical sidewalls and/or the plane layer has a single and constant refractive index. RCWA uses the Floquet expansion to model boundary conditions at the top and bottom of a layer. There is an eigenvalue system for each layer, and RCWA is used to solve these eigenvalue equations. These solutions then

can be used to calculate the amount of energy that is reflected, transmitted, and absorbed.

The RCWA coding used here in matlab is a custom program coded by Babar Minhas⁶⁵, a previous student in our group. The detailed theory and method used in this code is described and discussed in his thesis. A brief introduction and explanation of RCWA is provided below.

The first step in RCWA is to find the right unit cell of the structure, for example, for a 1D grating structure, the unit cell is the grating cross-section for one period cycle (one grating/one space). The boundary conditions are investigated and calculated in RCWA to simulate an infinite grating condition by defining only a finite structure. This limits the structures that can be simulated by RCWA to a periodic structure.

3.1.2 Definition of the Vertical Direction in RCWA

RCWA can simulate any 1D and 2D periodic structure. Because the structure measured and simulated is always a 1D grating structure in this dissertation, the methods used to define the geometry in RCWA introduced in this chapter focus on the 1D grating structure. To define the geometry of the structure in RCWA, the entire structure needs to be divided into several thin layers in which the width of the structure is constant in each layer. Thus, for a 1D grating structure, the thin layer either is a homogeneous layer

composed of a single material, or is a combination of grating and space (usually air in our case), while at the same time, the sidewall of the grating is vertical and the width of the grating is uniform in the z direction. For a simplified 1D grating structure, as shown in Figure 3.1, a grating structure lays on a series of plane layers and the substrate. The grating structure, plane layer, and substrate need to be defined separately in RCWA to perform the simulation.

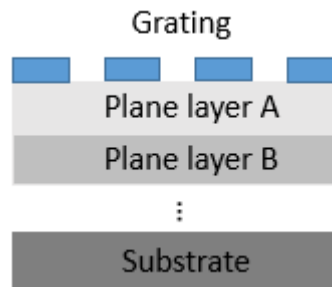


Figure 3.1 1D grating structure

The substrate is considered a homogenous layer, because its composition and refractive index are constant throughout. Generally, if considering reflection alone, we can assume that the substrate is infinitely thick and the transmitted energy into this layer either is reflected or absorbed in the substrate. If the substrate is not infinitely thick, and there is some reflection from the interface between the bottom of the substrate and the air, the well-known Fabry-Perot interference effect will occur when calculating the reflection. The Fabry-Perot effect is illustrated in the sketch shown in Figure 3.2. Briefly, two glass optics are placed with their reflective surfaces parallel to each other, and the beam travels

back and forth between the two. The reflection from surface A interfaces with the reflection from surface B, and forms an interference pattern at surface B. For a Fabry-Perot interferometer, surface A and surface B are coated with a highly reflective material to trap the energy between these two surfaces. If the substrate has a finite thickness, a Fabry-Perot effect will occur and RCWA will calculate the multiple reflections between the top and the bottom surface of the substrate. As a result, reflection vs. angle simulation will exhibit sharp changes and large noise at varying incident angle. These multiple reflections in the substrate are not desired in our experiment. To a substrate, the thickness

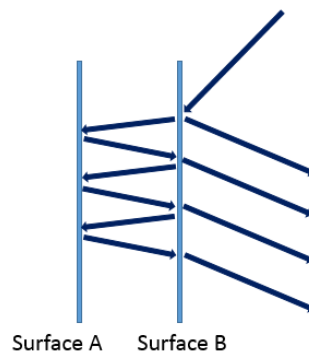


Figure 3.2 Fabry-Perot interference effect

of it can never be $\lambda/4$ thick. Further, this method only works for a fixed incident angle of beam. When incident angle need to change in a large range, like the simulation in our case, the optical length cannot fix at $\lambda/4$ for each angle. The solution for substrate reflection is to treat substrate as infinity thick.

In defining a multiple plane layer structure in RCWA, the structure is considered as

several homogenous layers that are similar to the substrate, because there is only one material with a constant refractive index in each layer. The only difference is that this layer should be assigned a finite thickness in RCWA and the layer structures are defined from top to bottom to calculate the field inside and at the interface of each layer.

In defining the grating in RCWA, its width has to be a constant in each layer, because RCWA needs to perform a Fourier transform for the grating, which requires the grating material to be the same width (the detailed methods for the Fourier transform are presented in the next part of this chapter). The solution used to define a non-rectangular grating is to divide the grating into several thin layers and allow the grating in each of these thin layers to have a constant width, as shown in Figure 3.3. The width of the grating in each layer increases or decreases gradually from bottom to top, and thus can define a trapezoid Al grating or any other complicated grating structure.

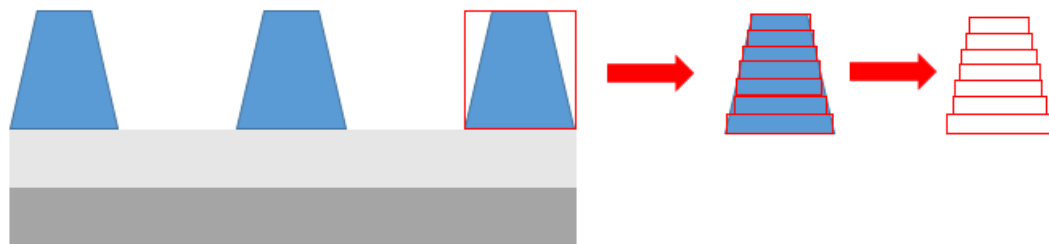


Figure 3.3 Definition for a trapezoid grating structure

3.1.3 Definition of the horizontal direction in RCWA

In the previous section, we discussed how to divide a homogenous layer or a grating layer into several thin layers with the same width. In this section, the method to perform the Fourier transform for the thin layer is introduced. Considering a 1D grating structure, for each thin layer of the grating, c_1 is used to present half the linewidth of gratings and c_2 is used to present the remaining width in one unit cell. The definitions of c_1 and c_2 are shown in Figure 3.4.

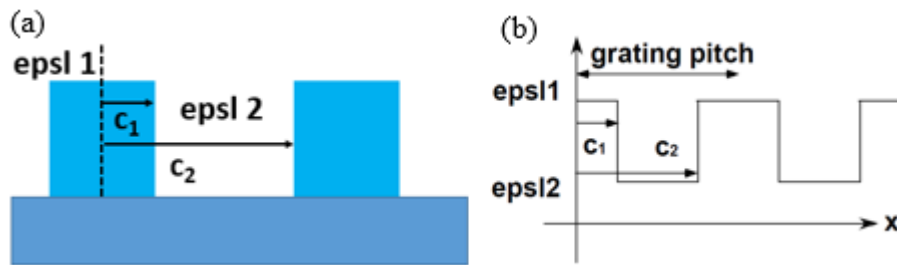


Figure 3.4 Definition of c_1 and c_2 for grating structure (a) in real space and (b) in epsilon space

The Fourier expansion of a unit cell of the thin layer can be described with the following equation:

$$F(K) = \int_0^{c_1} \varepsilon_1 e^{-iKx} dx + \int_{c_1}^{c_2} \varepsilon_2 e^{-iKx} dx + \int_{c_2}^p \varepsilon_1 e^{-iKx} dx \quad (3.1)$$

ε_1 and ε_2 are the permittivity of the grating material and the medium, p is the pitch of the grating structure; K is a continuous variable for a periodic structure evaluate at $n \frac{2\pi}{p}$ (n is from 0 to $m-1$ where m is the number of modes need to be considered in RCWA). As

it is very clear that $p=c_1+c_2$, the expansion in (3.1) can be simplified to:

$$F = \sum_0^{(m-1)} F(n) = \frac{i(\varepsilon_1 - \varepsilon_2)}{2\pi n} (e^{Kc_1} - e^{Kc_2}) \quad (3.2)$$

RCWA solves the eigenvalue problems using the Fourier expansion for each thin layer and can obtain the solution in a matrix form. From there, the total reflection, R, and total transmission, T, can be calculated, and the absorption is equal to $1-R-T$.

3.1.4 RCWA Code for Additional Layer in the Horizontal Direction

The RCWA codes described earlier in this chapter can deal only with a structure in which the combined layer includes just two materials. As shown in Figure 3.4, c_1 and c_2 are used to define the grating structure for two different materials (the grating and the space). If we want to simulate a more complicated structure, such as one with three different materials in the same layer, the Fourier expansion needs to be adjusted and more parameters need to be added. Figure 3.5 shows adding an additional layer to the outside

of the grating structure.

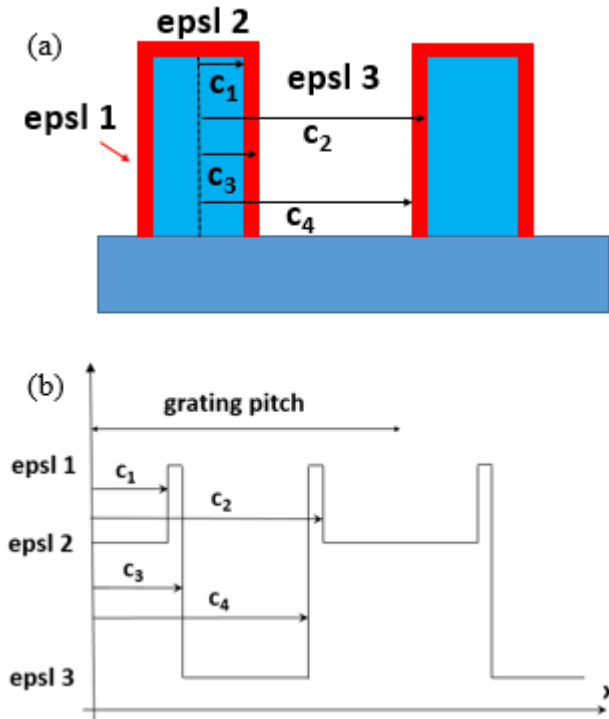


Figure 3.5 Additional layer for grating structure (a) in real space and (b) in epsilon space

c_3 and c_4 are added to describe the width of the additional layer and the Fourier expansion changes to:

$$F(K) = \int_0^{c_1} \varepsilon_2 e^{-iKx} dx + \int_{c_1}^{c_3} \varepsilon_1 e^{-iKx} dx + \int_{c_3}^{c_4} \varepsilon_3 e^{-iKx} dx + \int_{c_4}^{c_2} \varepsilon_1 e^{-iKx} dx + \int_{c_2}^p \varepsilon_2 e^{-iKx} dx \quad (3.3)$$

ε_1 is for the additional layer, ε_2 is for the grating material, and ε_3 is for the medium.

The equation can be simplified to:

$$F = \sum_0^{m-1} F(n) = \frac{i}{2\pi n} [(e^{Kc_4} - e^{Kc_1})(\varepsilon_1 - \varepsilon_2) - (e^{Kc_3} - e^{Kc_2})(\varepsilon_1 - \varepsilon_3)] \quad (3.4)$$

If the width of the additional layer reaches zero, which indicates that $\varepsilon_3 = \varepsilon_2$, $c_1=c_3$ and

$c_2=c_4$, then the expansion of Equation 3.4 will become the same as Equation 3.2, which is the condition without an additional layer. After adding two additional parameters, c_3 and c_4 , it is possible to extend the RCWA code's ability to handle more complicated structures, such that it can simulate a layer with three different materials.

3.1.5 Selecting the Correct Number of Modes

A detailed description of RCWA is not an integral part of this dissertation, but the way in which the number of modes was chosen needs to be considered in our simulation and is discussed below. In Equation 3.1, there is a parameter, m , that shows the modes of the Fourier expansion, which indicates how many truncation orders there are in the expansion. There has to be an odd number of modes, as equal numbers of positive and negative orders are retained (shown in Figure 3.6).

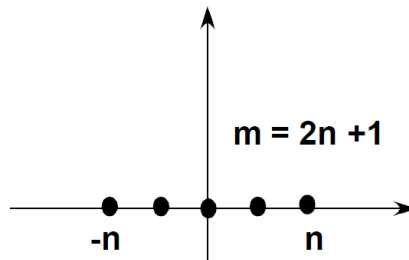


Figure 3.6 Number of modes in Fourier expansion

The number of modes, m , is a very important parameter in RCWA simulation. If the m is not large enough, RCWA does not provide an accurate solution for the simulation.

However, if an unnecessarily large m is selected, a lot of time is wasted (simulation time increases exponentially with increasing m). To select a reasonable number of modes, a series of RCWA simulations are performed with the exact same structure, but with different numbers of modes. Considering the two samples measured here (the WGP and resist grating), metallic structures usually require more modes in RCWA simulations with a result of the much higher index discontinues, so that if the number of modes is sufficient high for the WGP simulation, then it will also work for the resist grating simulation. Therefore, a simple Al grating structure on a fused silica substrate was defined to test the number of modes in RCWA. Figure 3.7 shows the simulation results with different numbers of modes at an incident angle of 45° using a 244 nm laser source. For both TM and TE polarizations, the simulation results become stable when there are more than ~ 45 modes.

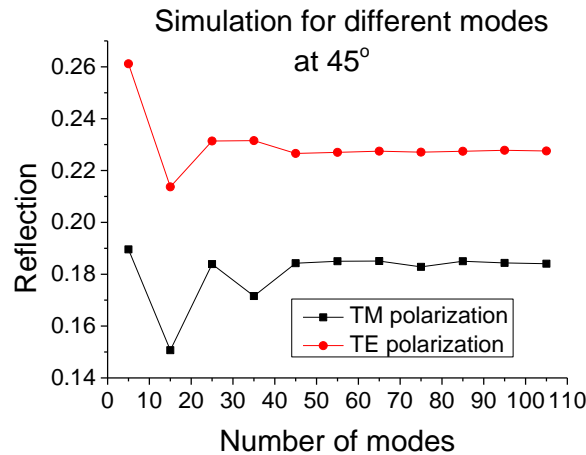


Figure 3.7 Simulation result for different modes with same structure at 45°

To check the conditions for a large range of angles, the reflection for the same grating structure was simulated with approximately 45 modes from 0.1° to 80° . The results are shown in Figure 3.8. Please note that because only one angle (45°) was simulated in Figure 3.7, the x-axis in Figure 3.7 is the number of modes. In Figure 3.8, the simulations were conducted for a range of angles, so the x-axis indicates those angles.

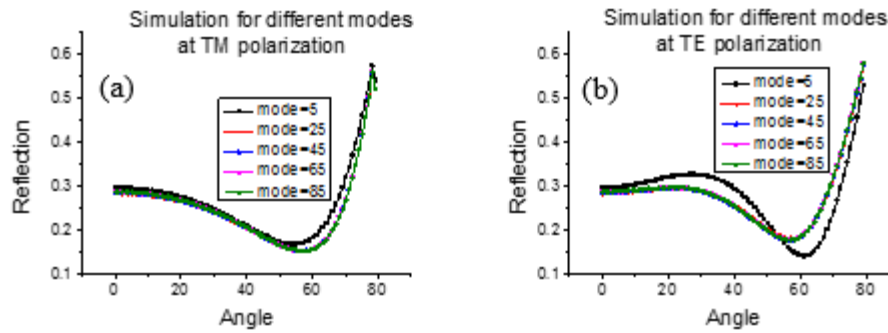


Figure 3.8 Simulation result for varying the number of modes in the RCWA simulation from 0.1° to 79.1°

Figure 3.8 shows that the reflection with mode=5 differs significantly from that of the other modes. Reflection with mode=5 is removed in Figure 3.9 and only reflection at small angle range is demonstrated to obtain an expanded view of the high modes simulations. The reflection graph becomes stable when mode m is larger than 65, $m=65$ was used in the following RCWA simulation for both the WGP and resist grating. When a much smaller scale structure is simulated for limitation study, the number of modes is checked again for the special structure.

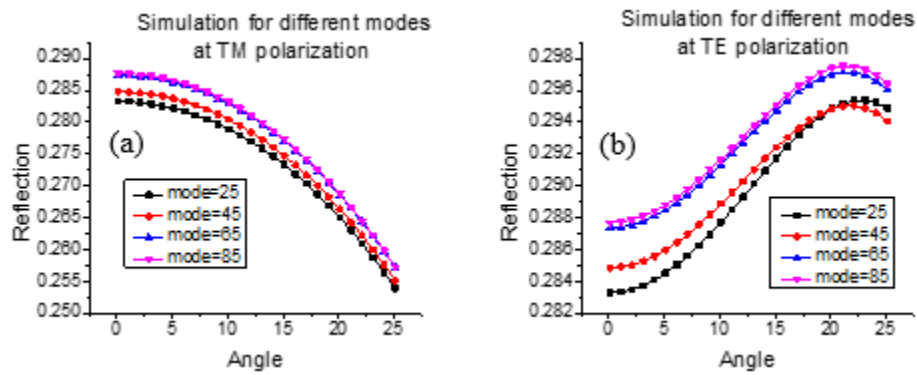


Figure 3.9 Simulation result for different modes with same structure at angle range from 0.1° to 25.1°

3.2 Scatterometry Measurements

3.2.1 Measurement setup

The basic requirement of the scatterometry setup is to track the diffraction from the sample surface while the incident angle of the light source is varied. A bread-board, two-rotation-stage scatterometry system was assembled to provide the mechanical flexibility necessary for the measurement. A large-area silicon detector was mounted on an arm extending from the bottom stage. The rotation speeds were adjusted, such that the detector on an arm that extended from the bottom stage tracked the reflection (0-order diffraction) from the sample on the top stage as the angle of incidence varied. This system also has the ability to track other diffracted orders (if available) and the intensity of light scattered out of the reflected beams by changing the rotation speed of the top stage and programming the motion of the stages. A single wavelength laser source was used. The scatterometry signal is invariant to the size of the beam, as long as many lines of the grating are illuminated to offer the ability to monitor inhomogeneity in the fabrication on scales from μm to cm. Measurement times in this apparatus were limited by the mechanical adjustments and settling times. A full angular scan (8° to 80°) takes approximately two minutes to complete. This time could be reduced significantly with attention to the experimental design, which will be discussed below. There is excellent repeatability (average repeatability for fixed parameters less than 0.2 nm) for multiple measurements of the same spot; measurements across the sample show some variability associated with sample inhomogeneity.

3.2.2 Reliability of measurement setup

Before the scatterometry setup was used to measure the real sample, a known measurement was used to test the reliability of the setup to determine whether the homemade tool provided good and accurate results. A blank glass slice without any coating layer on top was used as a test sample. The scatterometry setup shown above (see Figure 3.10) was used to measure this test sample in TE polarization using 244 nm laser source. After measurement, the reflection vs. angle graph was compared with the RCWA simulation and manual calculation of reflection from the interface between air and single homogenous glass layer. As shown in Figure 3.11, the measurement, RCWA simulation and manual calculation match nicely; thus, this test measurement proved the accuracy of the homemade scatterometry setup. The measurement result shows that no Fabry-Perot effect occurs in the glass slide. It is because glass has a high absorption coefficient at 244 nm so that all transmitted energy is absorbed in the glass surface.

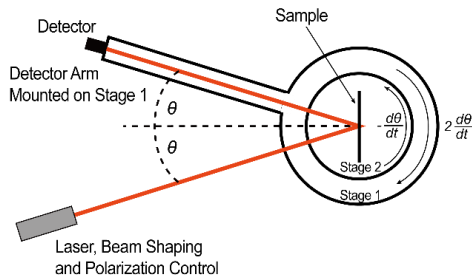


Figure 3.10 Schematic top view of scatterometry experimental system.

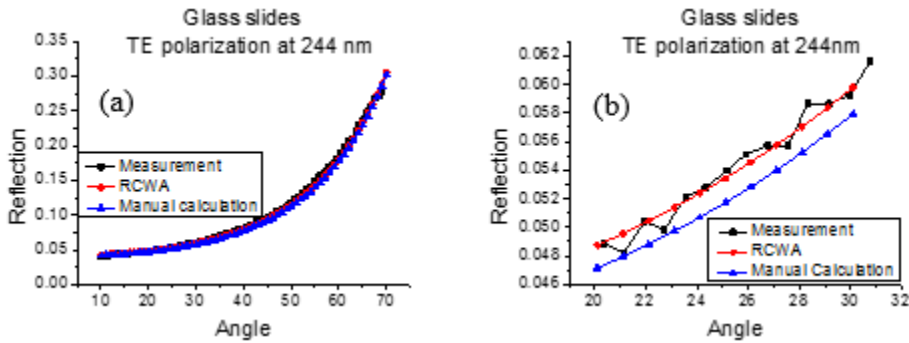


Figure 3.11 Test measurement on glass slide with TE polarization at 244 nm. (a) full angle range (b) expanded area

3.2.2.1 Reliability Check with Other FDTD Software

There are many approaches of simulation for reflection from multi-layer structures including Finite-Difference Time Domain (FDTD) method. FDTD is a numerical analysis method to find an approximate solution to the partial differential Maxwell's equations of the defined structure. The advantage of FDTD is that it can cover a wide frequency range in a single simulation and it can easily define the structure. The FDTD software introduced in this section is CST Microwave Studio which is widely used in simulating complicated 3D structure in industry and academia. Unlike in RCWA, the sample is not limited to a periodic structure or any shape. Figure 3.8 (a) demonstrates a single grating structure. The substrate could have a finite thickness, but it could also be assumed as infinite thick by defining a perfect matched layer (PML) at the bottom of substrate to absorb all the energy. CST can also simulate a "infinity" periodic structure by defining the single structure (Figure

3.12(a)) as a unit cell and the software could multiple the unit cell in x, y direction (Figure 3.12(b)).

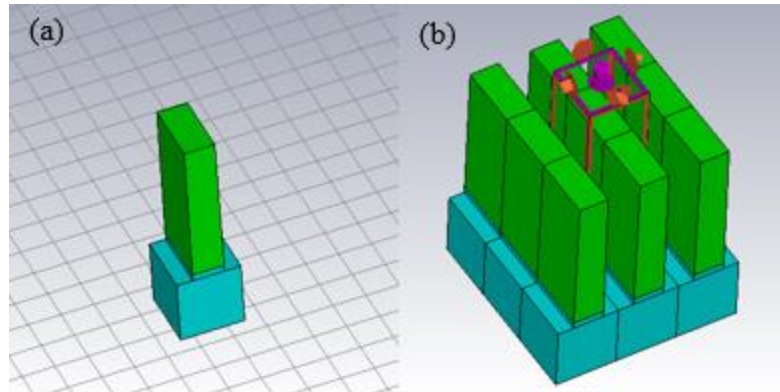


Figure 3.12 Structure definition in CST (a) single grating (b) periodic gratings

Although CST has more flexibility in structure definition, the calculation time is unacceptable for our scatterometry demands. For instance, for a single grating structure, the simulation time of CST is 100 times longer than that of RCWA. In our project, CST is only used to check the reliability of our RCWA result.

A CST simulation result for a single glass slide substrate at 244 nm comparing with our scatterometry measurement and RCWA simulation result is shown in Figure 3.13. Our scatterometry measurement is matched nicely with both RCWA simulation and CST simulation which indicates the reliability of our measurement system and reliability of our RCWA code.

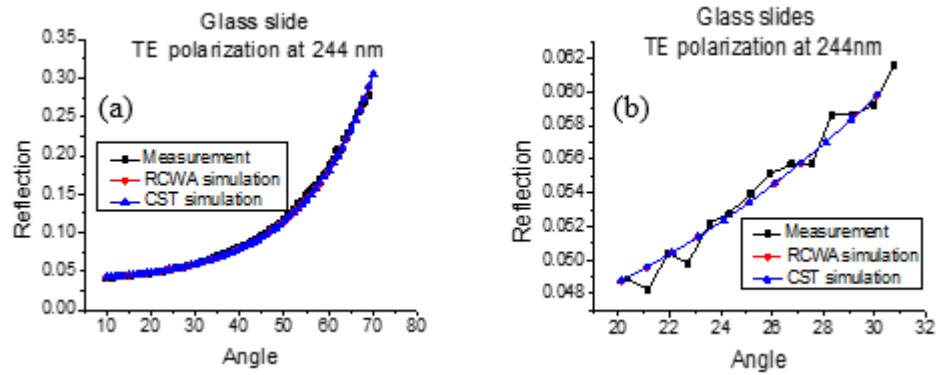


Figure 3.13 Comparison with Scatterometry measurement and simulation results with CST and RCWA (a) full angle range (b) enlarged angle range

3.3 Fitting Process

The fitting process is the final and most important step in scatterometry. It solves the inverse problem to find the structure parameter set that achieves the “best fitting results”.

These parameters are obtained by searching the lowest root mean square difference between measurement and simulation. All polarization conditions used in measurement are included in the analysis. The RMS difference is defined by:

$$Var(i) = \sqrt{\sum_n (x_n - x_{i,n})^2 / N} \quad (3.5)$$

where x_n is the measurement data point at the n^{th} incident angle, $x_{i,n}$ is the data point for the i^{th} simulation at the same incident angle of the measurement data point, and N is

the total number of data points. The best fitting result and parameter set appear at the minimum value of $\text{Var}(i)$.

3.3.1 Automatic fitting process

Several parameters could be used to define the sample structure and each must be optimized to find the best-fit result during the fitting process. The fitting process is a multi-parameter exercise so that it is not possible to manually approach the final result. Thus, an automatic modeling code must be used during the fitting process to obtain a fast and accurate result.

An initial parameter set needs to be specified as the starting point of the entire automatic process. These initial parameter set and a reasonable adjustable range of the parameters should be selected based on the results from other metrology studies, such as SEM, or the properties of the manufacturing tools, like pitch of the mask. For example, if the pitch of the mask used in NIL is 100 nm, then the initial pitch reading for this sample should be 100 nm with a ± 5 nm adjustable range. To calculate the result with the initial parameter sets, a first RMS result can be obtained and used as a reference number for the next step. Then, one of the parameters (Para A) is changed in positive (Para A+) and negative (Para A-) steps, for example, ± 0.2 nm, to obtain another two RMS results for these two steps. Comparing the RMS results from these three parameter numbers (Para A, Para A+, and

Para A-), a minimum RMS is selected and parameter A is updated to the number of the condition that has the minimum RMS. After the simulation of parameter A is completed, the code moves to the next parameter, B, and a similar process is run to identify the minimum RMS. The automatic process scans each of the parameters one by one. One cycle of the process is considered to be complete when the minimum RMS is found for the last parameter used in the geometry definition, and the second cycle begins again from Parameter A. When the minimum RMS remains the same for all parameters in one scanning cycle, the minimum RMS condition is found. It is possible that the minimum RMS condition is at a local minimum which is not the best fitting condition. The simulation is usually not matched with measurement in a local minimum condition with a large RMS. The initial parameter set need to be redefined to avoid this local minimum condition and repeat the automatic fitting process again with the new initial parameter set.

3.3.2 Library search

The automatic fitting process is helpful in finding the best fitting results for scatterometry when a sample is new, or when certain parameters of the sample are unknown. The problem is that the automatic process is time-consuming and thus is not desirable for real-time measurement.

When scatterometry is used for real-time quality control, the parameters of the structure are known already, and the adjustable range of the parameters is set as well. Because the range of all the parameters is clear, a library search⁶⁶ can help improve the fitting process dramatically. The basic idea of a library search is to complete all the calculations in advance, store all the simulation results in a digital library, and search the library for the best fitting result after the measurements are made. The method used to build the library is to calculate the Reflection vs. Angle for all the possible parameter sets within the adjustable range, and store the simulation results with the parameters used to define this structure. For example, if the pitch ranges from 99 to 101 nm in 1 nm steps, and the range of the linewidth is 49 to 51 nm in 1nm steps, then there is a total of nine parameter sets (3x3) and nine simulation results in the library. With the library search, real-time scatterometry measurement becomes possible. In our case, the laptop used for simulation is with a 2.40GHz i7 CPU and 8GB RAM. The fitting process takes less than 1 second using library search for over 10000 parameter variations.

4. Experiments and Results

This chapter presents the measurement results of scatterometry for the WGP samples and resist grating samples and discusses the several steps used to improve the fitting process of the RCWA code to obtain more accurate results.

4.1 Wire Grid Polarizer

As mentioned in Chapter 2, the WGP sample consisted of periodic Al lines on a fused silica substrate. Although angles between the grating direction and the photon polarizations other than 0^0 or 90^0 can be handled both in RCWA simulations and with the scatterometry setup shown in Chapter 3, we focus on the parallel conditions and perpendicular conditions between grating and polarization directions for all of our samples. If one considers only the parallel or perpendicular conditions between the gratings and polarizations, there are four conditions as shown in Figure 4.1. TM polarization of the laser indicates the electric field in the incident plane and TE polarization indicates the electric field perpendicular to the incident plane. We define parallel conditions when grating direction is parallel to polarization and perpendicular conditions when grating direction is perpendicular to polarization.

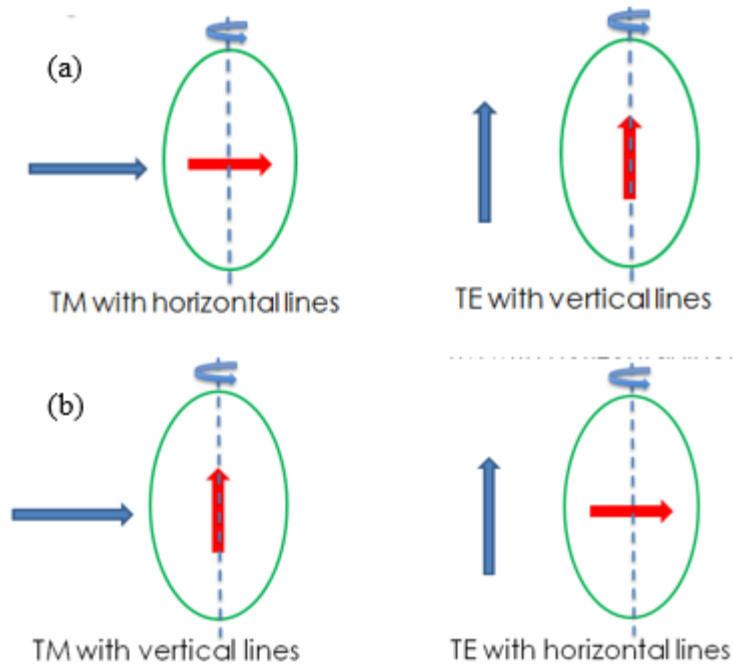


Figure 4.1 the red line is grating direction and the blue line is polarization direction (a) Parallel conditions between gratings and polarizations (b) Perpendicular conditions between gratings and polarizations

Recalling the characteristics of WGP introduced in Chapter 2, WGP can reflect the beam when the polarization direction is parallel to the metal wires and transmit it when the polarization direction is perpendicular to the metal wires. Because of this functionality of the WGP, approximately 90% of the energy is reflected when the laser polarization is perpendicular to the gratings, which makes the variation in reflection very small. Figure 4.2 shows the results of simulations for the parallel and perpendicular conditions of the

4. Experiments and Results

same structure. The reflection changes less than 10% in parallel conditions, while it changes more than 60% in perpendicular conditions (incident angles from 0.1° to 79.1°), which means the perpendicular conditions are more sensitive than are the parallel conditions. Therefore, all of the measurements for the WGP were performed under perpendicular conditions with a horizontal plane of incidence: TM polarization with

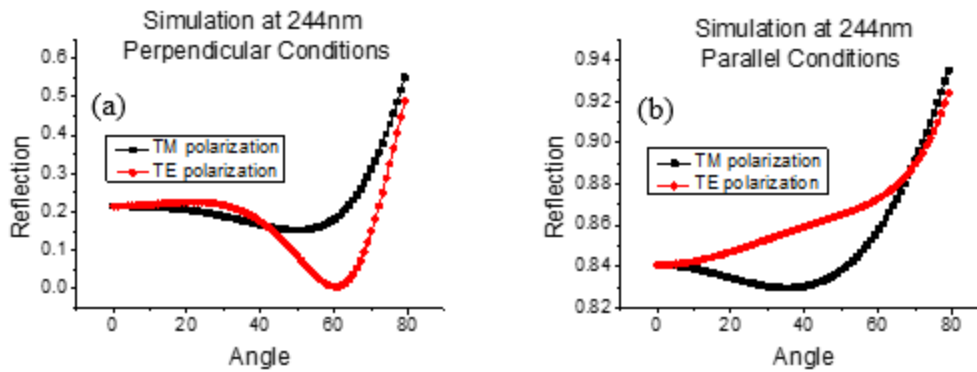


Figure 4.2 Simulations at 244 nm (a) Perpendicular conditions (b) Parallel conditions

vertical grating and TE polarization with horizontal grating.

4.1.1 Measurements at Multiple Wavelengths

The WGP structure we measured consists nominally of 50 nm lines and 50 nm spaces in a 200-nm thick Al film on a fused silica substrate ($p = 100$ nm). Four different laser sources were used at 244 nm (doubled Ar-ion laser; $\lambda/p = 2.4$); 405 nm (multimode diode laser; $\lambda/p = 4.1$); 633 nm (TEM_{00} single mode HeNe laser; $\lambda/p = 6.3$), and 982 nm (multimode diode laser; $\lambda/p = 9.8$). The specular reflection from the sample was

4. Experiments and Results

measured for angles that ranged from 8° to 80° for the two perpendicular conditions, as mentioned above (TM polarization with vertical grating and TE polarization with horizontal grating). The measurements at the four wavelengths are shown in Figures 4.3 to 4.6.

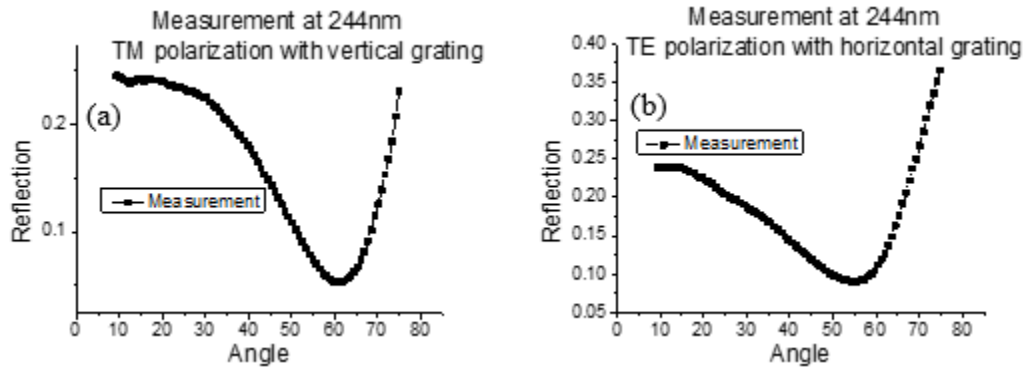


Figure 4.3 Measurement results at 244 nm (a) TM polarization (b) TE polarization

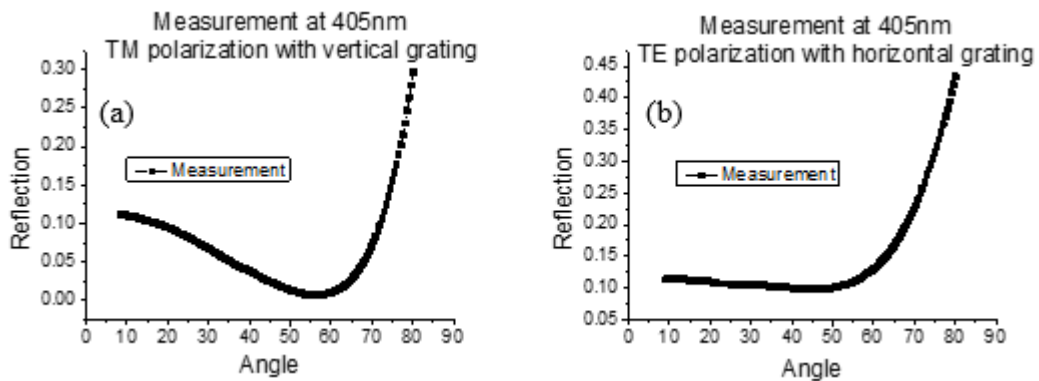


Figure 4.4 Measurement results at 405 nm (a) TM polarization (b) TE polarization

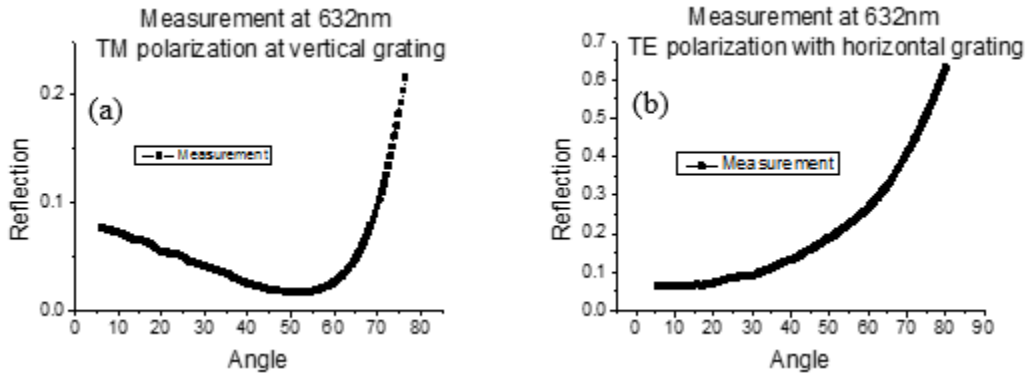


Figure 4.3 Measurement results at 632 nm (a) TM polarization (b) TE polarization

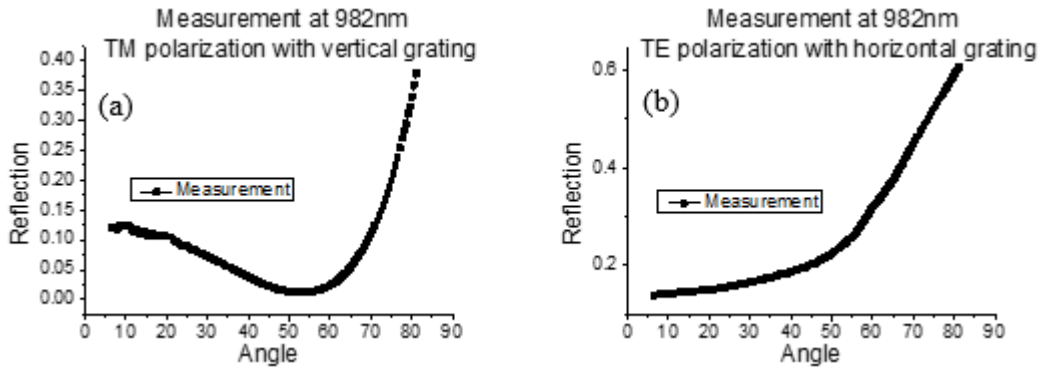


Figure 4.4 Measurement results at 982 nm (a) TM polarization (b) TE polarization

4.1.2 Effective Medium Comparison

Scatterometry is an indirect measurement, which means that the measurement is not a direct image of the sample surface, but a simulation of the structure through the dependence of the reflection vs. angle. For an effective scatterometry measurement, some fingerprints in the measurement figure should contain surface information. This is not

always true when the ratio of λ/p (wavelength / pitch) becomes increasingly large. When the photon used to detect the grating structure is too large, the reflection contains no information about the shape of the structure, but only information about its effective refractive index. In this case, the grating structure is considered an effective plane layer with an effective refractive index, and all the structure information, except the fill factor (critical dimension / pitch) of the grating, are lost in the scatterometry measurement. Before we moved to the process of fitting our scatterometry measurements at the four different wavelengths, the measurement results were compared with an effective medium approach to ensure that the wavelengths we used are able to detect our WGP samples.

There are several different methods and equations for effective medium approximation, which has a base medium with refractive index n_1 , an inclusion medium with refractive index n_2 , and a volume fraction σ of the inclusion medium. The volume fraction is between zero and unity ($0 < \sigma < 1$). We chose two common methods to compare our measurement results: the Maxwell-Garnett Theory and Bruggeman's Model.

For the Maxwell-Garnett Theory, the equation to calculate effective index is:

$$n_{eff}^2 = n_1^2 \left[1 - \frac{3\sigma(n_1^2 - n_2^2)}{2n_1^2 + n_2^2 + \sigma(n_1^2 - n_2^2)} \right] \quad (4.1)$$

For Bruggeman's Model, the equation to calculate effective index is

$$1 - \sigma = \frac{\left(\frac{n_{eff}^2}{n_1^2} - \frac{n_2^2}{n_1^2} \right)}{\left[\left(\frac{n_{eff}^2}{n_1^2} \right)^{\frac{1}{3}} \left(1 - \frac{n_2^2}{n_1^2} \right) \right]} \quad (4.2)$$

4. Experiments and Results

n_1 is the index of the base medium, which is air ($n_1=1$) for WGP, n_2 is the index of inclusion medium, which is the index of Al for the WGP which is $0.17613+2.8504i$, $0.47951+4.7724i$, $1.2667+7.2811i$ and $1.5711+9.0597i$ at wavelength of 244 nm, 405 nm, 632.8 nm and 982 nm, and σ is the fraction coefficient of the inclusion medium which is set at 0.5.

After obtaining the effective refractive index, we entered it into RCWA to calculate the reflections from 0.1° to 79.1° . The fill fraction coefficient chosen for the WGP was 0.5, and the thickness of this effective medium was equal to the thickness of the Al grating, which was 200 nm. Figures 4.7 to 4.10 show the comparison of our measurement results with those from the Maxwell-Garnett Theory and Bruggeman's Model.

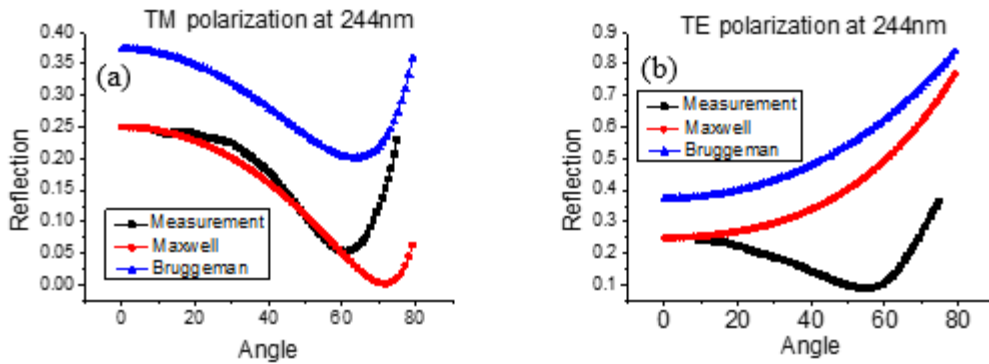


Figure 4.5 Measurement and effective medium approaches at 244 nm (a) TM polarization (b) TE polarization

4. Experiments and Results

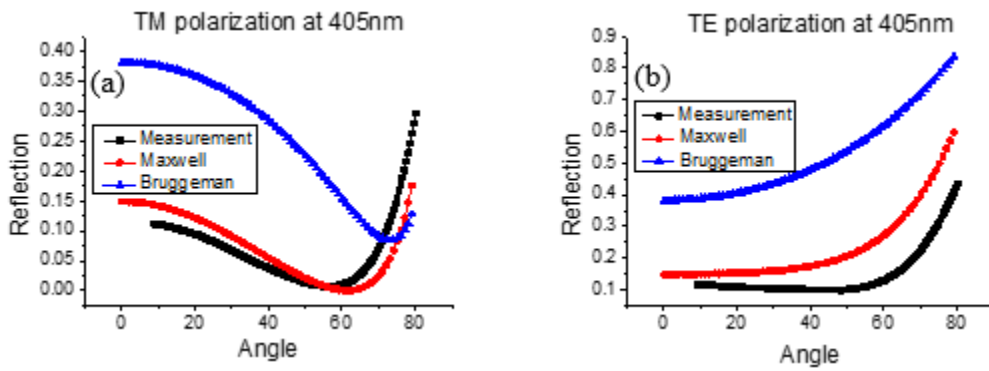


Figure 4.8 Measurement and effective medium approaches at 405 nm (a) TM polarization (b) TE polarization

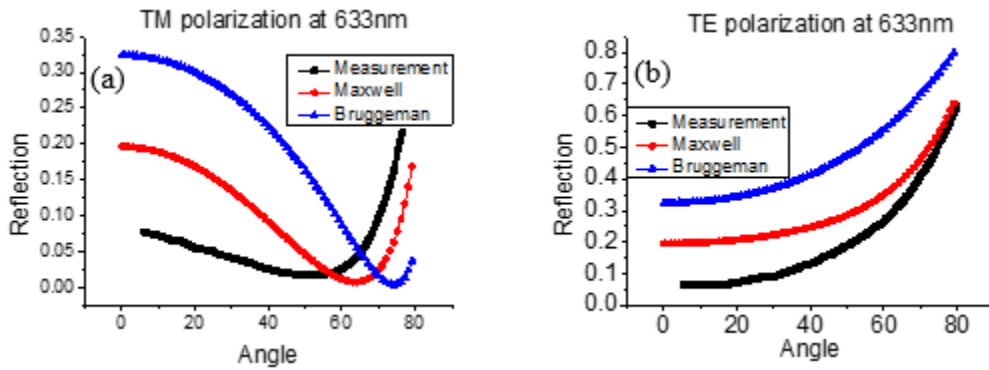


Figure 4.7 Measurement and effective medium approaches at 633 nm (a) TM polarization (b) TE polarization

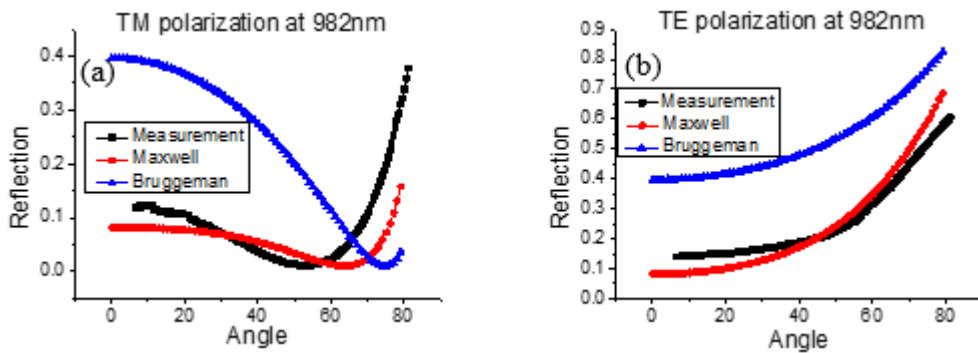


Figure 4.6 Measurement and effective medium approaches at 982 nm (a) TM polarization (b) TE polarization

We noted that there was a significant difference between the scatterometry measurements and the effective medium approximations, which indicates that there is structure information in the scatterometry measurements at all four wavelengths and measurements are more sensitivity in TM polarization. Even with a 982 nm laser, scatterometry can still obtain information for the 50 nm half pitch WGP sample ($\lambda/p=10$). We also noted that the measurement at 982 nm was much closer to the effective medium approximation than were the results at the other wavelengths. This indicates that the scatterometry measurement is more sensitive to the surface structure at shorter than longer wavelengths and scatterometry has a limit when difference between measurement and effective medium approaches is smaller than the noise of the system.

4.1.3 Simple Grating Definition

The measurements at the four different wavelengths were shown earlier in this chapter, which demonstrate the graphs for the Reflection vs. Angle in the approximate range of 8° to 80° . These graphs include fingerprints showing information about the structure, which differs at different wavelengths. These fingerprints are used in the fitting process to determine the parameter readings for the sample structure.

Before running the RCWA simulation, we needed to define the sample structure.

Generally, when defining a periodic grating sample, four parameters are needed to present the structure: Pitch (P), Bottom width (BW), Top width (TW), and Grating

4. Experiments and Results

height, which was the Al thickness in our case (AI). Figure 4.8 shows the SEM image for the WGP. After looking at the SEM image, we noted that the fused silica substrate was etched by approximately 20 nm, which is formed in dry etching process to remove the oxide hard mask. A parameter for the fused silica undercut (FS) was considered in the RCWA coding. A sketch of the grating definition is also shown in Figure 4.11.

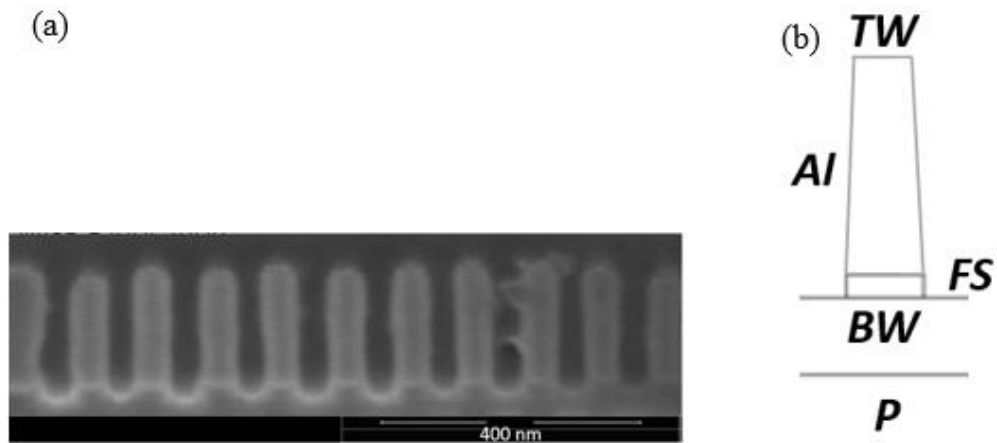


Figure 4.9 (a) SEM image for WGP (b) Simple definition of WGP with five parameters

4.1.3.1 Fitting Process at Simple Grating Definition

As mentioned in Chapter 3.3.1, an automatic fitting process was run to find the minimum RMS conditions between the measurement and simulation, which is considered the best fitting result. The minimum step for P and AI was 0.1 nm and was 0.2 nm for BW , TW , and FS . Figure 4.12 shows the best fitting result at 405 nm.

The parameter readings for this best fitting result were $P=87.60$ nm, $BW=38.60$ nm, $TW=38.60$ nm, $AI=189.50$ nm, and $FS=16.20$ nm. While the overall shape of the scatter fingerprint was reproduced, there were significant deviations between the measurement and simulation. With the simple grating definition, the simulation cannot approach the measurement, because five parameters are not sufficient to present the structure and some information about the surface is lost in the simulation. Therefore, more parameters had to be added in the RCWA coding.

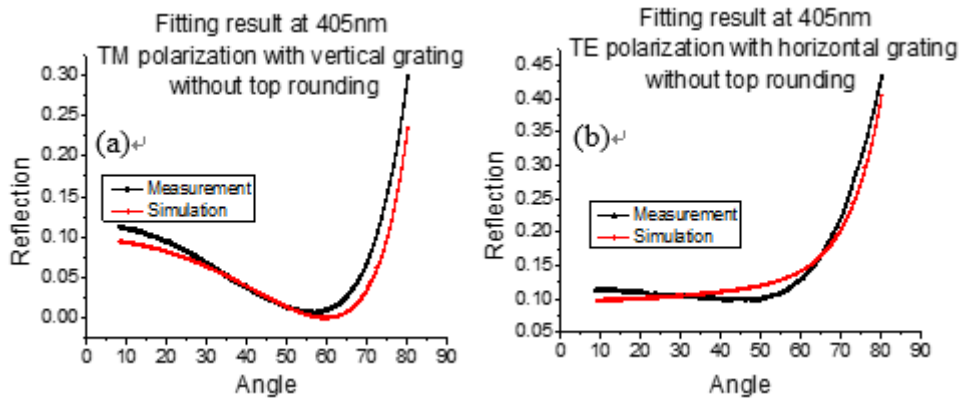


Figure 4.10 Grating structure without top rounding (a) TM polarization (b) TE polarization

4.1.4 Structure Definition Improvement

4.1.4.1 Top Rounding Structure

During the WGP fabrication process discussed in Chapter 2.1.2, the Al film was etched to form the grating structure. The etching process can form a round structure on the top of the metal grating, which also can be seen in the SEM image in Figure 4.11(a). We added a trapezoidal structure at the top of the Al lines to account for the rounding evident in the SEM results, and added two more parameters: horizontal rounding (**HR**) and vertical rounding (**VR**). Thus, there were seven parameters for the grating structure. The improved grating definition is shown in Figure 4.13.

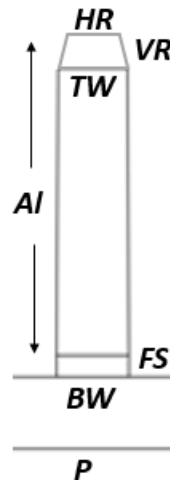


Figure 4.11 Definition of grating structure with top rounding structure with seven parameters.

4. Experiments and Results

After adding **HR** and **VR** in the simulation, we performed the fitting process for 244, 405, and 633 nm again. The minimum step was 0.10 nm for **P**, **AI**, and **VR**, and 0.20 nm for **BW**, **TW**, **HR**, and **FS**. Figures 4.14 to 4.16 show the new fitting results at the three different wavelengths.

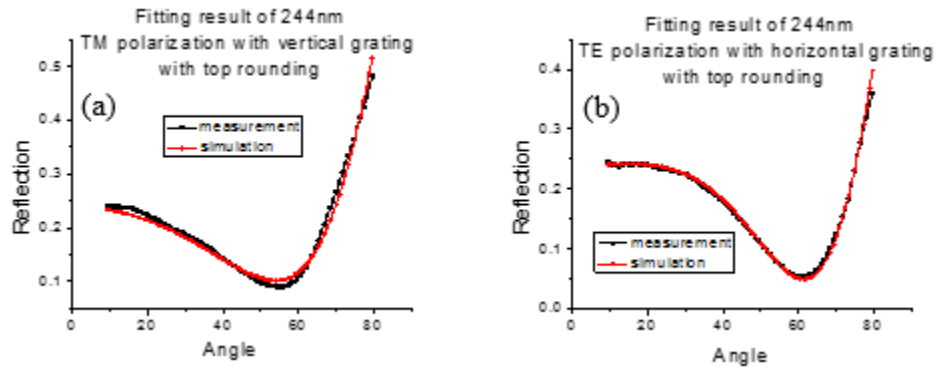


Figure 4.12 Fitting results for 244 nm measurements: (a) TM polarization with vertical grating, (b) TE polarization with horizontal grating

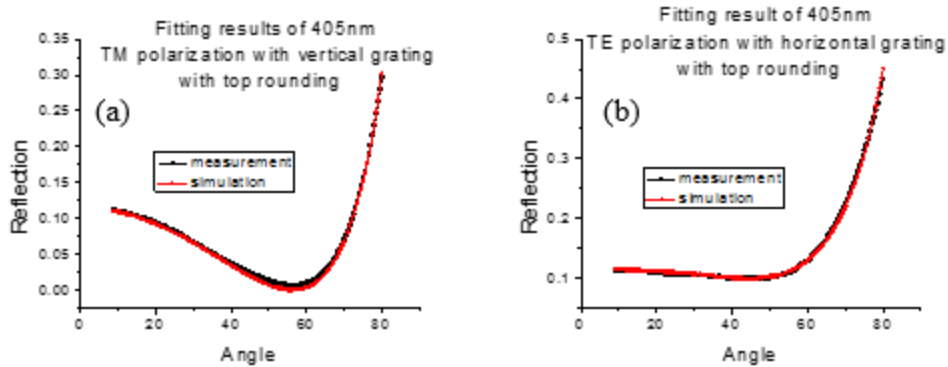


Figure 4.14 Fitting results for 405 nm measurements: (a) TM polarization with vertical grating, (b) TE polarization with horizontal grating

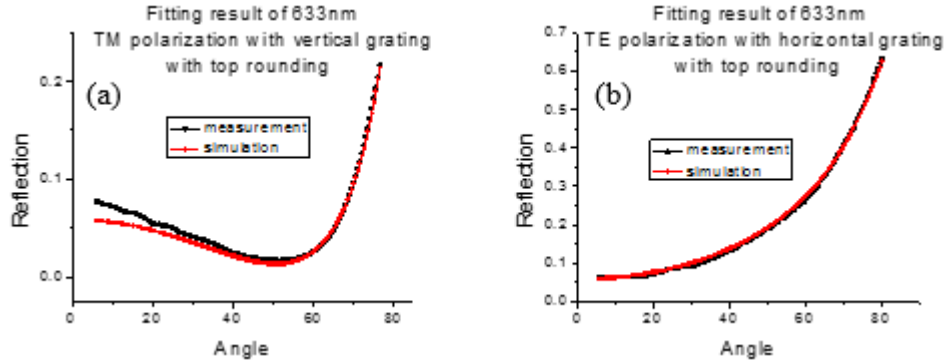


Figure 4.15 Fitting results for 633 nm measurements: (a) TM polarization with vertical grating, (b) TE polarization with horizontal grating

4.1.4.1.1 Uncertainty Error Bar Determination

There are several aspects to the uncertainty in the scatterometry measurements and simulation. The total uncertainty can be described as:

$$\sigma_{total} = \sqrt{\sigma_{elec}^2 + \sigma_{drift}^2 + \sigma_{laser}^2 + \sigma_{sensitivity}^2} \quad (4.3)$$

where σ_{elec} is the uncertainty from electronic noise, σ_{drift} is the uncertainty from mechanical system error and drift during the measurement, σ_{laser} is the uncertainty from the laser intensity and pointing changes during the measurement, and $\sigma_{sensitivity}$ is defined as $\pm 5\%$ difference from the minimum RMS reading in the simulation. Multiple independent measurements were taken under the same conditions on the same sample area, and very good repeatability was obtained in our scatterometry setup with a laser power of $\sim 0.2\text{mW}$ at 405 nm. The fitting results for the parameters at each single measurement were identical, which indicates that σ_{elec} and σ_{drift} were negligible. The laser intensity was monitored during the measurement and the reflectivity normalized to any

4. Experiments and Results

variation of intensity, so σ_{laser} can also be neglected. Thus, for our conditions, the total uncertainty was simplified to:

$$\sigma_{\text{total}} \approx \sigma_{\text{sensitivity}} \quad (4.4)$$

where $\sigma_{\text{sensitivity}}$ was defined as the change in a fitting parameter that resulted in a 5% increase from the minimum variance when only one parameter was changed and the others remained fixed.

4.1.4.1.2 Discussion

The parameter sets for the best fitting result are shown in Table 4.1. After adding a top rounding structure and two additional parameters to our structure definition, the simulation results were much closer to the measurement results for all three wavelengths. The two top rounding parameters, **HR** and **VR**, improved the definition of the grating structure and offered extra flexibility in the fitting process. As shown in Table 4.1, the three wavelengths all provided similar, but not overlapping results, which confirms the ability of scatterometry to measure the periodic grating structure even with a beam wavelength several times larger than the pitch ($\lambda/p = 2.40, 4, 6.30$).

Table 4.1 Scatterometry fitting results with top rounding.

(nm) nm □	<i>P</i>	<i>BW</i>	<i>TW</i>	<i>AI</i>	<i>FS</i>	<i>HR</i>	<i>VR</i>
244	95.5±0.2	38.0±0.4	61.0±0.4	222.6±0.5	37±1	33.4±0.2	14.3±0.3
405	92.3±0.2	44.2±0.2	52.8±0.2	217.3±0.5	29±2	25.6±0.8	20.7±0.4
633	93.3±0.3	50.8±0.4	62.6±0.4	189.7±0.5	28±2	33.8±1.4	18.7±0.6
AVER	93.7	44.3	58.8	209.8	31.3	30.9	17.9

(nm) nm □	<i>P</i>	<i>BW</i>	<i>TW</i>	<i>AI</i>	<i>FS</i>	<i>HR</i>	<i>VR</i>
244	95.5±0.2	38.0±0.4	61.0±0.4	222.6±0.5	37±1	33.4±0.2	14.3±0.3

4. Experiments and Results

The pitch readings from all three wavelengths were very similar, at approximately 94 nm. However, some other major parameters of the grating structure, including the Al thickness (*AL*), line width (*BW*), and top width (*TW*) at the three wavelengths still had non-negligible differences. Comparing with average value of each parameter, the parameter outside three-sigma range (three times of error bar) is marked in red in Table 4.1. There are two-thirds of parameters outside the range indicating that there still were missing parameters in our structure definition.

Initially, we used a poor multi-mode 405 nm laser in the scatterometry apparatus, which we marked as the old 405 nm source. The fitting results from those measurements were considerably different from both the 244- and 633-nm results, especially for the pitch and the fused silica undercut. The fitting results improved significantly and showed consistent readings for the pitch and fused silica undercut when we switched to an improved 405 nm laser, although it still was not a single TEM₀₀ mode source, but had a smaller divergence angle and a better coherence length. A lens is also placed in path to reduce divergence angle of laser beam, which impacts the measurements at high angles of incidence where the beam spot size at the sample is enlarged.

Table 4.3 Fitting results of two different 405 nm laser

(nm) \ (nm)	<i>P</i>	<i>BW</i>	<i>TW</i>	<i>Al</i>	<i>FS</i>	<i>HR</i>	<i>VR</i>
Old 405	84.8	43.4	48.8	242.5	NA	19.6	38.3
New 405	92.3	44.2	52.8	217.3	29	25.6	20.7

(nm) \ (nm)	<i>P</i>	<i>BW</i>	<i>TW</i>	<i>Al</i>	<i>FS</i>	<i>HR</i>	<i>VR</i>
Old 405	84.8	43.4	48.8	242.5	NA	19.6	38.3

4.1.4.2 Al₂O₃ layer

It is well known that a thin, self-limiting native oxide layer will form when an Al grating is exposed to air for a long period of time, hence the fitting results (Reflection vs. Angle) will have large difference between the structure definitions with and without Al₂O₃ layer because there is a large variation in the refractive index between Al and Al₂O₃ (index of Al is 0.50+4.90i and index of Al₂O₃ is 1.78 at 405 nm). A 4-nm thick layer⁶⁷ of Al₂O₃ covering the surface of the Al grating was used in the simulation to improve the accuracy and sensitivity of the scatterometry fitting results. The detailed method used to add this fixed 4-nm thick Al₂O₃ “skin” around the three sides of the Al structure exposed to air in the RCWA has been described in Chapter 3.1.4.

First, we wanted to determine the influence of the Al₂O₃ layer and to what degree the simulation results changed after the Al₂O₃ layer was added. The exact same grating parameter sets were used to simulate the conditions with and without the Al₂O₃ layer and for the condition with Al₂O₃, the 4 nm thick outside the Al parts in three directions (left side wall, right side wall, and top) were replaced with Al₂O₃. The detailed parameters for the grating structures with and without Al₂O₃ were $P = 98$ nm, $BW = 44$ nm, $TW = 44$ nm, $AI = 220$ nm, $FS = 20$ nm, $HR = 30$ nm, and $VR = 15$ nm. The TW , BW , and AI parameters of the grating quoted included both the Al grating line and the Al₂O₃ skin. As shown in Fig. 4.17, simulations at 405 nm demonstrated that inclusion of the Al₂O₃ overcoating layer had a significant influence on the scatterometry measurements across

4. Experiments and Results

the entire incident angle range, and both the reflection intensity and the shape of the reflection vs. angle graph changed considerably. This indicates that the Al_2O_3 layer is an important parameter for the WGP structure and cannot be ignored in the RCWA simulation.

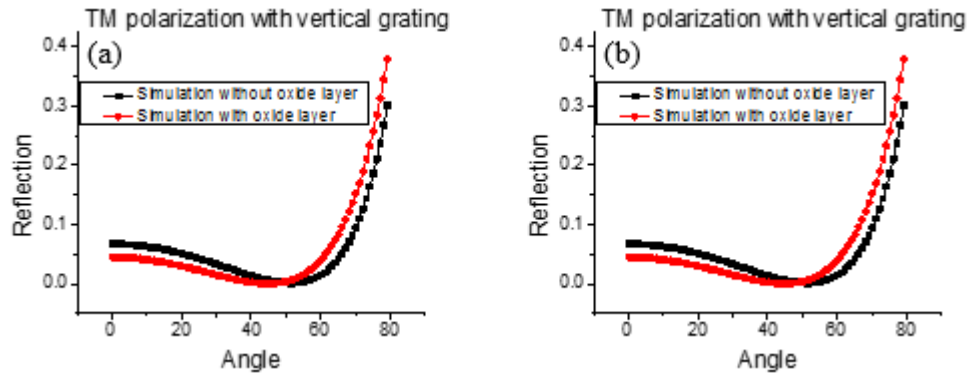


Figure 4.16 Comparison of the simulation results with and without the Al_2O_3 layer.

4.1.4.2.1 Fitting Results with Top Rounding and Al₂O₃

The minimum step for *P*, *Al*, and *VR* was 0.10 nm, and that for *BW*, *TW*, *HR*, and *FS* was 0.20 nm. Figures 4.18 to 4.21 show the fitting results at 244, 405, 633, and 982 nm and Table 4.3 shows the detailed parameter readings of the best fitting results at these four wavelengths.

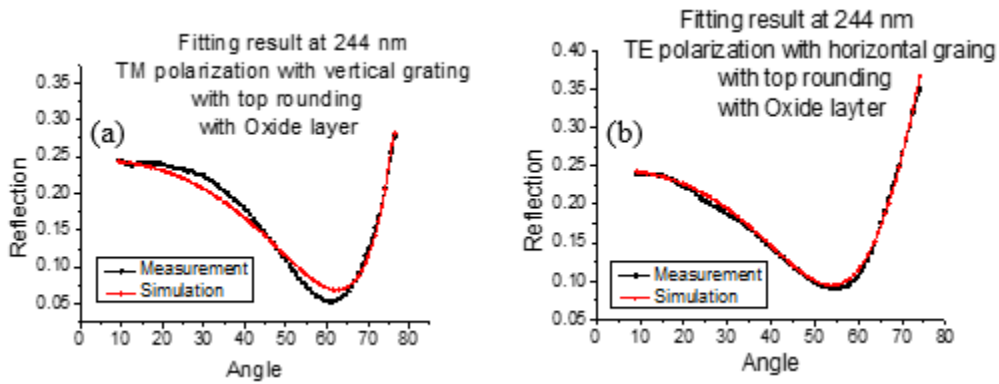


Figure 4.17 Fitting results for 244 nm measurements: (a) TM polarization with vertical grating, (b) TE polarization with horizontal grating

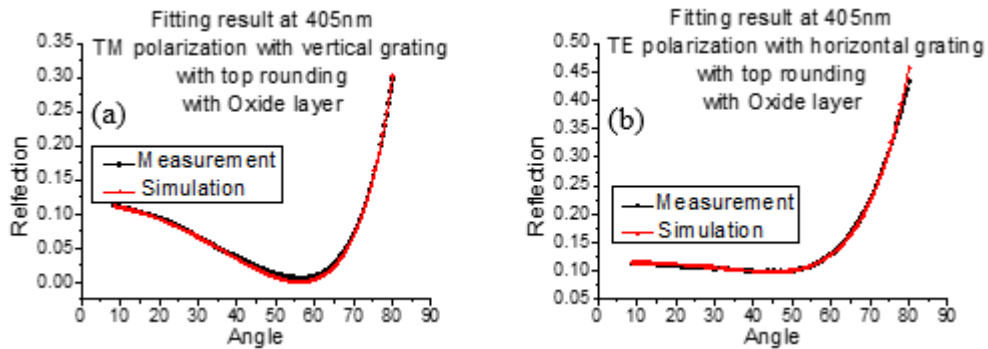


Figure 4.18 Fitting results for 405 nm measurements: (a) TM polarization with vertical grating, (b) TE polarization with horizontal grating

4. Experiments and Results

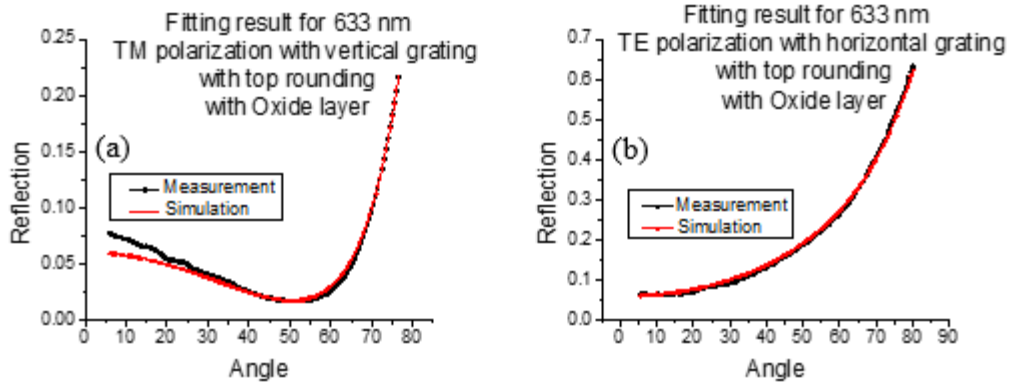


Figure 4.19 Fitting results for 633 nm measurements: (a) TM polarization with vertical grating, (b) TE polarization with horizontal grating

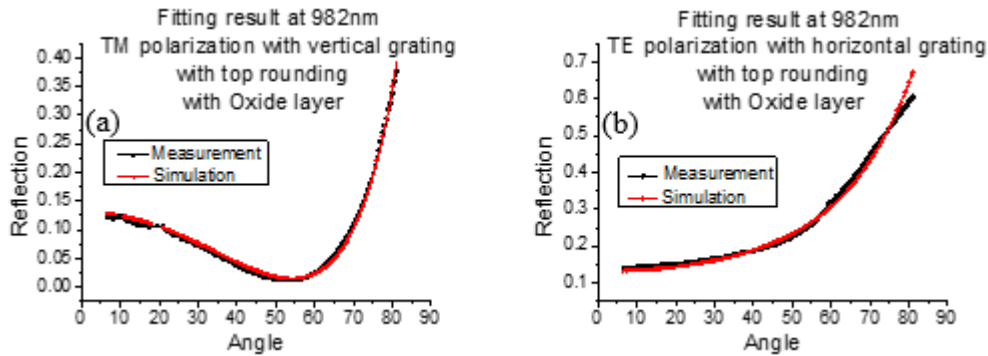


Figure 4.20 Fitting results for 982 nm measurements: (a) TM polarization with vertical grating, (b) TE polarization with horizontal grating

After including the Al_2O_3 layer for the WGP simulations, the fitting results of the four wavelengths were matched very well. Even for the longest wavelength, a 982 nm laser ($\lambda/p = 9.82$), scatterometry measurement still includes characteristic structure information. The parameters outside three-sigma range are also marked in red.

Comparing with the results from our previous results in Table 4.1 which didn't include the Al_2O_3 layer in the simulation, the results with the Al_2O_3 layer demonstrated better

4. Experiments and Results

correlations. The average pitch of the results without the Al₂O₃ layer was 93.7 nm, and was 97.8 nm with the Al₂O₃ layer while the e-beam written master grating was specified at 100 nm.

Table 4.5 Scatterometry fitting results of WGP with Al₂O₃

λ (nm) \ (nm)	<i>P</i>	<i>BW</i>	<i>TW</i>	<i>AI</i>	<i>FS</i>	<i>HR</i>	<i>VR</i>	<i>Var</i>
244	98.3±0.2	43.0±0.3	63.2±0.4	203±0.6	31.5±1.0	18.2±2.4	10.3±0.3	8.80x10 ⁻³
405	97.2±0.4	49.4±0.2	58.6±0.4	208.3±0.9	22.9±2.2	25.8±1.2	14.8±0.6	3.79x10 ⁻³
633	97.5±0.7	52.4±1.4	68.2±1.0	205.0±0.9	25.3±2.5	18.6±3.4	30.4±1.8	5.85x10 ⁻³
982	97.5±1.0	49.4±1.0	69.2±0.4	203.1±5.4	14.4±7.4	20.6±10.0	8.7±2.8	7.38x10 ⁻³
Aver	97.6	48.6	64.8	204.9	23.5	20.8	15.5	

In order to quantify the improvement in the fit after considering Al₂O₃, a parameter Δ is

defined to calculate the variance across wavelength.

λ (nm) \ (nm)	<i>P</i>	<i>BW</i>	<i>TW</i>	<i>AI</i>	<i>FS</i>	<i>HR</i>	<i>VR</i>	<i>Var</i>
244	98.3±0.2	43.0±0.3	63.2±0.4	203±0.6	31.5±1.0	18.2±2.4	10.3±0.3	8.80x10 ⁻³
405	97.2±0.4	49.4±0.2	58.6±0.4	208.3±0.9	22.9±2.2	25.8±1.2	14.8±0.6	3.79x10 ⁻³
633	97.5±0.7	52.4±1.4	68.2±1.0	205.0±0.9	25.3±2.5	18.6±3.4	30.4±1.8	5.85x10 ⁻³
982	97.5±1.0	49.4±1.0	69.2±0.4	203.1±5.4	14.4±7.4	20.6±10.0	8.7±2.8	7.38x10 ⁻³
Aver	97.6	48.6	64.8	204.9	23.5	20.8	15.5	

$\Delta = \sqrt{\frac{\sum (Average - x_i)^2}{N}}$

and N is the number of wavelengths used in the measurement. The parameter sets for the

conditions with and without the Al₂O₃ layer are given in Tables 4.1 and 4.3. The major

parameters, *P*, *BW*, *TW*, and *AI*, all showed significant improvements in cross-

correlations between the different wavelength measurements when the Al₂O₃ layer was

included in the simulation model (shown in Table 4.4); the *FS*, *HR*, and *VR* parameters

were connected more subtly to the scatterometry measurements and exhibited relatively

larger differences across wavelengths. To date, we have used a fixed, 4 nm Al₂O₃

thickness; in future work, we will extend the analysis to include varied thicknesses,

4. Experiments and Results

which will likely improve the cross-wavelength correlations further. The differences between the parameter values extracted at the different wavelengths were larger than the $\sigma_{sensitivity}$ suggesting that the model did not yet include all of the parameters required to describe the experimental results fully.

Table 4.7 Comparison of parameter variances at different wavelengths for the WGP with and without the Al₂O₃ layer

Δ	ΔP	ΔBW	ΔTW	ΔAI
With Al ₂ O ₃	0.42%	7.1%	6.5%	1.0%
Without Al ₂ O ₃	1.42%	11.8%	7.3%	6.9%

4.1.4.2.2 Sensitivity of scatterometry

Δ	ΔP	ΔBW	ΔTW	ΔAI
With Al ₂ O ₃	0.42%	7.1%	6.5%	1.0%
Without Al ₂ O ₃	1.42%	11.8%	7.3%	6.9%

In order to understand the response of scatterometry when the parameters were changed, we conducted simulations in which only one parameter among the four major parameters (P , BW , TW and AI) varied at a time in the structure definition with the top rounding structure and the Al₂O₃ layer. The initial parameter sets are the average readings in Table 4.3: $P = 97.6$ nm, $BW = 48.6$ nm, $TW = 64.8$ nm, $AI = 204.9$ nm, $FS = 23.5$ nm, $HR = 20.8$ nm and $VR = 15.5$ nm. The step of parameter changing is $\pm 5\%$: $\Delta P = \pm 4.9$ nm, $\Delta BW = \pm 2.4$ nm, $\Delta TW = \pm 3.2$ nm and $\Delta AI = \pm 10.2$ nm. Figures 4.22 to 4.25 show the simulation results with variation of seven parameters for four different wavelengths (244, 405, 633, and 982 nm).

4. Experiments and Results

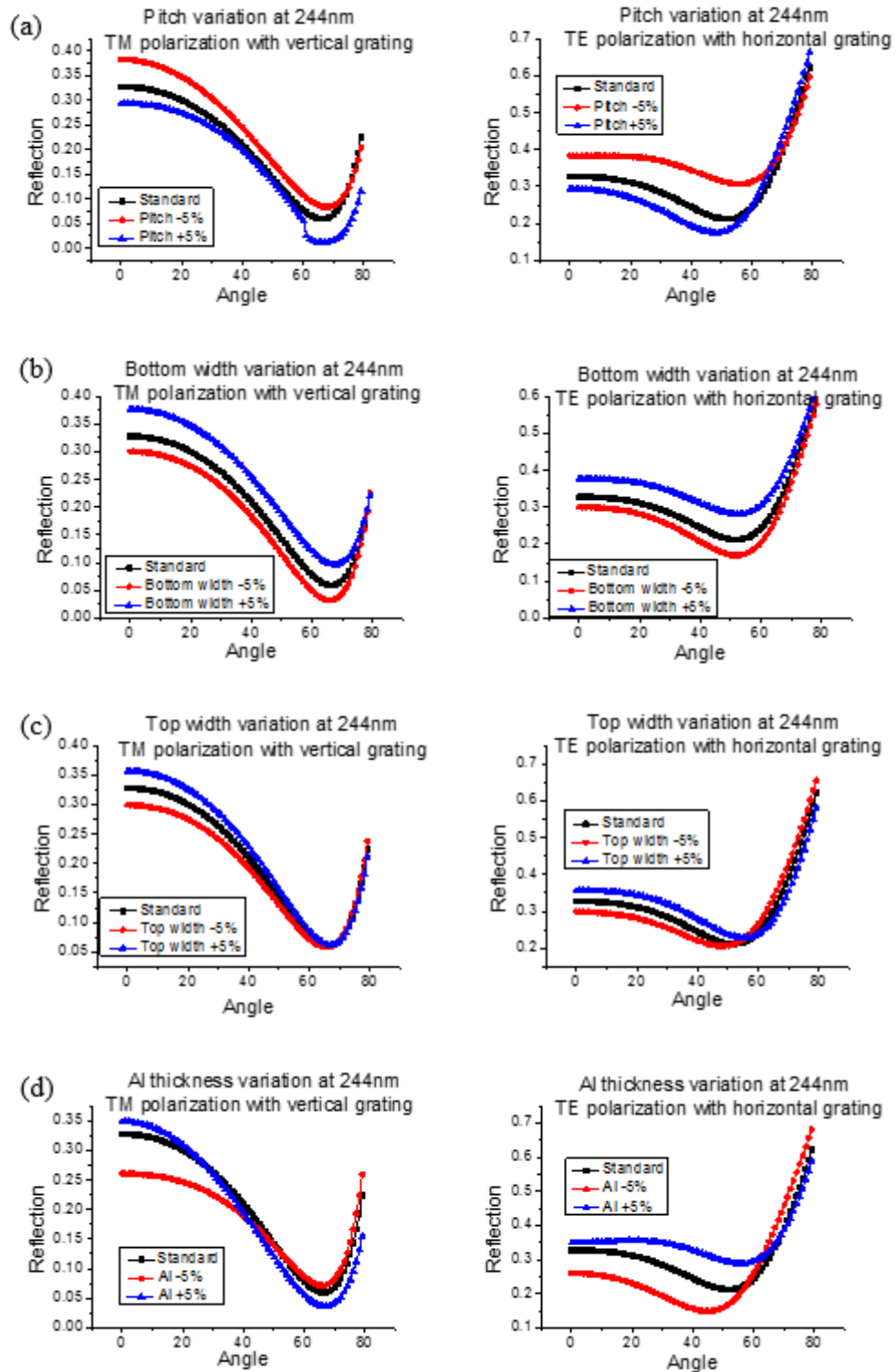


Figure 4.21 Major parameters variation at 244 nm (Standard, -5% and +5% conditions): (a) Pitch (b) Bottom width (c) Top width (d) Al thickness

4. Experiments and Results

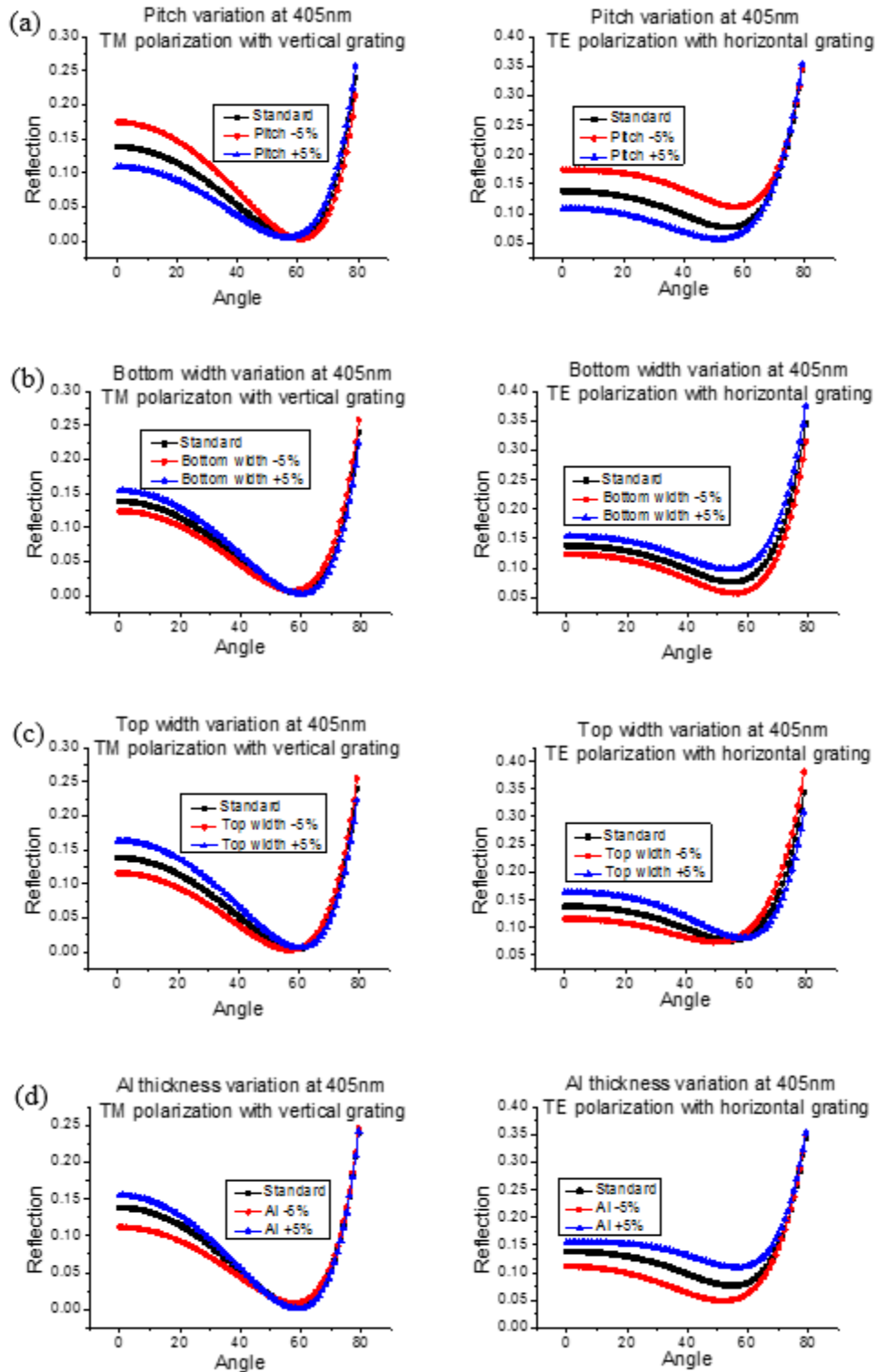


Figure 4.22 Major parameters variation at 405 nm (Standard, -5% and +5% conditions): (a) Pitch (b) Bottom width (c) Top width (d) Al thickness

4. Experiments and Results

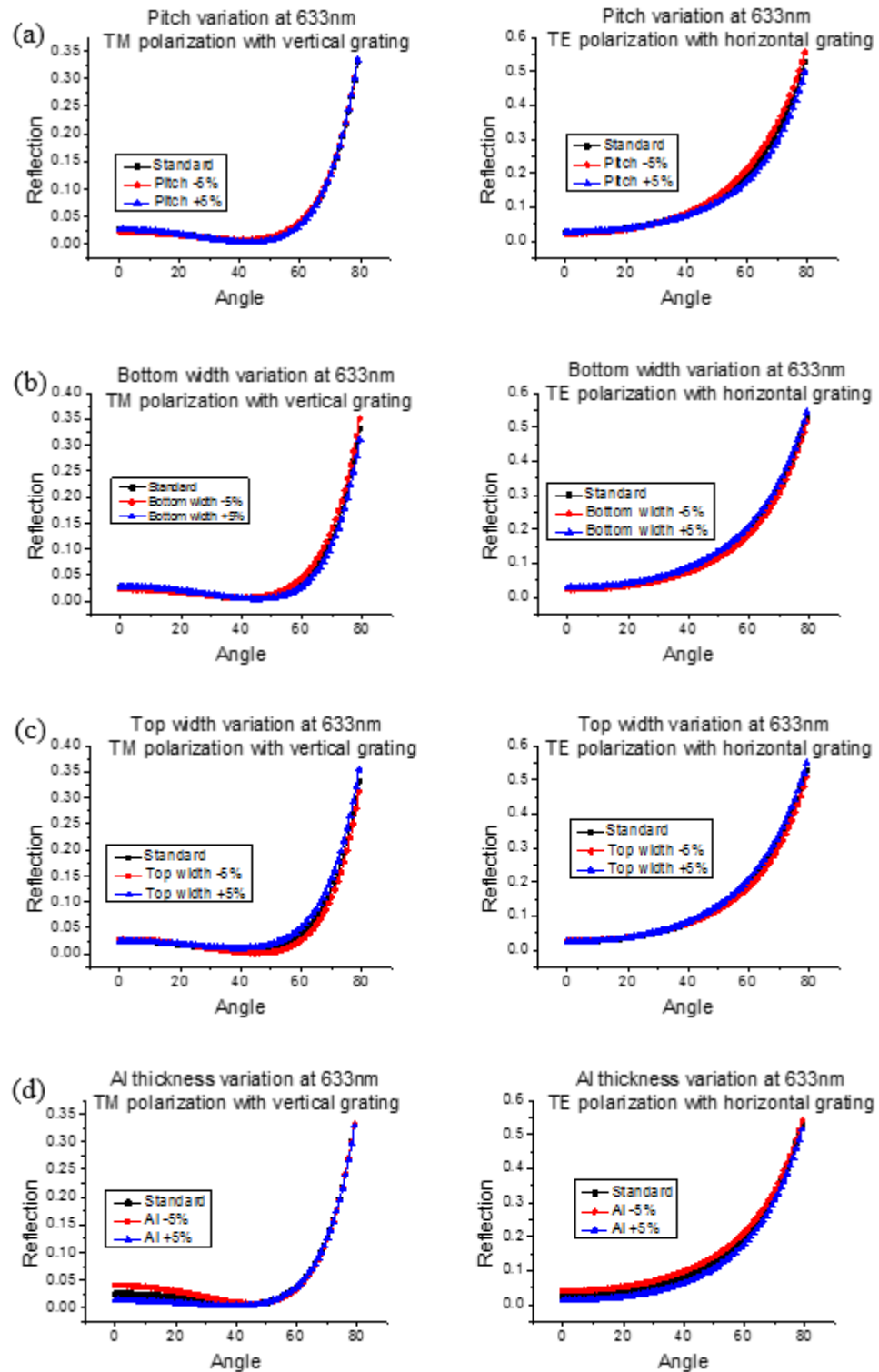


Figure 4.23 Major parameters variation at 633 nm (Standard, -5% and +5% conditions): (a) Pitch (b) Bottom width (c) Top width (d) Al thickness

4. Experiments and Results

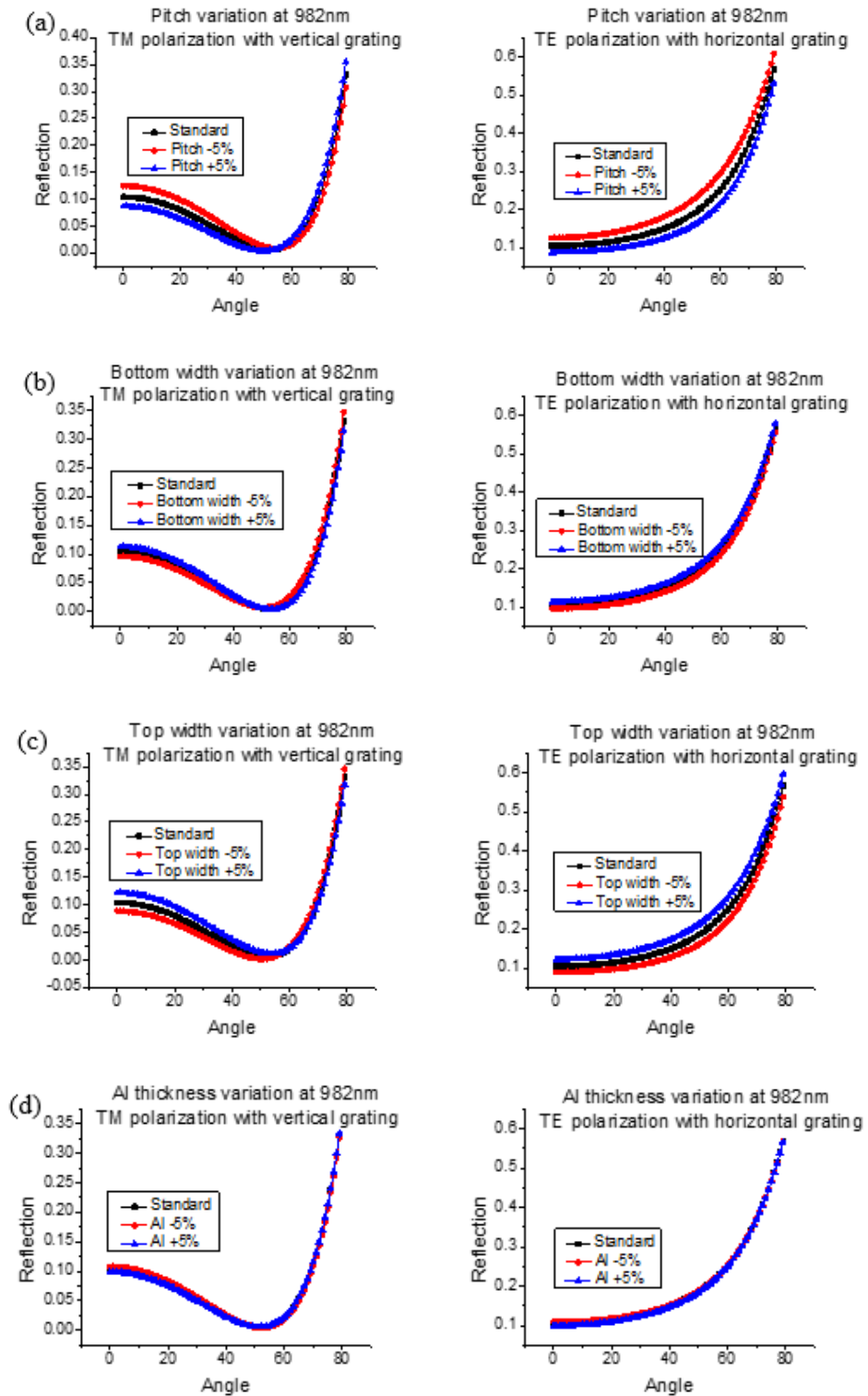


Figure 4.24 Major parameters variation at 982 nm (Standard, -5% and +5% conditions): (a) Pitch (b) Bottom width (c) Top width (d) Al thickness

4. Experiments and Results

The RMS difference between -5% condition and +5% condition is calculated for all four parameters at all four wavelength to provide a direct view of sensitivity of scatterometry.

Table 4.9 RMS between -5% and +5% conditions

$\Delta (10^{-2})$ <i>nm</i>	ΔP	ΔBW	ΔTW	ΔAI
244 nm	9.0	8.0	5.0	9.2
405 nm	5.2	3.2	3.8	4.1
633 nm	2.0	1.7	1.9	2.5
982 nm	4.9	1.7	3.8	0.6

As shown in Table 4.5, although scatterometry was less sensitive with larger wavelengths, as expected, the simulation results showed nonetheless that scatterometry at all four wavelengths had sufficient sensitivity and capability to detect the changing parameter. In pitch variation at 244 nm (Figure 4.22(a)), reflection has a shape reduce at

60° for pitch with +5% condition causing by surface resonance. It is a sufficient fingerprint for scatterometry measurement. With a laser wavelength that is ten times larger than the pitch (at 982 nm, $\lambda/p=9.80$), there was still structure information and reasonable sensitivity in the scatterometry measurements. For the other three parameters not shown (**FS**, **HR**, **VR**), they are not sensitive to parameter variations. However, in the previous section, we shows these minor parameters are still very important for our structure definition and have to be included in simulation.

4.2 Resist Grating

For the resist sample, when the grating directions were perpendicular to the polarization directions, strong Fabry-Perot effects were observed in the scatterometry measurements, which caused difficulties in the fitting. Thus, for the resist grating samples, the measurement was conducted for the condition in which the grating directions were parallel to the polarization directions (TM polarization with a horizontal grating, and TE polarization with a rotated, vertical grating; see Figure 4.26), opposite to the conditions in the WGP polarization.

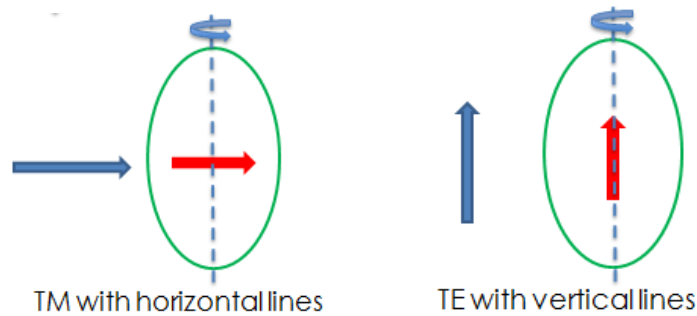


Figure 4.25 Parallel conditions between gratings and polarizations the red line is grating direction and the blue line is polarization direction

4.2.1 Resist Grating Made by J-FIL

4.2.1.1 Structure Definition

The resist grating sample was ~130 nm pitch and had a ~100 nm height resist grating on a polycarbonate substrate. We used five parameters to define the resist grating structure:

Pitch (P), Bottom Width (BW), Top Width (TW), Resist Height (H), and Residual layer Thickness (RT) (see Figure 4.27). The substrate for the resist grating samples was polycarbonate, which is a flexible material with high optical transmission.

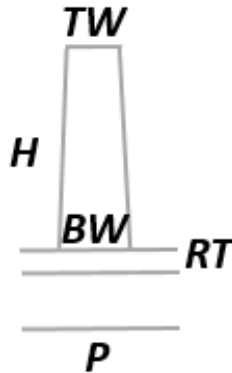


Figure 4.26 Definition of grating structure for J-FIL resist grating

4.2.1.2 Sensitivity of Resist Grating

The parameters used in the simulation were $P = 131.50$ nm, $BW = 86$ nm, $TW = 79$ nm, $H = 96.50$ nm, and $RT = 10$ nm. The step of parameter changing is $\pm 5\%$: $\Delta P = \pm 6.6$ nm, $\Delta BW = \pm 4.3$ nm, $\Delta TW = \pm 4.0$ nm and $\Delta H = \pm 4.8$ nm. We changed only one parameter at a time, as in the WPG procedure.

4. Experiments and Results

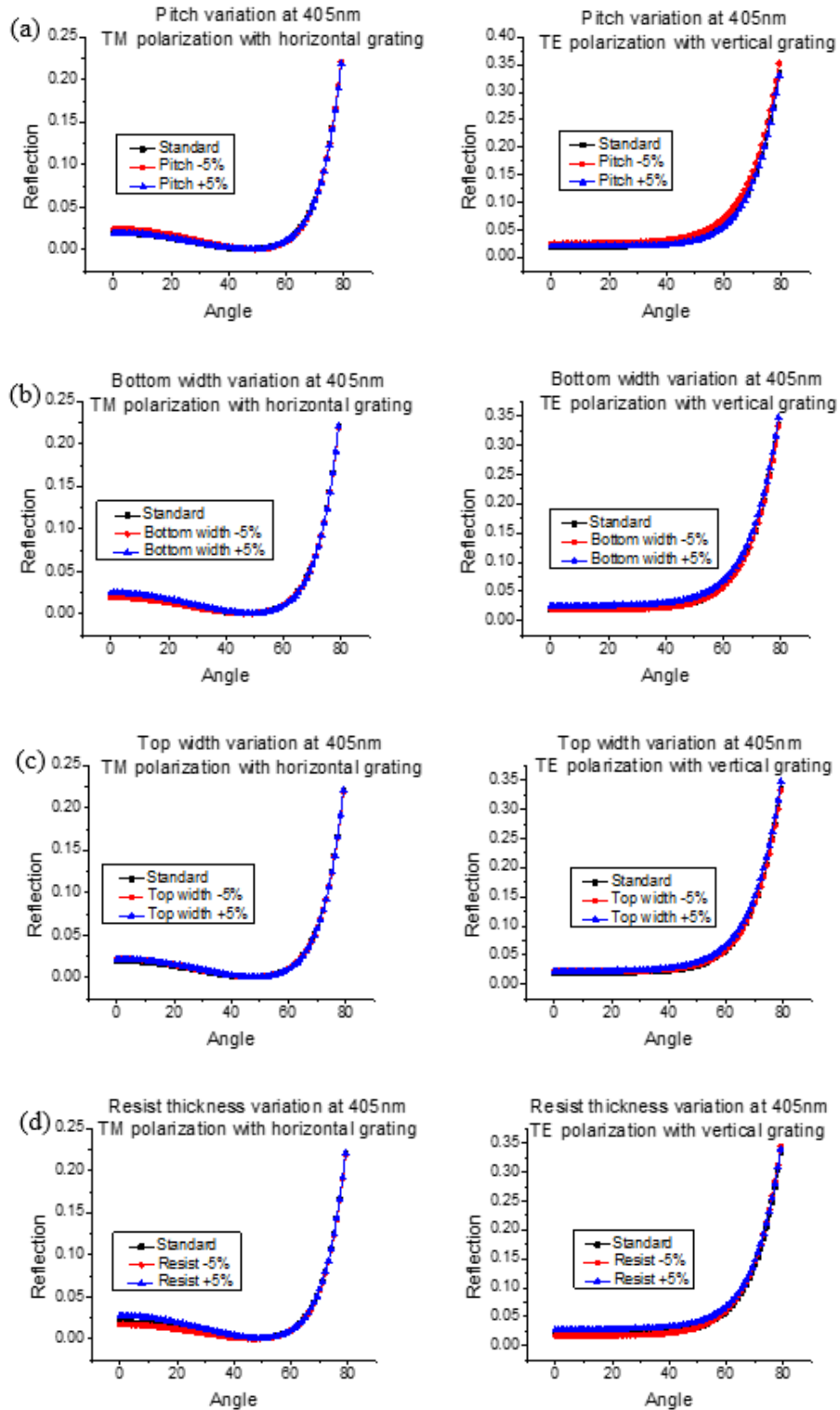


Figure 4.27 Major parameters variation at 405 nm (Standard, -5% and +5% conditions): (a) Pitch (b) Bottom width (c) Top width (d) Resist thickness

4. Experiments and Results

The RMS difference between -5% condition and +5% condition is calculated for all four parameters at 405nm.

Table 4.11 RMS between -5% and +5% conditions

$\Delta (10^{-2})$ <i>nm</i>	ΔP	ΔBW	ΔTW	ΔH
405 nm	0.88	0.67	0.46	0.77

These simulation results showed that the resist grating scatter signature had a lower sensitivity to changes in the nanostructure parameters than that of the WGP samples. The reason for this is that the difference in the refractive indices for the WGP was much larger than that of the resist grating. For the WGP, the permittivity of Al is ~ 23 and that of the substrate is ~ 2.6 . For the resist grating, the permittivity of the resist is ~ 2.6 , while that of the substrate is ~ 2.3 . In the simulations, the sensitivity of the reflection variation was related to the difference in the refractive index between the grating materials (Al:air and resist:air) and the substrate. High contrast situations (such as the WGP) will contain more information about the surface. The simulation still showed that the scatterometry measurements can provide enough information to determine the nanoscale parameters of the sample. However, the reduced sensitivity suggests that there is less headroom for extending to a larger λ/p .

4.2.1.3 Fitting Results

The same RMS procedure was used for the resist grating fitting process. Because the sensitivity of the resist grating measurement is lower than that of the WGP measurement, a larger simulation step was used. The minimum simulation step of P , R , and RL was 0.50 nm, and that of BW and TW was 1nm. The minimum variance was 3.91×10^{-3} . The scatterometry result is compared with AFM measurement of resist sample and a SEM image of master mask used in manufacturing procedure.

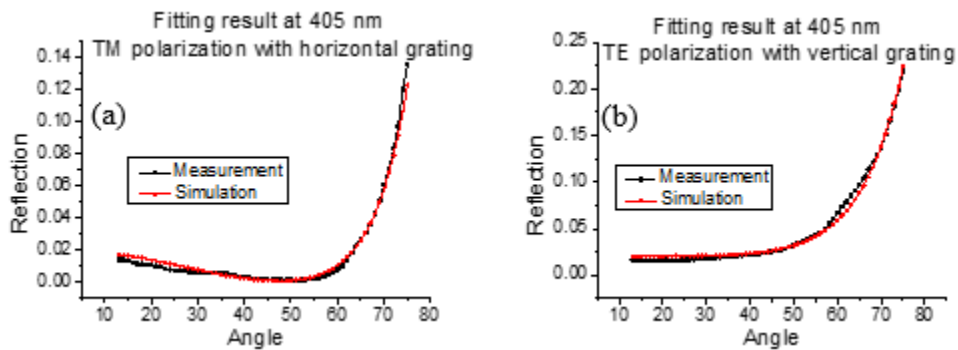


Figure 4.28 Fitting results of resist grating for 405 nm measurements: (a) TM polarization with horizontal grating, (b) TE polarization with vertical grating

Although the sensitivity of scatterometry for the resist grating is not as high as that for WGP, the scatterometry results agreed well with the AFM measurements of the pitch and the SEM measurements of the master grating. Compared to the other two measurement methods, only scatterometry has the ability to measure the TW and RL . The BW reading of AFM had a relatively large value because of the well-known artifact that arises from

4. Experiments and Results

the width of the AFM tips. Therefore, the correct AFM reading for **BW** needs to be calibrated further.

Table 4.13 Scatterometry fitting results of resist grating

$\lambda(\text{nm})$ \diagdown (nm)	Pitch	Bottom width	Top width	Resist Height	Residual Layer
Scatterometry	131.5	86.0	79.0	96.5	7.5
AFM	130.9	105.4-2 δ	NA	102	NA
Master Grating	130	65	NA	100 (silica)	NA

4.2.1.4 Macroscopic Defects

$\lambda(\text{nm})$ \diagdown (nm)	Pitch	Bottom width	Top width	Resist Height	Residual Layer
Scatterometry	131.5	86.0	79.0	96.5	7.5
AFM	130.9	105.4-2 δ	NA	102	NA
Master Grating	130	65	NA	100 (silica)	NA

Multiple scatterometry measurements were taken at different area on resist sample

surface. The reflectivity plots showed changes when the beam was directed to areas of the sample with different types and degrees of inhomogeneous defects. In contrast to the best conditioned area (that with the fewest defects), the reflected power in the areas with defects was not a smooth function, particularly at small measurement angles. There were also large differences in intensity over the full angular range (see Figure 4.30). Thus, scatterometry is a sensitive and efficient metrology method to detect and possibly classify macroscopic defects, which is a highly important metrology result in manufacturing control.

4. Experiments and Results

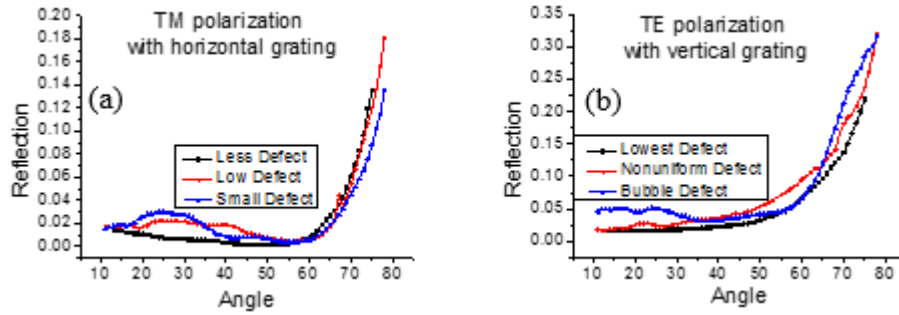


Figure 4.30 Scatterometry measurement at different area with different type of defects

We also monitored the shape of the reflected spot for these same defective areas. For the area with the fewest defects, the reflection pattern was round and had a roughly Gaussian intensity variation; this is the region used to fit the photoresist grating parameters. For

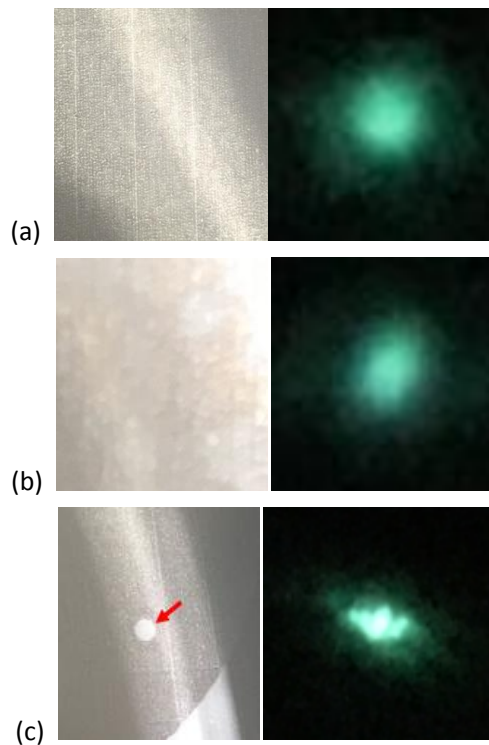


Figure 4.29 Different types of defects and reflection pattern. (a) Lowest defects (b) Nonuniform defects (c) Air-bubble defects

non-uniform areas and those with air bubbles, the reflection pattern became distorted and the intensity showed the internal structure. These reflection patterns could help in classifying the types of defects in samples.

4.2.2 Resist Grating Made by IIL

4.2.2.1 Structure Definition

The resist grating sample was ~ 85 nm pitch and had a ~70 nm height resist grating on a ~40 nm ARC layer and silicon substrate. We used five parameters to define the resist grating structure: Pitch (P), Bottom Width (BW), Top Width (TW), Resist Height (H), and ARC Thickness (ARC) (see Figure 4.32).

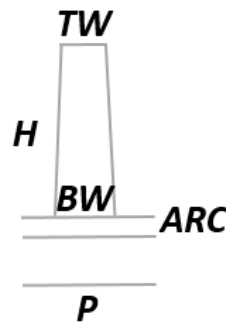


Figure 4.31 Definition of grating structure for IIL grating

4.2.2.2 Sensitivity Study

The parameters used in the simulation were $P = 86$ nm, $BW = 46$ nm, $TW = 42$ nm, $H = 70$ nm, and $ARC = 40$ nm. The parameter change step is $\pm 5\%$: $\Delta P = \pm 4.3$ nm, $\Delta BW = \pm 2.4$ nm, $\Delta TW = \pm 2$ nm and $\Delta H = \pm 3.5$ nm. We changed only one parameter at a time, following the same procedure as mentioned in previous section.

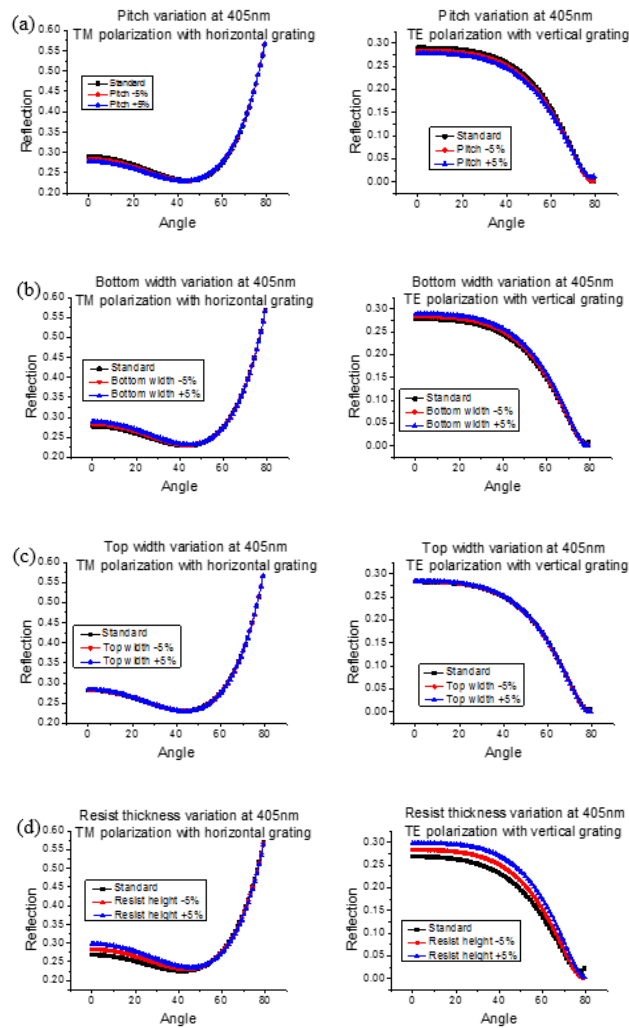


Figure 4.32 Major parameters variation at 405 nm for $P = 86$ nm, $BW = 46$ nm, $TW = 42$ nm, $H = 70$ nm, and $ARC = 40$ nm (Standard, -5% and +5% conditions):
 (a) Pitch (b) Bottom width (c) Top width (d) Resist thickness

4. Experiments and Results

A RMS difference between -5% condition and +5% condition is calculated for all four parameters at 405nm.

Table 4.15 RMS between -5% and +5% conditions

$\Delta (10^{-2})$ <i>nm</i>	ΔP	ΔBW	ΔTW	ΔAI
405 nm	0.93	0.90	0.13	2.7

Comparing with the RMS conditions with resist grating made by J-FIL (Table 4.6), resist

grating sample with smaller pitch ($P=86$ nm) made by IIL has a larger RMS variation than the resist grating sample made by J-FIL ($P=130$ nm). As discussed above, this is

$\Delta (10^{-2})$ <i>nm</i>	ΔP	ΔBW	ΔTW	ΔAI
405 nm	0.93	0.90	0.13	2.7

because resist grating made by IIL is on a silicon substrate which has a higher refractive index contrast with the resist. The permittivity of silicon at 405 nm is ~ 31.36 while the permittivity of the resist and ARC is ~ 2.56 . The large index contrast makes scatterometry more sensitive for parameter changes even with a smaller feature size sample.

4.2.2.3 Fitting Result

The same RMS procedure was used for the resist grating fitting process. We used the same step for resist grating made by J-FIL. The minimum simulation step of P , H , and ARC was 0.50 nm, and that of BW and TW was 1nm.

4. Experiments and Results

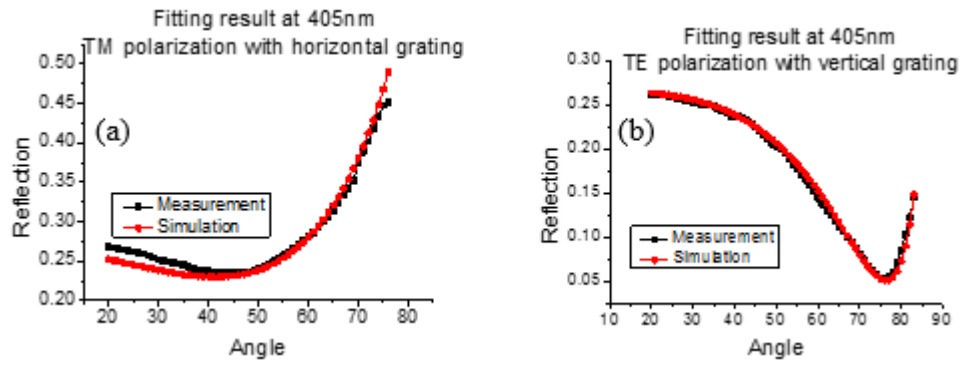


Figure 4.33 Fitting results of resist grating for 405 nm measurements: (a) TM polarization with horizontal grating, (b) TE polarization with vertical grating

The scatterometry result is compared with SEM measurement of resist grating made by IIL in Table 4.9.

Table 4.17 Scatterometry fitting results of resist grating

$\lambda(\text{nm})$ \diagdown (nm)	Pitch	Bottom width	Top width	Resist Height	ARC Layer
Scatterometry	84.8	36.0	31.2	70.4	43
SEM	87.5	35.0-48.0	25.0	65.7	NA

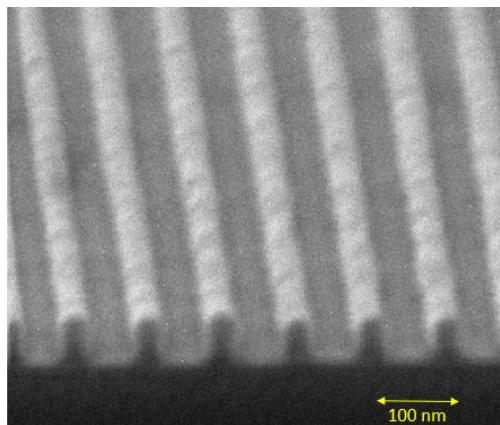


Figure 4.34 SEM of resist grating

Scatterometry provides a very similar reading to the SEM. The bottom width measurement has a blooming effect in SEM due to the finite electric beam width. For bottom width of SEM reading, the range from inside of the sidewall to the outside of the sidewall is indicated. There is some variation at top width between scatterometry and SEM. It is because the top width has a large variation from grating lines to grating lines and scatterometry measures an average conditions over a large area on sample. Another reason is that the SEM image is taken by tilted for 8° and it may have some error in the calibration process. For ARC layer thickness, our SEM does not obtain a sufficient resolution to measure it while scatterometry can still provide information about the ARC layer.

4.3 In-line Scatterometry Attempts

For the scatterometry setup introduced in section 3.2.1, the sample is rotated during measurement process which is not desirable for real-time, in-line application. For a real-time metrology tool, we should rotate beams and optics instead of rotating the sample itself to adjust incident angle.

In order to optimize scatterometry setup for real-time measurement, two parabolic mirrors and a cube glass wobbler are used to achieve the similar function of the two rotation stages. Figure 4.36 indicates the real-time measurement setup. The laser beam is

4. Experiments and Results

introduced to pass through the glass wobbler while the wobbler is periodic tilted mirror a certain angle range, then the beam after the wobbler is parallel moving in a certain distance. One parabolic mirror is placed in path to reflect the parallel moving beam to its focal plane with a beam spot size of 0.5 mm and the sample is place exactly at the focal plane of this parabolic mirror. When the beam is parallel moving back and forth, the incident angle on the sample surface is also changed simultaneously. The second parabolic mirror is placed at the symmetric position to collect the reflection from the sample and pass it into a camera. During measurement, the sample is fixed and the measurement time is less than 1 second. Comparing with the scatterometry setup introduced in Chapter 3.2.1, this in-line scatterometry setup can provide a much faster measurement and does not need to move the sample which makes it very industry-friendly and suitable for real-time measurement in manufacturing process.

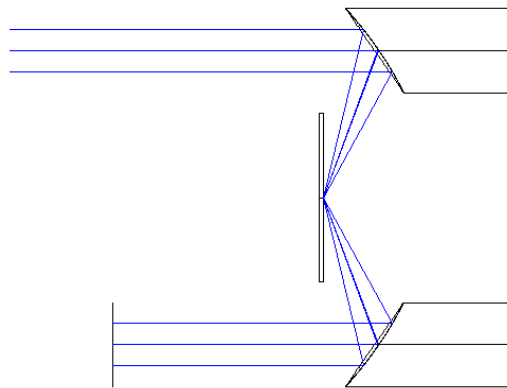


Figure 4.35 Real-time scatterometry design in Zemax

Different from the previous scatterometry setup, the measurement angle range of this on-line system is about 10° to 20° which is smaller than the measurements in the previous chapter. It is true that measurement for a larger angle range contains more structure information and makes it easier to find an initial parameter set for the automatic fitting process. As discussed in Chapter 3.3.1, we may need to optimize our initial parameter set in several positions to avoid local minimum and find the right ones for automatic fitting process. However, during manufacturing in industry, the parameters of structure are known and should only have a small variation. We could simply chose the standard or desired parameters of the product structure as the initial parameter sets. If the fitting process ends up at a local minimum with a large RMS, it indicates there is a large variation between the real structure and the desired one which means the product measured is with large defects. It is be not necessary to measure at full angle range and a smaller angle range measurement is sufficient for quality control proposed for manufacturing.

A test digital library is built for resist grating made by J-FIL. The initial parameter sets are $P = 131.50$ nm, $BW = 86$ nm, $TW = 79$ nm, $H = 96.50$ nm, and $RT = 10$ nm. The step of P , H and RT is 0.5 nm; step of BW and TW is 1 nm. The range of parameter variation is: $\Delta P = \pm 1$ nm, $\Delta BW = \pm 2$ nm, $\Delta TW = \pm 2$ nm, $\Delta H = \pm 2$ nm and $\Delta RL = \pm 2$ nm. To build up a library coving the designed range of the five parameters, the number of

4. Experiments and Results

different parameter sets is 10125 (5x5x5x9x9). Both TM polarization and TE polarization are calculated for each parameter set and the results are stored in the memory of a laptop. Several random measurement data sets are chosen as inputs and an automatic program runs to find the minimum RMS conditions for these random input. The average searching time is about 0.2 second with a 2.40GHz i7 CPU and 8GB RAM. Combining in-line setup and library searching, scatterometry can provide a fast in-line measurement in manufacturing process.

5 Limits of Scatterometry

From the results presented in the previous chapter, scatterometry can measure a 50 nm half pitch Al feature structures using a 982 nm laser beam for which the wavelength of the laser is twenty times larger than the half pitch. This suggests that a 405 nm laser source has the potential capability to measure 20 nm half pitch features. Today, the semiconductor industry is moving from the 14 nm node to 12 nm node with plans to go to the 7 nm node in 2018 with half pitch of ~18 nm. As scatterometry is a potential metrology technology for these generations of semiconductor manufacturing, it is necessary to study its fundamental limitations how impact its sensitivity and accuracy of these technique.

5.1 Noise Level

An essential part for scatterometry limitation study is to determine the noise level of the measurement system. When scatterometry reaches its limitation, it means there is insufficient structure information in the scatterometry signature of sample surface and noise is larger than the simulation variations as the fully parameters are changed. The variance for changing parameters is defined as the maximum difference among the data points between the initial parameter sets and a $\pm 5\%$ variation of the parameters. If the variation is larger than the system noise level, the parameter change is considered as “visible” in scatterometry measurement. For the special condition, if noise is infinitely

small, there is actually no limitation for this system. Meanwhile, simulation in RCWA has to be stable with the selected number of modes.

In order to obtain the noise level of our scatterometry system, we measured the same area at the same sample several times and then we calculate an average RMS difference for these measurement. The first time measurement data points are chosen to be the reference. The average RMS difference is calculated by Equation 5.1:

$$RMS(i) = \frac{\sum_m \sqrt{\sum_n (x_n - x_{i,n})^2 / N}}{M} \quad (5.1)$$

where x_n is the measurement data point at the n^{th} incident angle, $x_{i,n}$ is the first measurement data point at the same incident angle, N is the total number of data points and M is the total number of measurements. This RMS evaluation shows the reflection variation between several measurements at 8° to 80° angle range for the same sample area. This noise level means that we can only measure reflection levels to an uncertainty of 6.4×10^{-4} .

5.2 Limitation for WGP structure

For studying the limitation of scatterometry applied to the WGP, we shrink the structure size of sample in the simulation. A reflection difference is calculated between the scaled structure and its 5% variation of one of its parameters for TM polarization with vertical grating and TE polarization with horizontal grating (same definition as was presented for

the WGP at Chapter 4.1). The maximum difference among angle range from 0.1° to 79.1° is compared with the noise level of our system. We used two different approaches to shrink the structure size: one is fixing the pitch at 100 nm and shrinking the line width of the grating and Al thickness separately to study the influence under variation of these two parameters; another is to shrink the whole structure simultaneously (e.g. linewidth, pitch and grating thickness) keeping the line width equal to the half pitch and the Al thickness equal to the pitch. All the simulation work is done at 405 nm wavelength. These two conditions are discussed separately below.

5.2.1 Pitch at 100 nm

The initial structure we defined in simulation is that the line width is equal to the half pitch ($BW/P=0.5$) and Al thickness is equal to two times the pitch ($Al/P=2$). We fix the pitch of WGP at 100 nm and (1) shrink Al grating width from 70 nm to 10 nm (See Figure 5.1); (2) Shrink Al grating thickness from 200 nm to 10 nm (See Figure 5.3).

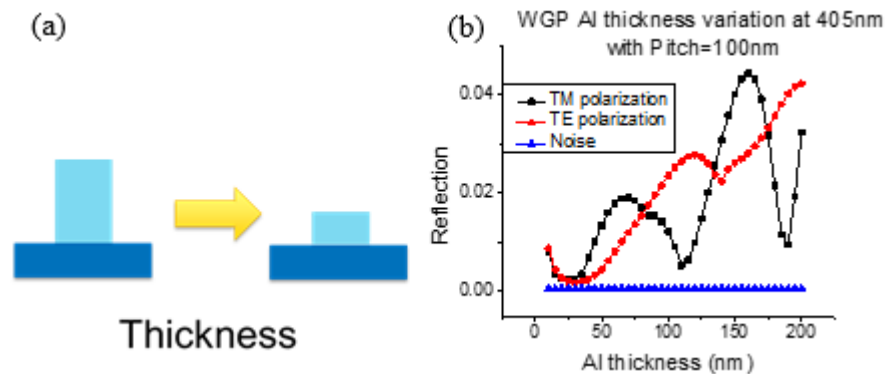


Figure 5.1 Varying Al thickness at fixed 100 nm pitch for WGP

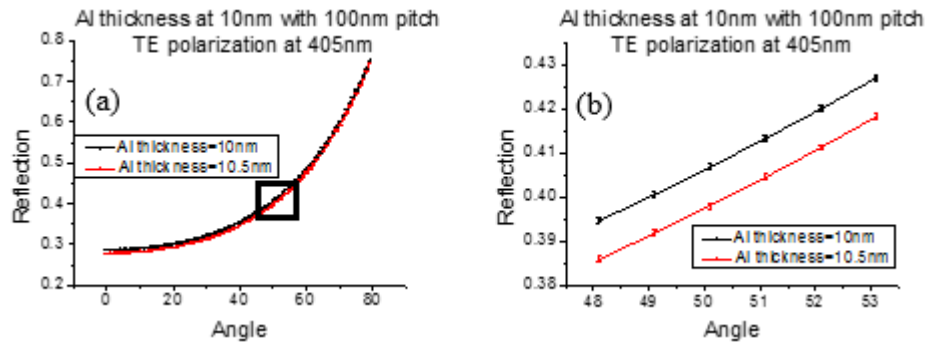


Figure 5.2 Al thickness at 10 nm with 100 nm pitch for WGP with error bar (a) large angle range (b) expanded area

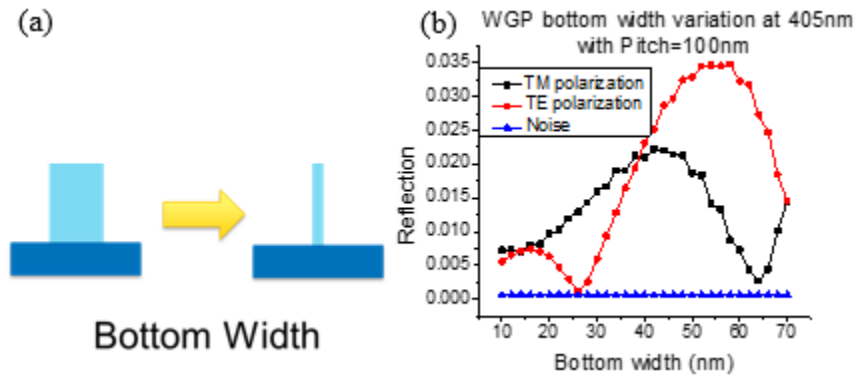


Figure 5.2 Varying line width at fixed 100 nm pitch for WGP

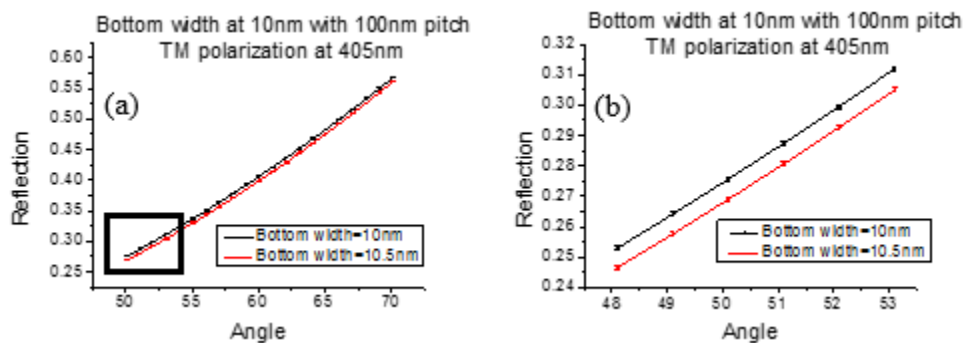


Figure 5.4 Bottom width at 10 nm with 100 nm pitch for WGP at TM polarization with error bar (a) large angle range (b) expanded area

Both simulation results indicate that scatterometry with 405 nm wavelength laser is sufficient to measure a grating size down to 10 nm on a 100 nm pitch structure (see Figure 5.2 and 5.4). When feature size approaches 10 nm scale, the difference between 5% parameter variations is still greater than our noise level, but becomes very small. In Figure 5.2, 5.4 and all other figures in the remaining of this chapter, an enlarged figure is used to show relation between the difference and error bar. It indicates that scatterometry system needs a very careful calibration and alignment to obtain any information at 10 nm scale because the two curves are parallel with each other and they only differ in reflected intensity. In linewidth variation condition, though TE polarization has lost sensitivity at ~25 nm line width (see Figure 5.3), it can be solved by switching to another wavelength laser.

5.2.2 Pitch Variation from 100 nm to 5 nm

In this section, the pitch size is varied from 100 nm to 5 nm. When the pitch varies, the line width of the grating changes simultaneously so that line width is fixed at half size of pitch and the Al thickness is fixed at 100 nm in the simulation.

Figure 5.5 shows result for the pitch of the WGP is varied from 100 nm to 10 nm.

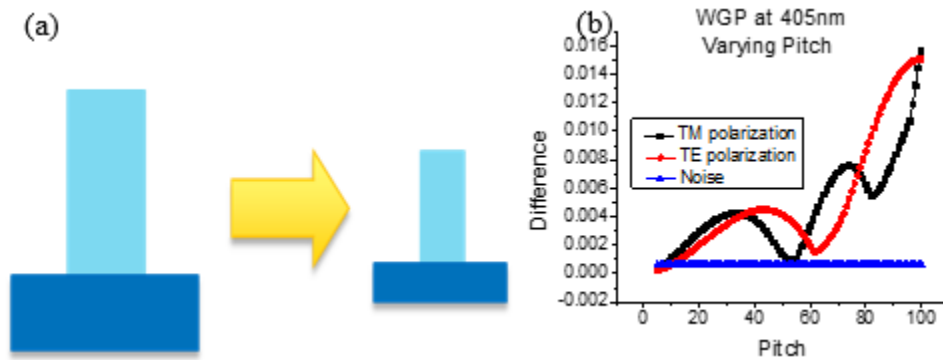


Figure 5.5 Varying Pitch from 100 nm to 10 nm for WGP

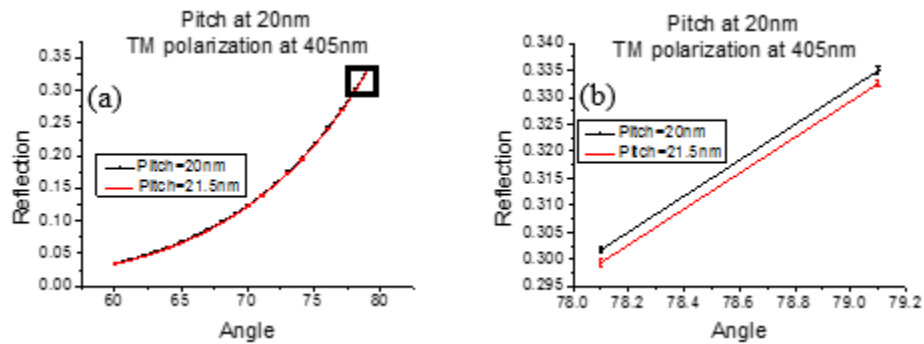


Figure 5.6 Pitch at 20 nm for WGP at TM polarization with error bar (a) full angle range (b) expanded area

The difference for TM and TE polarization conditions at pitch=100 nm is much greater than the noise level. It indicates that scatterometry measurement is very sensitive and sufficient for our current WGP sample with pitch=100 nm. Figure 5.6 demonstrates that scatterometry still obtain sensitivities at 20 nm feature size with 405 nm wavelength laser ($\lambda/p=20$) at TM polarization and the measurable feature size could be smaller with a lower noise system. This indicates the impressive potential capability of scatterometry.

Both polarizations have sharp changes at approximate $P=54$ nm in Figure 5.5. It may be caused by a surface resonance which is very common phenomenon happened at metal grating structure with wavelength \gg pitch⁶⁸. The reflection for TM polarization at normal incidence (0.1°) for different pitch is demonstrated in Figure 5.7.

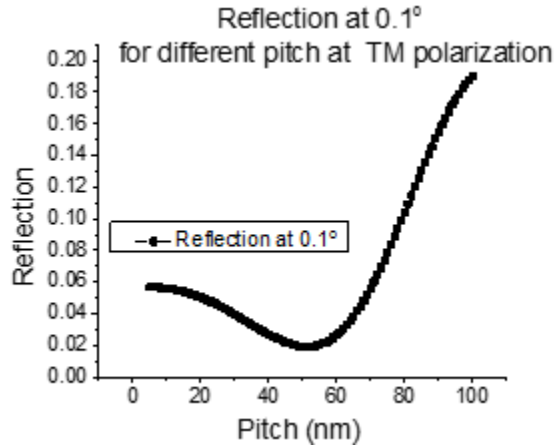


Figure 5.3 Reflection at normal incidence for different pitch at TM polarization

We notice the minimum reflection also appears at approximate $P=54$ nm which is related the result at Figure 5.5. At pitch range from 45 nm to 55 nm, the reflection is nearly disappeared which causes a loss of sensitivity. This problem could be easy to solve by switching to a similar but different wavelength laser to avoid the surface resonance.

5.3 Resist Grating

In this section, we look at simulations for the resist grating fabricated by J-FIL. As expected, the limits are not as good as those of WGP because of the low index contrast of this sample. Similar with limitation study of WGP, two different ways to shrink structure are discussed:

shrink line width and resist thickness at a fixed pitch=130 nm and shrink the pitch from 130 nm to 5 nm. With a scaled structure, simulations for this structure and a 5% variation on this structure are calculated for both TM polarization with horizontal grating and TE polarization with vertical grating (same conditions defined in Chapter 4.2.1).

5.3.1 Pitch at 130 nm

The initial structure we defined in the simulation is that the line width is equal to a half size of pitch (ratio of line / space is 1:1) and the resist thickness is 100 nm. We fix the pitch of resist grating at 130 nm and (1) shrink resist grating width from 100 nm to 10 nm (See Figure 5.8); (2) shrink resist grating thickness from 100 nm to 10 nm (See Figure 5.10).

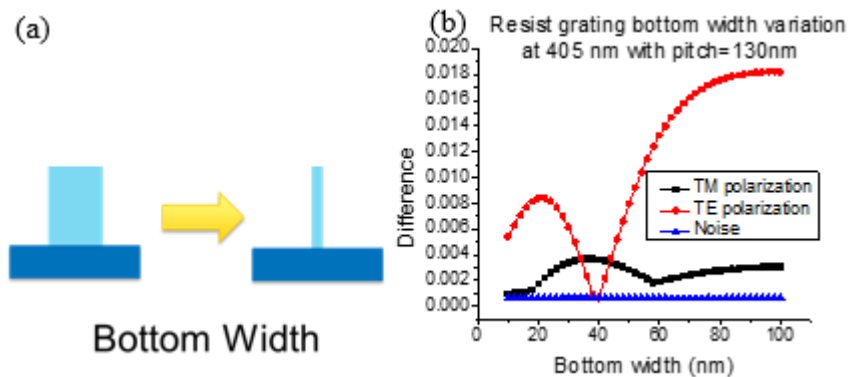


Figure 5.4 Varying line width at fixed 130 nm pitch for resist grating

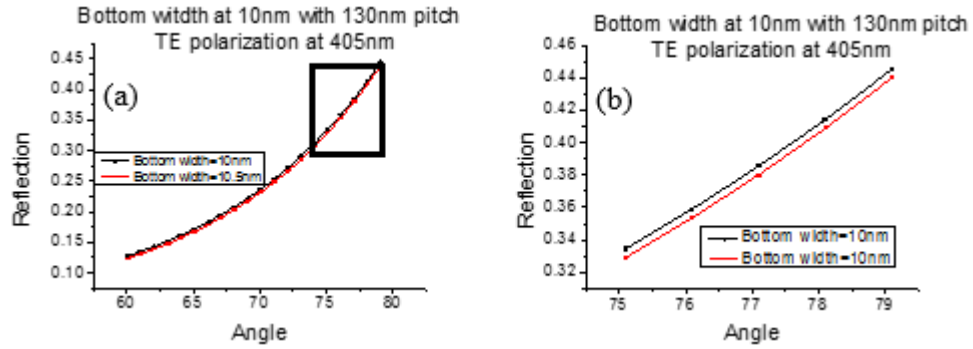


Figure 5.9 Bottom width at 10 nm with 130 nm pitch at TE polarization with error bar (a) large angle range (b) expanded area

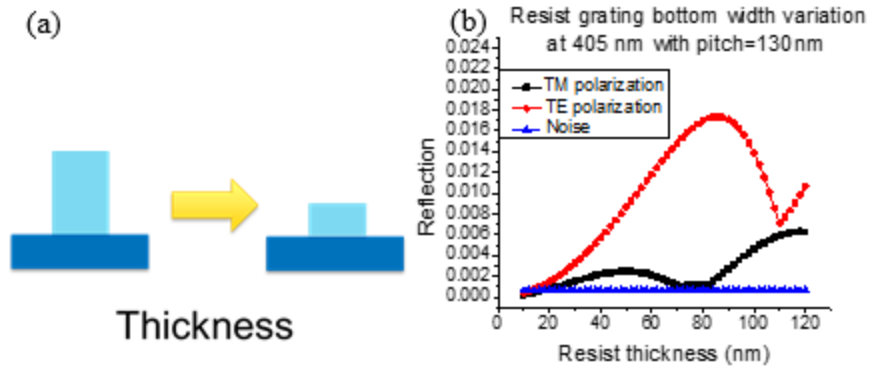


Figure 5.5 Varying resist thickness at fixed 130 nm pitch for resist grating

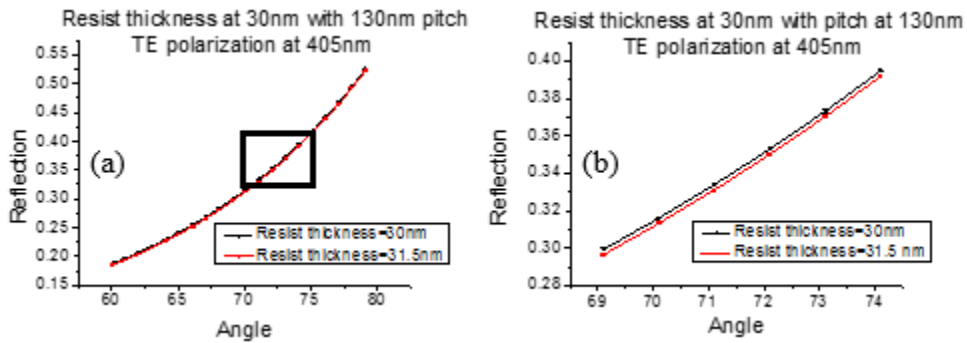


Figure 5.11 Resist thickness at 30 nm at 130 nm pitch with TE polarization with error bar (a) large angle range (b) expanded area

TE polarization has a better sensitivity for parameter variation for resist grating at pitch

= 130 nm. Comparing with WGP results in this chapter, scatterometry is less sensitivity for resist grating because less contrast of indices (discussed in Chapter 4.2.1.2), but simulations at Figure 5.9 and 5.11 indicates that scatterometry with 405 nm laser still can take a sufficient for line width at 10 nm and resist thickness at 30 nm.

5.3.2 Pitch Variation from 130 nm to 10 nm

In this section, pitch is varied from 130 nm to 10 nm and line width is fix at half of pitch and resist thickness is equal to pitch because for resist grating, there is a stronger surface tension between gratings with a smaller pitch and gratings are likely to collapse with a high ratio of resist grating thickness over pitch.

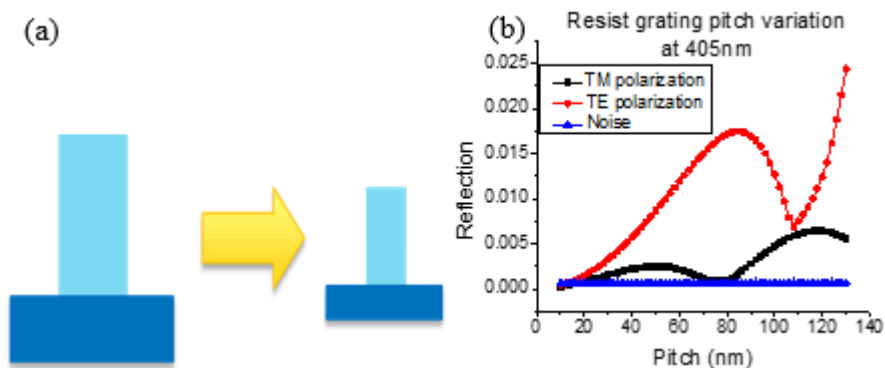


Figure 5.6 Varying resist thickness at fixed pitch for resist grating

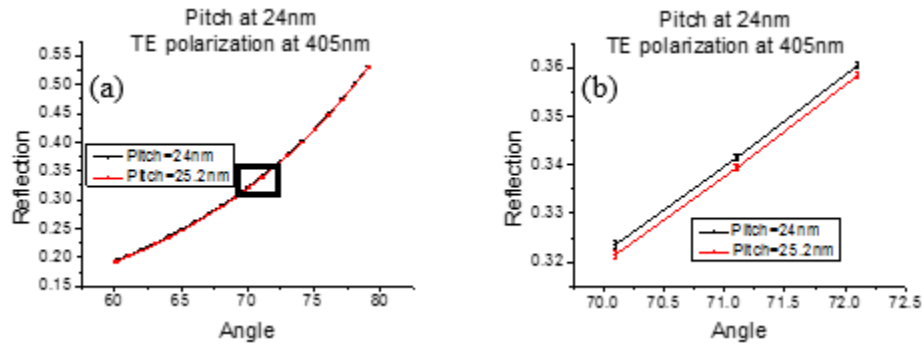


Figure 5.7 Pitch at 24 nm for resist grating at TE polarization (a) large angle range (b) expanded area

Similar with the results in last section, TE polarization has much more sensitivity than TM polarization. Scatterometry lose the sensitivity at ~ 24 nm for both TM and TE polarization. Although a pitch of 24 nm is the limit of resist grating under current noise level, the Reflection vs. Angle graphs are still different with an effective medium approach discussed in Chapter 4.2.1.3. However, when pitch of resist grating approaches 14 nm, the Reflection vs. Angle graphs have a similar shape and reflection intensity comparing with the effective medium results. Figure 5.14 demonstrates that all resist grating structure information is lost at a pitch of 14 nm and that there is any effective refractive index information in Reflection vs. Angle graph.

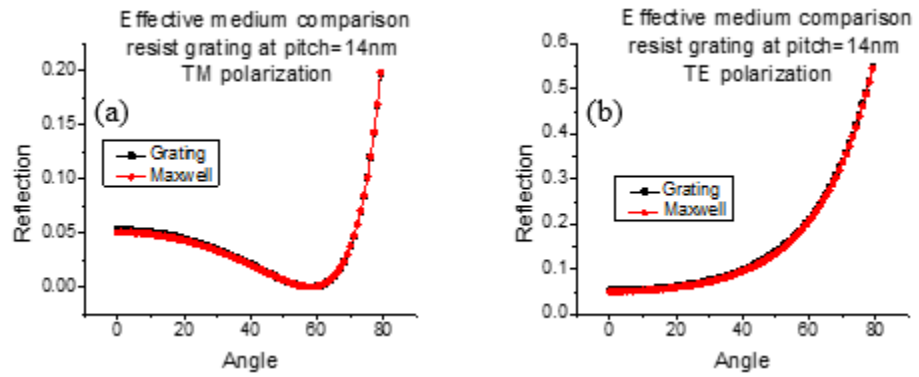


Figure 5.8 Comparison with grating structure simulation at pitch=14 nm and effective medium (a) TM polarization (b) TE polarization

6. Conclusion and Future Work

In this chapter, achievements of scatterometry project are summarized and relative future work is also proposed.

6.1 Conclusion

As shown in previous chapters, we designed and build up a bread-board scatterometry system. Both measurement and simulation indicate scatterometry is a sensitive, reliable, non-contact and non-destructive metrology technology for 50 nm half pitch features. Scatterometry is proven to be a promising metrology technology for next generation of semiconductor industry requirements for 10 nm node. Our work demonstrates the following points:

- This is the first angular scatterometry study using multiple wavelengths for the same sample. The different wavelengths (244 nm, 405 nm, 633 nm and 982 nm) of lasers in scatterometry are used to measure the same WGP sample. A sensitive study for wavelength / pitch (λ/p) based on the scatterometry is demonstrated that measurements at all these four wavelengths have significant difference with the effective medium approximations and contain sufficient information about surface structure in Reflection vs. Angle graphs. Scatterometry is proven to provide a sufficiently accurate measurement with $\lambda/p=10$ (100 nm pitch measured by 982 nm laser) for WGP. Multi-wavelength measurements also provide important independent information of the

structure definition helping to improve the model in RCWA to make fitting graphs and results more constant.

- Scatterometry measurement for three different types of samples: metal grating on fused silica, resist grating on polycarbonate and resist grating on silicon. The study demonstrates that 405 nm laser can provide a sufficient measurement for all of these three samples with 50 nm half pitch features. Measurement for resist grating samples is less sensitive than that for WGP because of low index contrast, but can still provide a reliable fitting result matched dimensions measured with AFM and SEM result.
- Scatterometry setup can also detect macroscopic defects on the sample surface using a camera. Different types of defects have different scatter shapes which are easy to be detected.
- Limitation study on WGP and resist grating structure indicates that scatterometry with 405 nm laser can provide sufficient measurement for ~20 nm Al features ($\lambda/p=20$) and ~24 nm resist features ($\lambda/p=17$) with the current system noise level. For resist grating on polycarbonate, at pitch of 14 nm, scatterometry does not obtain any grating structure information and Reflection vs. Angle graph is the same as the effective medium result.
- Our design of in-line real-time scatterometry system combining with library searching can be easily applied to industry manufacturing tools to provide reliable qualify control. Total measurement time could be within 1s and fitting process is as short as 0.2 s for

over 10000 parameter variations.

6.2 Future Work

Measurement part:

Because the longest wavelength (982 nm) laser in this dissertation can still provide a sufficient scatterometry measurement on WGP, we could introduce an even longer wavelength in scatterometry measurement to extend the ratio of λ/p .

In limitation study, we understand the sensitivity of scatterometry measurement is highly related with system noise level. For our scatterometry setup, most of noise is related to sample inhomogeneous and sample alignment. It could be improved to replace the sample stage with an automatic 3D mechanical stage and develop a sample alignment system to assure samples can always be placed at exactly the same position.

Simulation part:

The simulation results are not totally matched with measurement of WGP at 244 nm and 633 nm. Fitting results at four wavelengths are similar but not exactly the same. This indicates that some parameters defining the structure are missed in simulation. We fixed Al_2O_3 thickness at 4 nm in simulation. The influence of different Al_2O_3 thickness need some further study in the future. Some more parameters like width variation in fused

silica undercut also need to be investigated in simulation to find a better structure definition.

For current simulation model, the roughness of grating is not considered. When feature size become smaller and smaller, surface roughness could become a major error in measurement and simulation. CST software can provide a good model for roughness study, but as mentioned above, the simulation time of CST limits its capability to apply to scatterometry fitting process. A simulation of roughness on top of grating can be done in CST to demonstrate the roughness influence in Reflection vs. Angle graph. Then we could assume the roughness layer to be a plane effective medium and then transfer this roughness effective medium to RCWA to have an approximate roughness effect in simulation.

We should also extend scatterometry simulation to some complicate 2D/3D structures like FinFETs and dot array structure.

In-line scatterometry system part:

The in-line scatterometry system can adapt with macroscopic defects detections to provide an essential brief measurement with a high resolution camera. The angle range of in-line setup could be extended to provide more information about sample structure by

6. Conclusion and Future Work

using different optics to switch the beam and vary the incident angle. A noise level of in-line scatterometry system also need to be determined and improved.

Library searching speed could be faster by improving its algorithm. Several random positions in the parameter map could be calculate first to determine the area of best fitting result in the parameter map. It could speed up the searching process by avoiding unnecessary calculations at wrong parameter areas.

Reference

- 1 Diebold, Alain C., ed. *Handbook of silicon semiconductor metrology*. CRC Press, 2001.
- 2 National technology roadmap for semiconductors 2015
- 3 Hisamoto, Digh, et al. "FinFET-a self-aligned double-gate MOSFET scalable to 20 nm." *IEEE Transactions on Electron Devices* 47.12 (2000): 2320-2325.
- 4 Vandervorst, Wilfried, et al. "Conformal doping of FINFETs: a fabrication and metrology challenge." *ION IMPLANTATION TECHNOLOGY: 17th International Conference on Ion Implantation Technology*. Vol. 1066. No. 1. AIP Publishing, 2008.
- 5 Liu, Chi-Chun, et al. "Integration of block copolymer directed assembly with 193 immersion lithography." *Journal of Vacuum Science & Technology B* 28.6 (2010): C6B30-C6B34.
- 6 Park, Jong-Hee, and T. S. Sudarshan, eds. *Chemical vapor deposition*. Vol. 2. ASM international, 2001.
- 7 Cho, A. Y., and J. R. Arthur. "Molecular beam epitaxy." *Progress in solid state chemistry* 10 (1975): 157-191.
- 8 Ritala, Mikko, and Markku Leskela. "Atomic layer deposition." *Handbook of thin film materials* 1 (2001): 103-159.
- 9 Boning, Duane S., and James E. Chung. "Statistical metrology: Understanding spatial variation in semiconductor manufacturing." *Microelectronic Manufacturing 1996*. International Society for Optics and Photonics, 1996.
- 10 Rice, Bryan J., et al. "CD metrology for the 45-nm and 32-nm nodes." *Microlithography 2004*. International Society for Optics and Photonics, 2004.
- 11 Jalili, Nader, and Karthik Laxminarayana. "A review of atomic force microscopy imaging systems: application to molecular metrology and biological sciences." *Mechatronics* 14.8 (2004): 907-945.
- 12 Meli, F., and R. Thalmann. "Long-range AFM profiler used for accurate pitch measurements." *Measurement Science and Technology* 9.7 (1998): 1087.
- 13 Dai, Gaoliang, Fan Zhu, and Jens Fluegge. "High-speed metrological large range AFM." *Measurement Science and Technology* 26.9 (2015): 095402.

- 14 Dixon, Ronald, Ryan S. Goldband, and Ndubuisi G. Orji. "Lateral tip control effects in CD-AFM metrology: the large tip limit." *SPIE Scanning Microscopies*. International Society for Optics and Photonics, 2015.
- 15 Orji, Ndubuisi G., et al. "Tip characterization method using multi-feature characterizer for CD-AFM." *Ultramicroscopy* 162 (2016): 25-34.
- 16 Wong, Stanislaus S., et al. "Functionalization of carbon nanotube AFM probes using tip-activated gases." *Chemical Physics Letters* 306.5 (1999): 219-225.
- 17 Wong, Stanislaus S., et al. "Carbon nanotube tips: high-resolution probes for imaging biological systems." *Journal of the American Chemical Society* 120.3 (1998): 603-604.
- 18 Yu, Fangzhou, et al. "Design, fabrication, and characterization of polymer-based cantilever probes for atomic force microscopes." *Journal of Vacuum Science & Technology B* 34.6 (2016): 06KI01.
- 19 https://simple.wikipedia.org/wiki/Atomic_force_microscope
- 20 Fallica, Roberto, Elizabeth Buitrago, and Yasin Ekinici. "Comparative study of line roughness metrics of chemically amplified and inorganic resists for extreme ultraviolet." *Journal of Micro/Nanolithography, MEMS, and MOEMS* 15.3 (2016): 034003-034003.
- 21 Verduin, T., et al. "Sensitivity of secondary electron yields and SEM images to scattering parameters in MC simulations." *Microelectronic Engineering* 155 (2016): 114-117.
- 22 Chin, A. K., H. Temkin, and R. J. Roedel. "Transmission cathodoluminescence: A new SEM technique to study defects in bulk semiconductor samples." *Applied Physics Letters* 34.7 (1979): 476-478.
- 23 Goldstein, Joseph, et al. *Scanning electron microscopy and X-ray microanalysis: a text for biologists, materials scientists, and geologists*. Springer Science & Business Media, 2012.
- 24 Constantoudis, Vassilios, et al. "Model-aided hybrid metrology for surface roughness measurement fusing AFM and SEM data." *17th International Congress of Metrology*. EDP Sciences, 2015.
- 25 Lorusso, Gian Francesco, et al. "Line width roughness accuracy analysis during pattern transfer in self-aligned quadruple patterning process." *SPIE Advanced Lithography*. International Society for Optics and Photonics, 2016.
- 26 <https://www.purdue.edu/ehps/rem/rs/sem.htm>

- 27 Raymond, Christopher J., et al. "Multiparameter grating metrology using optical scatterometry." *Journal of Vacuum Science & Technology B* 15.2 (1997): 361-368.
- 28 Madsen, Morten Hannibal, and Poul-Erik Hansen. "Scatterometry—fast and robust measurements of nano-textured surfaces." *Surface Topography: Metrology and Properties* 4.2 (2016): 023003.
- 29 Raymond, Christopher J., et al. "Multiparameter grating metrology using optical scatterometry." *Journal of Vacuum Science & Technology B* 15.2 (1997): 361-368.
- 30 Fursenko, O., et al. "Through silicon via profile metrology of Bosch etching process based on spectroscopic reflectometry." *Microelectronic Engineering* 139 (2015): 70-75.
- 31 Raymond, Christopher J., et al. "Metrology of subwavelength photoresist gratings using optical scatterometry." *Journal of Vacuum Science & Technology B* 13.4 (1995): 1484-1495.
- 32 Madsen, Morten Hannibal, and Poul-Erik Hansen. "Imaging scatterometry for flexible measurements of patterned areas." *Optics express* 24.2 (2016): 1109-1117.
- 33 Kritsun, Oleg, et al. "Extending scatterometry to the measurements of sub 40 nm features, double patterning structures, and 3D OPC patterns." *SPIE Advanced Lithography*. International Society for Optics and Photonics, 2008.
- 34 Zhu, Ruichao, et al. "Metrology of 50nm HP wire-grid polarizer: a SEM-scatterometry comparison." *SPIE Advanced Lithography*. International Society for Optics and Photonics, 2015.
- 35 M. Golam Faruk, Matthew S. Angyal, Oluwafemi Ogunsola, David K. Watts and R. Wilkins, "Variability Modeling and Process Optimization for the 32 nm BEOL Using In-Line Scatterometry Data", *Semiconductor Manufacturing IEEE Transactions on*, vol. 27, pp. 260-268, 2014, ISSN 0894-6507.
- 36 McNeil, John R. "Scatterometry applied to microelectronics processing." *Electronic-Enhanced Optics, Optical Sensing in Semiconductor Manufacturing, Electro-Optics in Space, Broadband Optical Networks, 2000. Digest of the LEOS Summer Topical Meetings*. IEEE, 2000.
- 37 Silver, Richard, et al. "Fundamental limits of optical critical dimension metrology: a simulation study." *Advanced Lithography*. International Society for Optics and Photonics, 2007.
- 38 Rice, Bryan J., et al. "The limits of CD metrology." *Microelectronic engineering* 83.4 (2006): 1023-1029.

- 39 Benschop, Jos, et al. "Integrated scatterometry for tight overlay and CD control to enable 20-nm node wafer manufacturing." *SPIE Advanced Lithography*. International Society for Optics and Photonics, 2013.
- 40 Diebold, Alain C., ed. *Handbook of silicon semiconductor metrology*. CRC Press, 2001.
- 41 McNeil, John R., Scott R. Wilson, and Richard H. Krukar. "Method for broad wavelength scatterometry." U.S. Patent No. 5,867,276. 2 Feb. 1999.
- 42 Kumar, Nitish, et al. "Reconstruction of sub-wavelength features and nano-positioning of gratings using coherent Fourier scatterometry." *Optics express* 22.20 (2014): 24678-24688.
- 43 Chou, Stephen Y., Peter R. Krauss, and Preston J. Renstrom. "Nanoimprint lithography." *Journal of Vacuum Science & Technology B* 14.6 (1996): 4129-4133.
- 44 Kooy, Nazrin, et al. "A review of roll-to-roll nanoimprint lithography." *Nanoscale research letters* 9.1 (2014): 1.
- 45 Schiff, Helmut. "Nanoimprint lithography: an old story in modern times? A review." *Journal of Vacuum Science & Technology B* 26.2 (2008): 458-480.
- 46 Guo, L. Jay. "Nanoimprint lithography: methods and material requirements." *Advanced Materials* 19.4 (2007): 495-513.
- 47 Sreenivasan, S. V. "Nanoscale manufacturing enabled by imprint lithography." *MRS bulletin* 33.09 (2008): 854-863..
- 48 Colburn, Matthew, et al. "Step and flash imprint lithography: a new approach to high-resolution patterning." *Microlithography'99*. International Society for Optics and Photonics, 1999.
- 49 Taniguchi, Jun, et al. "Measurement of adhesive force between mold and photocurable resin in imprint technology." *Japanese journal of applied physics* 41.6S (2002): 4194.
- 50 Chou, Stephen Y., Peter R. Krauss, and Preston J. Renstrom. "Nanoimprint lithography." *Journal of Vacuum Science & Technology B* 14.6 (1996): 4129-4133.
- 51 Bailey, T., et al. "Step and flash imprint lithography: Template surface treatment and defect analysis." *Journal of Vacuum Science & Technology B* 18.6 (2000): 3572-3577.

- 52 Choi, Byung Jin, Sidlgata V. Sreenivasan, and Stephen C. Johnson. "High precision orientation alignment and gap control stages for imprint lithography processes." U.S. Patent No. 6,873,087. 29 Mar. 2005.
- 53 X. Chen, S. Liu, C. Zhang, H. Jiang, Z. Ma, T. Sun and Z. Xu, "Accurate characterization of nanoimprinted resist patterns using Mueller matrix ellipsometry," *Opt. Express* **22**(12), 15165 (2014).
- 54 M. Asano, H. Tsuda, M. Komori, K. Matsuki, H. Abe, and W-Y Jung, "Scatterometry-based process control for nanoimprint lithography, *Proc SPIE* **9778**, 977820 (2016).
- 55 X. Chen, S. Liu, C. Zhang, H. Jiang, Z. Ma, T. Sun and Z. Xu, "Accurate characterization of nanoimprinted resist patterns using Mueller matrix ellipsometry," *Opt. Express* **22**(12) 15165 (2014).
- 56 K. Kogyo-Danchi, K. Sentoku, K. Sato and H. Ina, "A first-order analysis of scatterometry sensitivity for NIL process," *Proc. SPIE* **7637**, 763721 (2010).
- 57 H. J. Patrick, T. A. Germer, Y. Ding, H. W. Ro, L. J. Richter and C. L. Soles, "In situ measurement of annealing-induced line shape evolution in nanoimprinted polymers using scatterometry," *Proc. SPIE* **7271**, 727128 (2009).
- 58 R. M. Al-Assaad, L. Tao and W. Hu, "Physical characterization of nanoimprinted polymer structures using visible light angular scatterometry," *J. Micro/Nanolith, MEMS MOEMS* **7**(1), 013008 (2008).
- 59 H. J. Patrick, T. A. Germer, Y. Ding, H. W. Ro, L. J. Richter and C. L. Soles, "Scatterometry for in situ measurement of pattern reflow in nanoimprinted polymers," *Appl. Phys. Lett.* **93**, 233105 (2008).
- 60 R. M. Al-Assaad, S. Regonda, L. Tao, S.W. Pang, W. Hu, "Characterizing nanoimprint profile shape and polymer flow behavior using visible light scatterometry," *J. Vac. Sci. Technol.* **B25**(6), 2396 (2007)
- 61 D. Fuard, C. Perret, V. Farys, C. Gourgon and P. Sciavone, "Measurement of residual thickness using scatterometry," *J. Vac. Sci. Technol.* **B23**(6) 3069 (2005).
- 62 C. Courgon, N. Chaix, H. Shift, M. Tormen, S. Landis, C.M. Sotomayor-Torres, A. Kristensin, R.H. Pedersen, M. B. Christiansen, I. Fernandez-Cuesta, D. Mendels, L. Nontelius and T. Haatainen, "Benchmarking of 50 nm features in thermal nanoimprint," *J. Vac. Sci. Technol.* **B25**(6), 2373 (2007).
- 63 Ahn, Se Hyun, et al. "High-performance wire-grid polarizers using jet and Flash™ imprint lithography." *Journal of Micro/Nanolithography, MEMS, and MOEMS* **12.3** (2013): 031104-031104.

- 64 Moharam, M. G., and T. K. Gaylord. "Rigorous coupled-wave analysis of planar-grating diffraction." *JOSA* 71.7 (1981): 811-818.
- 65 Minhas, Babar Kaleem. *Numerical modeling of periodic structures: Metallic grids and metamaterials*. 2003..
- 66 Chen, Xiuguo, et al. "Improved measurement accuracy in optical scatterometry using fitting error interpolation based library search." *Measurement* 46.8 (2013): 2638-2646.
- 67 McCafferty, E., and J. P. Wightman. "Determination of the surface isoelectric point of oxide films on metals by contact angle titration." *Journal of colloid and interface science* 194.2 (1997): 344-355.
- 68 Ebbesen, Thomas W., et al. "Extraordinary optical transmission through sub-wavelength hole arrays." *Nature* 391.6668 (1998): 667-669.